

---

ETD Archive

---

Winter 1-1-2019

## Simulation And Control At the Boundaries Between Humans And Assistive Robots

Holly E. Warner  
*Cleveland State University*

Follow this and additional works at: <https://engagedscholarship.csuohio.edu/etdarchive>  
**How does access to this work benefit you? Let us know!**

---

### Recommended Citation

Warner, Holly E., "Simulation And Control At the Boundaries Between Humans And Assistive Robots" (2019). *ETD Archive*. 1304.  
<https://engagedscholarship.csuohio.edu/etdarchive/1304>

This Dissertation is brought to you for free and open access by EngagedScholarship@CSU. It has been accepted for inclusion in ETD Archive by an authorized administrator of EngagedScholarship@CSU. For more information, please contact [library.es@csuohio.edu](mailto:library.es@csuohio.edu).

SIMULATION AND CONTROL AT THE BOUNDARIES  
BETWEEN HUMANS AND ASSISTIVE ROBOTS

HOLLY E. WARNER

Master of Science in Mechanical Engineering

Cleveland State University

August 2015

Bachelor of Mechanical Engineering

Cleveland State University

May 2014

submitted in partial fulfillment of requirements for the degree

DOCTOR OF PHILOSOPHY IN ENGINEERING

at the

CLEVELAND STATE UNIVERSITY

DECEMBER 2019

We hereby approve this dissertation for  
HOLLY E. WARNER  
Candidate for the Doctor of Philosophy in Engineering degree  
for the Department of Mechanical Engineering and  
CLEVELAND STATE UNIVERSITY'S  
College of Graduate Studies by

---

Hanz Richter, Ph.D., Committee Chair  
Department of Mechanical Engineering

---

Antonie J. van den Bogert, Ph.D.  
Department of Mechanical Engineering

---

Eric Schearer, Ph.D.  
Department of Mechanical Engineering

---

Silai Shao, Ph.D.  
Department of Mathematics and Statistics

---

Dan Simon, Ph.D.  
Department of Electrical Engineering and Computer Science

Student's Date of Defense: December 3, 2019

This student has fulfilled all requirements for the  
Doctor of Philosophy in Engineering degree.

---

Chandra Kothapalli, Ph.D., Doctoral Program Director

## ACKNOWLEDGMENT

I want to thank the many individuals without whom this journey would have been impossible. First, to my advisor, Dr. Richter, you have been my mentor in so many areas, both academics and life. Thank you for your balance between theory and practice, saving the day with strain gauges, and lessons in when to persist and when to move on. To all of my committee members, you have brought a rounded depth of insight to this dissertation. Dr. van den Bogert, thank you for advising me on whether I am on the right track with human motion in real life or simply making mathematical achievements. Dr. Scheerer, thank you for always holding the practical in front of me. I will always ask “why does it matter?” and “how can I get it to the right audience for it to make an impact?”. Dr. Shao, I so appreciate your patience in sifting and sitting through hours of engineering jargon to provide thoughtful feedback on the math. Dr. Simon, you gave me the chance of a lifetime to get started in the prosthesis project. I would not be here today if you had not gone looking for me as an undergrad two years after we had met just once. It has been an optimal journey into and through graduate school.

I would like to recognize the support of the National Science Foundation through grants 1344954 and 1544702. It has provided me the freedom to pursue a variety of directions in my research for which I am very grateful.

To my fellow labmates, Poya Khalaf, Humberto de las Casas Zolezzi, Amin Ghorbanpour, Erivelton Gualter dos Santos, and Santino Bianco, it has been some adventure. Thank you for being a great team!

The completion of this dissertation would not have been possible without the support of Dr. Hardin and her team at the Louis Stokes Cleveland VA Medical Center. My deepest appreciation also goes to the gracious volunteer who offered his time and insight testing the prosthesis prototype.

I would like to extend my sincere gratitude to David Epperly, who is a genius at all things fabrication.

I cannot begin to fully express my appreciation to my family. We have walked together throughout this process—the good, the bad, the complicated, and the crazy. I would never have arrived here without you.

Soli Deo gloria!

SIMULATION AND CONTROL AT THE BOUNDARIES  
BETWEEN HUMANS AND ASSISTIVE ROBOTS

HOLLY E. WARNER

**ABSTRACT**

Human-machine interaction has become an important area of research as progress is made in the fields of rehabilitation robotics, powered prostheses, and advanced exercise machines. Adding to the advances in this area, a novel controller for a powered transfemoral prosthesis is introduced that requires limited tuning and explicitly considers energy regeneration. Results from a trial conducted with an individual with an amputation show self-powering operation for the prosthesis while concurrently attaining basic gait fidelity across varied walking speeds.

Experience in prosthesis development revealed that, though every effort is made to ensure the safety of the human subject, limited testing of such devices prior to human trials can be completed in the current research environment. Two complementary alternatives are developed to fill that gap. First, the feasibility of implementing impulse-momentum sliding mode control on a robot that can physically replace a human with a transfemoral amputation to emulate weight-bearing for initial prototype walking tests is established. Second, a more general human simulation approach is proposed that can be used in any of the aforementioned human-machine interaction fields.

Seeking this general human simulation method, a unique pair of solutions for simulating a Hill muscle-actuated linkage system is formulated. These include using the Lyapunov-based backstepping control method to generate a closed-loop tracking simulation and, motivated by limitations observed in backstepping, an optimal control solver based on differential flatness and sum of squares polynomials in support of receding horizon controlled (e.g. model predictive control) or open-loop simulations.

The backstepping framework provides insight into muscle redundancy resolution. The optimal control framework uses this insight to produce a computationally efficient approach to musculoskeletal system modeling. A simulation of a human arm is evaluated in both structures. Strong tracking performance is achieved in the backstepping case. An exercise optimization application using the optimal control solver showcases the computational benefits of the solver and reveals the feasibility of finding trajectories for human-exercise machine interaction that can isolate a muscle of interest for strengthening.

# TABLE OF CONTENTS

	Page
ABSTRACT . . . . .	v
LIST OF FIGURES . . . . .	xi
LIST OF TABLES . . . . .	xiv
CHAPTER	
I. INTRODUCTION . . . . .	1
1.1 Motivation . . . . .	1
1.2 Problem Statement . . . . .	2
1.3 Specific Aims . . . . .	2
1.4 Dissertation Organization . . . . .	4
PART 1: POWERED TRANSFEMORAL PROSTHESIS CONTROL AND EXPERIMENTS . . . . .	5
II. POWERED PROSTHESIS WITH FORCE-MODULATED IMPEDANCE AND ENERGY REGENERATION . . . . .	6
2.1 Introduction . . . . .	6
2.2 Energy Regenerative Prosthesis Model . . . . .	10
2.3 Force-Modulated Impedance Control Method . . . . .	13
2.4 Prosthesis Prototype . . . . .	17
2.5 Remarks . . . . .	20
III. IMPULSE-MOMENTUM SLIDING MODE CONTROL AND APPLICATION TO A PROSTHESIS TEST ROBOT . . . . .	21



3.1	Introduction . . . . .	21
3.2	Test Robot Vertical Degree of Freedom Model . . . . .	24
3.3	Impulse-Momentum Sliding Mode Control . . . . .	26
3.4	Terminal Sliding Mode Control . . . . .	28
3.5	Switching Laws . . . . .	29
3.6	Results and Discussion . . . . .	31
3.6.1	Simulations . . . . .	32
3.6.2	Experiments . . . . .	32
3.7	Remarks . . . . .	35
IV.	WALKING TRIALS WITH THE POWERED TRANSFEMORAL PROSTHESIS . . . . .	37
4.1	Introduction . . . . .	37
4.2	Experimental Procedure for Human Trials . . . . .	37
4.3	Gait Data Analysis and Results . . . . .	39
4.4	Prosthesis Sensor Data Analysis and Results . . . . .	44
4.5	Test Subject Feedback . . . . .	51
4.6	Remarks . . . . .	51
PART 2:	MUSCULOSKELETAL MODELING FOR HUMAN-MACHINE INTERACTION SIMULATION . . . . .	53
V.	BACKSTEPPING CONTROL OF A MUSCLE-ACTUATED LINKAGE HUMAN SIMULATION . . . . .	54
5.1	Introduction . . . . .	54
5.2	Hill Muscle Model as Actuator . . . . .	57
5.2.1	Hill Muscle Model . . . . .	57
5.2.2	Equilibrium Properties . . . . .	60
5.2.3	Model Normalization . . . . .	61

5.3	Antagonistic Muscle Pair Actuated Mass . . . . .	62
5.3.1	Muscle Actuated Mass Model . . . . .	62
5.3.2	Overview of Backstepping Control . . . . .	63
5.3.3	Pure-Feedback (Modified Strict-Feedback) Dynamics .	70
5.3.4	Pole Placement Based Backstepping Control . . . . .	71
5.3.5	Simulation and Results . . . . .	75
5.3.6	Discussion and Summary of Findings . . . . .	80
5.4	Muscle-Actuated Linkage . . . . .	81
5.4.1	Muscle Actuated Linkage Model . . . . .	81
5.4.2	Inverse Dynamics Based Backstepping Control . . . . .	85
5.4.3	Simulation and Results . . . . .	92
5.4.4	Discussion and Summary of Findings . . . . .	104
5.5	Remarks . . . . .	105
VI.	OPEN LOOP MUSCLE-ACTUATED LINKAGE HUMAN SIMU- LATION . . . . .	107
6.1	Introduction . . . . .	107
6.2	Differential Flatness of Musculoskeletal Systems . . . . .	110
6.2.1	Example: Differential Flatness of Antagonistic Muscle Pair Actuated Mass System . . . . .	112
6.3	Sum of Squares Representation of Muscle Co-contractions . .	113
6.3.1	Including Interaction Forces . . . . .	116
6.4	Validating the Open Loop Solver . . . . .	116
6.5	Application to Optimal Exercise . . . . .	123
6.5.1	Exercise Machine and Human Arm Interaction Model	124
6.5.2	Trajectory Generation . . . . .	125
6.5.3	SOS Solution Reduced to a Linear Program . . . . .	126
6.5.4	Trajectory and Impedance Optimization . . . . .	128

6.6	Results . . . . .	133
6.6.1	Selected Optimal Exercise Trials . . . . .	134
6.6.2	Constant Co-contractions . . . . .	157
6.6.3	Computational Efficiency . . . . .	158
6.7	Remarks . . . . .	159
6.7.1	Exercise Optimization . . . . .	160
6.7.2	Receding Horizon Control . . . . .	160
VII.	CONCLUSION . . . . .	162
7.1	Summary . . . . .	162
7.2	Contributions . . . . .	164
7.3	Future Work . . . . .	166
	BIBLIOGRAPHY . . . . .	168
	APPENDIX . . . . .	189
A.	COPYRIGHTS AND PERMISSIONS . . . . .	190

## LIST OF FIGURES

Figure		Page
1.	Prosthesis prototype . . . . .	10
2.	Prosthesis system schematic . . . . .	11
3.	Schematic of prosthesis experimental setup . . . . .	18
4.	Instrumented prosthetic foot . . . . .	18
5.	CSU prosthesis test robot . . . . .	22
6.	Vertical drive mechanism of the prosthesis test robot . . . . .	25
7.	Tracking and force trajectories for the prosthesis test robot walking trial	34
8.	Control input and sliding functions for the prosthesis test robot walking trial . . . . .	35
9.	Volunteer test subject wearing the prosthesis prototype . . . . .	38
10.	Kinematic and kinetic results for walking at three speeds . . . . .	40
11.	Change in energy for individual joints of the leg subsystem . . . . .	43
12.	Average control signal $r$ for walking at 0.6 m/s . . . . .	45
13.	Average control signal $r$ for walking at 0.75 m/s . . . . .	46
14.	Average control signal $r$ for walking at 0.9 m/s . . . . .	46
15.	Average normalized shank force measurement . . . . .	47
16.	Internal energy balance for walking at 0.60 m/s . . . . .	48
17.	Internal energy balance for walking at 0.75 m/s . . . . .	48
18.	Internal energy balance for walking at 0.90 m/s . . . . .	49
19.	Net increase in capacitor bank voltage during variable speed walking	50
20.	Hill muscle model . . . . .	58
21.	Mass system actuated by an antagonistic pair of muscles . . . . .	62

22.	Motor driven bob pendulum . . . . .	65
23.	Simulation results for bob pendulum under backstepping control . . .	69
24.	Tracking performance of the two muscle system . . . . .	78
25.	Two muscle system control signals and computed muscle activations .	79
26.	Errors $w_1$ and $w_2$ converge to zero for the two muscle system . . . . .	79
27.	Two degree of freedom planar robot schematic . . . . .	82
28.	Block diagram of muscle-actuated linkage system dynamics and back- stepping control levels . . . . .	92
29.	Locations of simulated muscles . . . . .	94
30.	Least Squares Solution: Tracking . . . . .	97
31.	Least Squares Solution: Tendon length states . . . . .	97
32.	Least Squares Solution: Synthetic controls . . . . .	98
33.	Least Squares Solution: Control signals and activations . . . . .	99
34.	Least Squares Solution: Forces generated by each muscle . . . . .	99
35.	Constrained Optimization Solution: Tracking . . . . .	101
36.	Constrained Optimization Solution: Tendon length states . . . . .	101
37.	Constrained Optimization Solution: Synthetic controls . . . . .	102
38.	Constrained Optimization Solution: Control signals and activations .	103
39.	Constrained Optimization Solution: Forces generated by each muscle	103
40.	Vertical trajectory validation for optimal control solver . . . . .	119
41.	Right diagonal trajectory validation for optimal control solver . . . .	120
42.	Horizontal trajectory validation for optimal control solver . . . . .	121
43.	Left diagonal trajectory validation for optimal control solver . . . . .	122
44.	Exercise machine and arm tracing a trajectory . . . . .	124
45.	General ellipse trajectory . . . . .	126
46.	Process for a single trial of the exercise optimization problem . . . . .	133
47.	Trajectories and $F_{ext}$ found to maximize Anterior Deltoid . . . . .	137

48.	Muscle activations resulting from maximizing Anterior Deltoid . . . .	138
49.	Tendon forces resulting from maximizing Anterior Deltoid . . . . .	139
50.	Trajectories and $F_{ext}$ found to maximize Posterior Deltoid . . . . .	141
51.	Muscle activations resulting from maximizing Posterior Deltoid . . . .	142
52.	Tendon forces resulting from maximizing Posterior Deltoid . . . . .	143
53.	Trajectories and $F_{ext}$ found to maximize Biceps Brachii . . . . .	145
54.	Muscle activations resulting from maximizing Biceps Brachii . . . . .	146
55.	Trajectories and $F_{ext}$ found to maximize Triceps Brachii (long head) .	148
56.	Muscle activations resulting from maximizing Triceps Brachii (long head)	149
57.	Trajectories and $F_{ext}$ found to maximize Triceps Brachii (short head)	151
58.	Muscle activations resulting from maximizing Triceps Brachii (short head) . . . . .	152
59.	Muscle co-contractions resulting from maximizing Triceps Brachii (short head) . . . . .	153
60.	Trajectories and $F_{ext}$ found to maximize Brachialis . . . . .	155
61.	Muscle activations resulting from maximizing Brachialis . . . . .	156
62.	Permissions for Figures 1 and 9 . . . . .	190
63.	Permissions for Figure 10 . . . . .	191

# LIST OF TABLES

Table	Page
I. Prosthesis test robot parameters . . . . .	26
II. Prosthesis control gains . . . . .	39
III. Muscle-actuated mass system simulation parameters . . . . .	77
IV. Physical parameters of the linkage scaled to a human arm . . . . .	94
V. Muscle-actuated mass system simulation parameters . . . . .	95
VI. Muscle and moment arm properties selected for the human arm . . .	95
VII. Average time required to complete the validation problem . . . . .	118
VIII. Parameter range limits for exercise optimization . . . . .	132
IX. Optimal trajectory and impedance parameters for exercise solutions .	135

# CHAPTER I

## INTRODUCTION

### 1.1 Motivation

Advancing simulation and control methodologies have expanded the realm of human-machine interaction. Among the varied applications of this field, assistive robotics is particularly inspiring. Some systems that fall within this category include advanced exercise machines [16, 97], powered prostheses [22, 75, 109, 155], and rehabilitation robots [3, 65].

The nature of boundaries between humans and assistive robots can be classified in two ways: (1) a measure of seamless integration and (2) a barrier providing support for system development and human safety. For the first case consider a powered prosthesis. It is perhaps the most intimate, daily-use application of human-robot interaction. In this context it is desirable for the boundary between the human and assistive robot to become increasingly blurred, signaling movement toward better emulation of the natural system that the robot is replacing. Regarding the second case, a trend toward developing intermediate machines to replace the human in early trials, such as gait emulators for lower-limb prostheses, suggests a recognized need to broaden the boundary between ideation and human trials [10, 26, 27, 73, 74]. Such



testing iterations should support development by increasing repeatability [35] and promote the examination of extreme conditions, among other benefits.

## 1.2 Problem Statement

This dissertation focuses on two unique but not entirely independent problems. The first question is exclusively related to powered above-knee prostheses. The current state of the art for individuals with above-knee amputations offers passive prostheses that produce a variable damping and stiffness at the joint. These solutions are inadequate to replicate able-bodied gait, leading to ongoing health concerns [29, 105, 115]. While efforts are being made to improve prosthesis performance by adding active components such as motors, two of the foremost obstacles barring powered prostheses from progressing toward becoming mainstream solutions for individuals with transfemoral amputations are control complexity and insufficient battery life [121]. The second challenge undertaken by this dissertation initially arose from observing the limited capacity to test ideas in the field of prosthetics prior to human trials [31]. Further investigation revealed a more general deficit in simulation methods for human and machine interaction. This shortcoming limits opportunity for pre-prototype study, including optimization, and induces increased safety hazards.

## 1.3 Specific Aims

**Objective 1: To design a simplified powered prosthesis controller and prototype with energy regeneration.** A powered prosthesis design and related controller will be developed with a focus on achieving natural gait, control simplicity, and energy regeneration. The resulting prosthesis will be tested by a volunteer with an amputation. Gait efficacy and energy usage will be evaluated against passive prosthesis data and published able-bodied data.

**Objective 2: To extend impulse-momentum sliding mode control to emulate weight-bearing walking gait with a robot for prosthesis mechanical testing.** Research on an impulse-momentum sliding mode controller recently introduced in the literature will be continued. The specific application of a prosthesis test robot motivates the concept such that a realistic gravity and inertia component can be experienced by the prosthesis being tested. This control law is active when the prosthetic foot contacts the ground. Control is given to a tracking controller during the non-contact phase. The control system will be extended from a vertical stomping motion to walking gait by development of an improved control switching law.

**Objective 3: To develop a framework for closed-loop muscle-actuated linkage simulation of a human.** An intermediate model defined as a two-muscle actuated mass system will be considered to expound upon the implications of redundant, antagonistic muscle actuators. A simulation environment where, for example, a human arm or leg can be constructed as a robotic linkage actuated under backstepping control by Hill muscle models will be then developed. Two methods of resolving muscle redundancy will be investigated. Application to an arm model will be validated against a published simulation.

**Objective 4: To establish an efficient open-loop musculoskeletal system solver.** A novel parameterization based on differential flatness and sum of squares polynomials of muscle-actuated linkage dynamics will be developed. The method will be evaluated by comparison to published data and application to an optimal exercise problem.

## 1.4 Dissertation Organization

Each chapter begins with the relevant literature review and further motivation for the individual topics.

**Part 1** relates the design and validation of a powered prosthesis, Objectives 1 and 2.

- **Chapter II** details the development of the prosthesis control method from impedance control fundamentals while explicitly considering energy regeneration (Objective 1). The prototype hardware is also introduced.
- **Chapter III** presents Objective 2, impulse-momentum sliding mode control based gait emulation, considering both theory and implementation.
- **Chapter IV** completes Objective 1 by describing the walking trials conducted with an individual with an amputation and examines the results.

**Part 2** develops simulation methods for human-machine interaction systems, Objectives 3 and 4.

- **Chapter V** chronicles the construction of a closed-loop human simulation including muscle dynamics under backstepping control. Special attention is given to the resolution of actuator (muscle) redundancy. Results suggest the necessity of prediction for control.
- **Chapter VI** considers an optimal control solver for musculoskeletal dynamics that can be used for open-loop human-machine interaction studies or prediction for control. The model is validated against published electromyography data, and application to an optimal exercise problem is explored.

PART 1:

POWERED TRANSFEMORAL PROSTHESIS CONTROL AND EXPERIMENTS

## CHAPTER II

### POWERED PROSTHESIS WITH FORCE-MODULATED IMPEDANCE AND ENERGY REGENERATION

#### 2.1 Introduction

Passive prostheses of various forms have long provided mobility to individuals with transfemoral amputations, from the “peg leg” of the past to the mechanical knees or micro-processor managed variable damping knees of today [50]. Though progress has been made, regardless of the form, all of these prostheses lack an integral component of the natural leg, namely the muscles. Passive prostheses do not provide a means of joint actuation. The result is energetically costly and asymmetric gait. One study reports that individuals with transfemoral amputations walk at one-half of the speed of able-bodied individuals while exerting 65% more energy [142]. This leads to inactivity, in general, for people with a transfemoral amputation. Consequentially, they are prone to certain health risks. In the case of individuals with amputations due to vascular causes (artery disease, diabetes, etc.), these conditions already existed and become more prominent. These individuals are 50% more likely to lose the opposite leg in two to three years; within less than five years of an amputation, they are 55% more likely to lose their lives. Perhaps less shocking but still considerable concerns

for all those with such an amputation are the health issues resulting from asymmetric gait (limping) such as osteoarthritis, back pain, and others that reduce quality of life over time [29, 115]. It is generally assumed that these risks should decrease as prosthesis development moves closer to emulating the natural leg. Accordingly, the appropriate next step in the development of prostheses would be integrating powered actuation, replacing the missing muscles [44, 89].

The creation of powered prostheses opens wide the question of control, for which options abound. Perhaps the most common and broadly successful approach in the current literature is impedance control with a finite-state machine to vary gains [6, 38, 47, 68, 69, 77, 119–122, 141]. Typically, the gait cycle is divided into segments, each of which have a minimum of three gains—an associated stiffness, spring equilibrium parameter, and damping. For varying the speed or task, such as traversing slopes or stairs, a look-up table associating sets of gains with each pre-programmed speed or task is generated. In addition to tuning these gains, switching laws must be assigned, and user intent recognition must be established. Some work has added further variation to the gains by scaling them according to real-time kinematic or kinetic measurements [25, 110]. Indeed, tuning the gains associated with these methods quickly becomes excessive, particularly considering that the true end-user of the control interface is not the design team but rather the clinical team.

Alternatives to impedance control have also been studied, primarily stemming from the field of bipedal robotics. In purposeful contrast to the finite state impedance controllers, this work tends toward unifying controllers, at most breaking the gait cycle down into only swing (off contact) and stance (ground contact) phases. Control laws like the one described in [154] based on recreating human-like trajectories have found good success in transitioning from the discipline of bipedal robotics to prostheses. However, it seems likely that this method will suffer from increased complexity upon expanding the catalog of desired motions beyond walking gait. Alternatively,

reference [32] summarizes work done on control based on a single phase variable, the center of pressure of the prosthetic foot. Concerns regarding robustness are identified by this work; for example, if a person shifts too far forward while standing, the knee will be activated to flex. Considering the same concept with thigh angle as the phase variable, these concerns are not mentioned, but increasing complexity upon adding activities once again becomes relevant [23,93]. While the current state of these controllers allows for some variation such as changes in speed and in some cases incline, they are generally limited to one periodic motion.

A second question arises when looking toward powered prostheses; that is, they require an embedded power source. With recent advances in battery technology, powered transfemoral prostheses have entered the realm of marginal feasibility, hence the market currently offers limited options. For the Power Knee up to 12 hours of operation are possible [86]. However, this is dependent on the level of activity, and actual operation times have been reported to be between 5 and 7 hours [33]. Similarly, the Empower<sup>TM</sup>MP Foot reaches about eight hours maximum [87]. Within the research realm several platforms have been presented as well. For example, the Vanderbilt prosthesis, including both powered knee and ankle joints, provides about 1.8 hours of walking activity or 9-12 km [119,121]. For an active individual these designs, while providing increased ability to complete some previously unattainable tasks such as climbing stairs with alternating feet and perhaps reducing energy for many activities of daily living, limit the individual using the device by requiring constant attention to the prosthesis' power requirements. Frequent recharging, which requires hours, or carrying spare batteries is an unpleasant consequence of these benefits.

In referring to able-bodied gait, the answer as to how to extend prostheses' power storage longevity seems evident. In [143] power flows for both the knee and ankle are analyzed for several walking speeds. Indeed, for a portion of the gait cycle the

knee acts as a brake, absorbing energy. Much of this energy is dissipated as heat in the surrounding tissues, and some is stored in the tendons, which act in a spring-like manner. Because neither of these options must occur in a prosthetic knee, it seems prudent to strive to recover this energy, a process termed energy regeneration. An attempt to do just this is documented in the 1980's by a series of dissertations and theses from the Massachusetts Institute of Technology (MIT) [45,106,123]. However, the capacitor technology at that time limited the prosthesis' feasibility. More recently, efforts toward realizing energy regeneration in prosthetic leg joints have been revisited. Through the use of various mechanisms energy regeneration for the purpose of actuator augmentation has been realized [39,103]. Looking at electrical energy recovery, [130] recognizes the opportunity for energy regeneration and identifies an allowable range for knee joint damping. These findings are secondary to the goals of these projects, however, and appear to have limited further development, leaving energy regeneration in prostheses in practically the same state as it was in the 1980's [67].

The described state of the literature regarding powered transfemoral prostheses suggests that two features of prosthesis design be explicitly addressed in the development of such a prosthesis; these are simplified control and energy regeneration. Within the context of a broader prosthetics project at Cleveland State University (selected publications: [20,24,55,100,141]), one such design was developed and taken through the prototyping and initial testing stages by the author in collaboration with Poya Khalaf. This chapter develops the theory behind this prosthesis and its prototyping, which has been published in [59]. Chapters III and IV focus on the design and implementation of mechanical and human tests completed with this prosthesis and evaluate its performance.



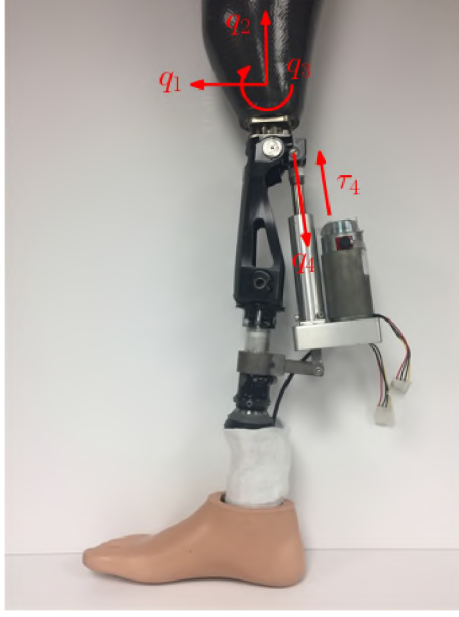


Figure 1: Prosthetic knee mounted between a typical socket and an Ottobock Triton Vertical Shock foot © 2018 ASME [59]

## 2.2 Energy Regenerative Prosthesis Model

The prosthetic knee joint actuated by a DC motor through action of a lead screw is shown in Figure 1. This system, including the human, can be modeled as a four degree of freedom robot with equation of motion

$$D_0(q)\ddot{q} + C(q, \dot{q})\dot{q} + R_0(q, \dot{q}) + g(q) + \tau_{ext} = \tau, \quad (2.1)$$

where  $D_0(q)$  is the inertia matrix,  $C(q, \dot{q})$  is the Coriolis matrix,  $R_0(q, \dot{q})$  is the damping, which could be nonlinear,  $g(q)$  is the gravity vector,  $\tau_{ext}$  is a vector of external forces and moments when reflected to the individual joints, and  $\tau$  is a vector of the input forces and torques. The vector of four generalized coordinates  $q$  represents the horizontal, vertical, and rotational degrees of freedom of the human hip and the degree of freedom causing flexion of the prosthetic knee, as depicted on the far left side of Figure 2. The ankle is passive, composed of a leaf spring and rubber damper, and accordingly, is not identified as an additional degree of freedom.

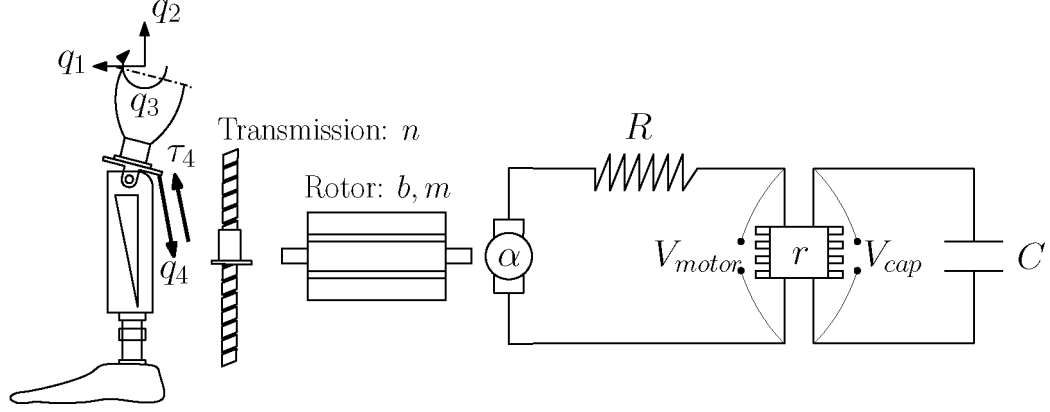


Figure 2: System schematic including prosthesis and regenerative drive (lead screw, DC motor, armature resistance, motor driver, and supercapacitor power storage)

While the human controls the first three degrees of freedom, the knee is driven by an actuator; see Figure 2. Moving from left to right, the prosthesis body and screw transmission with ratio  $n$  are shown. The screw is driven by a DC motor with damping  $b$ , inertia  $m$ , and torque constant  $\alpha$ . The armature resistance  $R$  is in series with the motor driver, which is ideally modeled by its duty ratio  $r$  as  $V_{motor} = rV_{cap}$  with  $r \in [-1, 1]$ . Parameter  $r$  is used as the final control input. Motivated by their successful use in motor vehicles, a bank of supercapacitors, denoted by capacitance  $C$ , are used as the sole power storage unit for the system [19]. Particularly when excess energy becomes available from the knee, the storage element must be capable of receiving it quickly. Supercapacitors provide a means of exchanging energy rapidly when compared with batteries [12].

Under this drive system, the four degrees of freedom can be categorized according to their energy sources based on the framework developed in [56–58, 95]. The first three degrees of freedom are under the control of the human, who also provides energy to the system. They are termed fully active. In contrast, the fourth degree of freedom is semiactive; it contains an internal means of storing energy (supercapacitors), allowing it to capture energy transmitted through the system and release energy to the system.

The actuator dynamics can be written as

$$\tau_4 = -mn^2\ddot{q}_4 - \left(bn^2 + \frac{(\alpha n)^2}{R}\right)\dot{q}_4 + \frac{\alpha nr}{R}V_{cap} \quad (2.2)$$

Augmenting the equation of motion (2.1) with (2.2) yields the final model

$$D(q)\ddot{q} + C(q, \dot{q})\dot{q} + R(q, \dot{q}) + g(q) + \tau_{ext} = u, \quad (2.3)$$

where matrix and vector elements are updated as follows:

$$D_{[4,4]} = D_{0[4,4]} + mn^2\ddot{q}_4 \quad (2.4)$$

$$R_{[4]} = R_{0[4]} + \left(bn^2 + \frac{(\alpha n)^2}{R}\right)\dot{q}_4 \quad (2.5)$$

and the control vector  $u$  is determined by the human for the first three degrees of freedom and is

$$u_4 = \frac{\alpha nr}{R}V_{cap} \quad (2.6)$$

for the fourth degree of freedom. Clearly, this is not the typical case of modulating the motor's voltage from an external supply with constant voltage. Rather, the source is internal and varying, another feature of a semiactive degree of freedom. By applying semiactive virtual control as described in [56, 57, 95, 100], any control law, termed the virtual control law  $\tau^d$ , can be selected for  $u_4$ . Setting  $u_4$  equal to  $\tau_d$  and solving for the parameter  $r$ , which can be modulated, gives a virtual matching law

$$r = \frac{R}{\alpha n V_{cap}}\tau^d \quad (2.7)$$

correlating  $r$  to the virtual control for any combination of motor and transmission parameters. According to [95], as long as the virtual matching law has a solution, any

properties, for example stability, held by the virtual control law will be transmitted to the system. The matching law for the knee always has a solution if there is sufficient capacitor voltage and accurate knowledge of parameters  $\alpha$ ,  $n$ , and  $R$ .

While considering the system dynamics, a measure of the energy regenerated at the knee joint can be developed. It is reported in [58], starting from integrating the capacitor power between times  $t_1$  and  $t_2$

$$\Delta E = \int_{t_1}^{t_2} V_{cap} i_{cap} dt, \quad (2.8)$$

where  $i_{cap}$  is the capacitor current, that the energy stored under a chosen virtual control law for a semiactive system is

$$\Delta E = \int_{t_1}^{t_2} \left( \tau^d \dot{q}_4 - \left( \frac{\tau^d}{\alpha n} \right)^2 R \right) dt. \quad (2.9)$$

Positive  $\Delta E$  indicates energy regeneration. It can be seen that the integrand is the difference between the mechanical power at the joint and the electrical losses (of form  $i^2 R$ ) and is only dependent on the parameters associated with the motor and transmission, the chosen control law, and the trajectory of the knee.

### 2.3 Force-Modulated Impedance Control Method

Based on the successful trials reported in the literature, the virtual control law  $\tau^d$  was selected as an impedance type controller. The concept of impedance control can be summarized as controlling the dynamic interaction between the controlled device and the environment, in this case the human-prosthesis and prosthesis-ground interfaces [41–43]. For example, if the selected impedance is just of a stiffness type, increasing displacement of the joint would result in an increasing force response from the device; it would feel like a spring. Similarly, inertia and damping features can be generated.

Reference [118] identifies the action of the knee to be sufficiently modeled by a combination of stiffness and damping. The ability to select a suitable design for the physical prosthesis' weight and mass distribution also supports that including inertia is unnecessary. Accordingly, the proposed control law is constructed as a combination of stiffness and damping terms

$$\tau^d = -(B_h + B)\dot{q}_4 - \frac{F}{F_s}Kq_4 - K_s(q_4 - q_4^\circ) \quad (2.10)$$

where  $B_h$  and  $B$  are damping coefficients,  $F$  is the shank force,  $F_s$  is a constant for normalizing,  $K$  and  $K_s$  are stiffness coefficients, and  $q_4^\circ$  is the equilibrium point for spring  $K_s$ . Each of these terms and the rationale for their selection will be explained by separating the gait cycle into stance (contact) and swing (off-contact) phases.

For stance phase the control law is dominated by the  $K$  stiffness term because the knee is near its equilibrium point and  $K$  by tuning is large relative to  $K_s$

$$\tau^d \approx -\frac{F}{F_s}Kq_4. \quad (2.11)$$

It was hypothesized that a measurement representative of the force between the foot and ground could modulate the stiffness of the knee, making the impedance a continuous function of the gait kinematics and kinetics as was suggested rather generally at the conclusion of [136]. Practically, it would at minimum distinguish between contact and off-contact. More broadly, it can be observed that as the prosthetic foot contacts the ground, the opposing leg is unloading, implying an increase in force through the prosthetic leg. The reverse effect occurs when unloading the prosthetic leg. Therefore, increased force applied to the prosthesis by its user yields increased support. This modulation leads to predictable powered knee actuation, yet allows the knee to soften as needed to prepare for swing. To generate such a measurement internal to the prosthesis system, the force transmitted through the shank  $F$  was used. Dividing

this measurement by normalization factor  $F_s$ , which is the force associated with the user's full weight under static conditions, allows smooth modulation of  $K$ . The final result is that for increased knee flexion and increased contact force, the knee will provide greater torques to straighten the prosthesis. This result is distinctly different from the slow sinking motion generated by a passive hydraulic knee. Extending this concept beyond gait, one could conceive that climbing stairs with alternating legs might become possible in this framework.

When the prosthesis is in swing phase, the foot is no longer in contact with the ground, and  $F$  is zero, leading to the reduction of the control law (2.10) to

$$\tau^d = -(B_h + B)\dot{q}_4 - K_s(q_4 - q_4^\circ). \quad (2.12)$$

The gain  $K_s$  defines a spring that applies force to move the knee back to equilibrium  $q_4^\circ$ , typically full knee extension. While this term is technically active in both stance and swing phases, it is typically small or zero because the purpose of this term is to provide the individual with aid in extending the knee, if needed. The kinetic energy of the knee at the beginning of swing phase should provide for the majority of the energy required for the extending motion. However, in the case that the use of  $K_s$  is required, it can be checked using (2.9) that, under the assumption of periodicity, the only energy usage by this portion of the control law is associated with the  $i^2 R$  portion of (2.9).

Gain  $B_h$  was included for practical purposes. The prosthesis design includes a hard stop at full extension. To prevent jarring of the individual wearing the device, some additional damping was included according to

$$B_h = \begin{cases} b_h, & q_4 < q_{threshold} \\ 0, & q_4 \geq q_{threshold} \end{cases} \quad (2.13)$$

just at the end of the swing phase, as determined by  $q_{threshold}$ . Energy usage for this purpose could be avoided if an insert were designed for the prototype system to provide the same effect.

Returning to the idea of energy regeneration, swing phase has limited energy usage and significant energy availability [143]. The damping term  $B$  is included to capture this energy. Under the assumption that  $\tau_d \approx -B\dot{q}_4$ , substitution of this term into (2.9) gives

$$\Delta E_s = \int_{t_1}^{t_2} - \left( B + \frac{R}{(\alpha n)^2} B^2 \right) \dot{q}_4^2 dt. \quad (2.14)$$

Clearly, energy regeneration takes place when  $-\frac{(\alpha n)^2}{R} < B < 0$ , leading to the conclusion that the coefficient  $B$  must be negative. Negative damping would reduce the physical system's overall damping. Assuming that negative damping in the given range will not cause system instability and that the maximum energy regeneration is independent of  $\dot{q}_4$ , differentiating (2.14) with respect to  $B$ , setting it equal to zero, and solving for  $B$  gives the optimal value

$$B^* = -\frac{(\alpha n)^2}{2R}. \quad (2.15)$$

Using this value for the damping gives the optimal amount of energy regenerated

$$\Delta E_s^* = \int_{t_1}^{t_2} \frac{(\alpha n)^2}{4R} \dot{q}_4^2 dt. \quad (2.16)$$

Tuning the controller requires the selection of the following five gains and parameters:  $b_h$ ,  $q_{threshold}$ ,  $K$ ,  $K_s$ , and  $q_4^o$ . The value of  $B$  is determined based on system parameter measurements from (2.15). In addition to reducing the number of parameters by potentially an order of magnitude relative to prior work, the remaining parameters are intuitive to tune. Virtual damping  $b_h$  is chosen such that it is slightly larger in magnitude than the value calculated for  $B$  so that it overrides the negative

damping. The distance  $q_{threshold}$  from full extension where the hard stop prevention damping becomes active is selected as the smallest value where the hard stop is no longer evident; for the prosthesis prototype this condition was associated with noise reduction and the comfort of the individual wearing the device. In general  $q_{threshold}$  is a few millimeters of screw travel. The value of  $K$  determines how supportive the knee feels. It is selected based on the user's feedback.  $K_s$  and  $q_4^o$  are adjusted until the knee fully extends under the individual's control. For the trial conditions  $K_s$  was able to be set to zero.

## 2.4 Prosthesis Prototype

A prosthesis capable of controlled powered actuation and energy regeneration was constructed from off-the-shelf components to provide preliminary testing of the previously presented ideas. A schematic of the overall test system setup is provided in Figure 3. The body of the prosthesis supports the user's weight and includes standard pyramid adaptors for connection to the individual's socket and selected foot. To reduce power usage, the knee is capable of self-locking at equilibrium ( $q_4 = \dot{q}_4 = 0$ ) if the individual wearing it so chooses by shifting his or her center of mass. For the tests completed, an Ottobock Triton Vertical Shock foot was used. To provide shank force feedback, the foot was instrumented with two strain gauges; see Figure 4. The strain gauge signals were processed by custom built circuitry. First, the signal was passed to a Wheatstone bridge. The positive and negative outputs of the bridge were sent to an operational amplifier voltage follower. The outputs of these two voltage followers were processed by an operational-amplifier differential amplifier, resulting in a scaled difference. Lastly, this signal was given to a second order low pass filter constructed with an operational amplifier. The output of this filter was used as the final force measurement signal.

To calibrate the force measurement, the foot was initially connected to a short rod



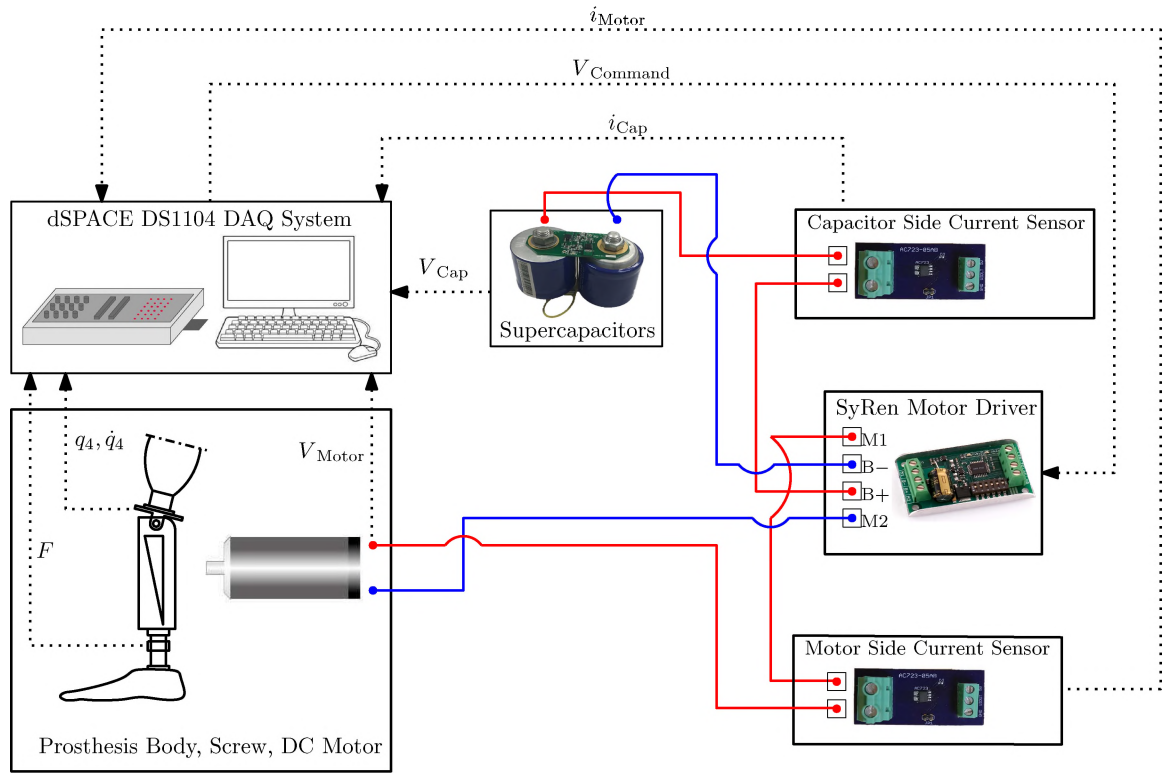


Figure 3: Schematic of the experimental setup for the prosthesis prototype. Solid lines signify power transmission. Dotted lines denote signal transmission



Figure 4: Ottobock Triton Vertical Shock foot instrumented with two strain gauges

with a calibrated load cell at the opposite end. Forces emulating gait at magnitudes up to full body weight were manually applied through the load cell and rod fixture to generate dynamic calibration data. A least squares fit was performed for this data, resulting in a formula for the shank force that was composed of a linear sum of the individually scaled signals. The result of this calibration was in good agreement with the load cell output when plotted in real time, dynamically validating the shank force measurement.

Having established the prosthesis' structure, the actuation system can be addressed. A 12 V DC motor drives a lead screw via a 1:1 belt transmission (ULTRAMOTION). The shortening of the screw causes knee flexion by use of a four bar crank-slider linkage. Motor position is measured by an optical encoder, which is kinematically related to knee flexion angle. For calculation of the virtual damping  $B$ , the motor resistance and torque constant are  $R = 0.27 \, \Omega$  and  $\alpha = 0.031 \, \text{Nm/A}$ , respectively. A transmission ratio of  $n = 989.5 \, \text{rad/m}$  is associated with the screw.

The motor voltage is modulated by a SyRen 10 Amp four-quadrant motor driver from DimensionEngineering. Power is supplied to the driver from 4 Maxwell 2.7 V, 650 F supercapacitors (BCAP0650 P270 K04) connected in series by balancing circuitry (BKIT-MCINT). The voltage of the capacitors is measured in real time for use in the virtual control matching law. Much like the strain gauge signal, the measurement passes through individual voltage followers for the positive and negative leads and then is processed by a differential amplifier circuit built with an operational amplifier. To provide for analyzing the system's energy regeneration capacity, the current flowing between the capacitors and the motor driver and the current flowing between the motor driver and the motor were measured separately.

Control prototyping was implemented by use of a dSPACE DS1104 data acquisition board and ControlDesk software system. This system interfaces easily with MATLAB Simulink, where the controller was encoded. An output analog voltage sig-

nal was generated according to the motor driver’s specifications to correspond with the desired control signal. All necessary feedback and evaluative measurements were taken and recorded using the analog to digital capabilities of the dSPACE system; each measurement (except  $q_4$ ) was digitally filtered with a 24 Hz cutoff frequency. Note that this system implies that the prosthesis is currently only operational on a tether, by which it also connects to the capacitor power supply.

## 2.5 Remarks

A prototype powered knee prosthesis was developed with particular attention to a unifying control strategy and energy regeneration. The control law requires few tuning parameters while maintaining the impedance foundation that has been so successful in the literature. This controller explicitly considers energy regeneration, providing tuning guidelines to accomplish this goal. Additionally, the prototype itself was designed to make energy regeneration possible.

## CHAPTER III

### IMPULSE-MOMENTUM SLIDING MODE CONTROL AND APPLICATION TO A PROSTHESIS TEST ROBOT

#### 3.1 Introduction

Lower-limb prosthesis prototype testing, as previously referenced, is an area receiving attention in the literature. These applications [10, 26, 27, 73, 74, 98, 99] utilize control methods that are linear, including various combinations of proportional, integral, and derivative terms; nonlinear, such as sliding mode control; and one that is unspecified, though the description suggests a form of tracking control.

One example from among these systems has been constructed at Cleveland State University (CSU) in collaboration with The Cleveland Clinic. The details of this single-legged prosthesis test robot can be found in [98, 99]. It consists of two degrees of freedom, vertical hip displacement and thigh rotation. Any prosthesis of interest with standard connections can be installed and be made to walk along a treadmill with this system. Figure 5 shows the system configured with the prosthesis described in Chapter II.

Prior work with the hip robot has used a sliding mode controller to provide accurate tracking of pre-recorded human hip trajectories. This approach, while valuable

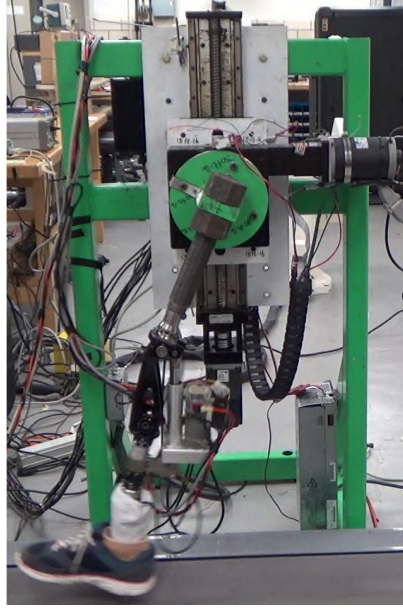


Figure 5: CSU prosthesis test robot walking with the prosthesis presented in Chapter II

for studying the kinematic response of a prototype, makes it difficult to collect data consistent with the dynamic forces that a lower-limb prosthesis would experience. Tracking controllers in general use as much force or torque as needed to make a given joint follow the desired trajectory. The result can be environmental impact forces, ground reaction forces in this case, that are unnatural.

To improve the contact forces associated with the CSU test robot, one work reports adapting the kinematic reference trajectory by evolutionary optimization with the error between a reference ground reaction force and the actual machine-generated ground reaction force as the cost function [14,15]. This process was stated to emulate the adaptation required from an individual with an amputation to walk with the prosthesis being tested and match able-bodied ground reaction force. Several features discourage the generalized use of this work, however. First, the adjustments made to the trajectories are likely dependent on the prosthetic knee and ankle/foot being tested; different combinations will lead to alternative trajectories. Long operation times are cited in this work to accomplish convergence, making it difficult to switch

prostheses. Second, it cannot be expanded to emulate individuals with differing body weights without first collecting new able-bodied data. Finally, it assumes that ground reaction force is the key to improved prosthetic gait. The opposite possibility is that improved prostheses lead to more natural ground reaction forces for those who use them. For a purely tracking solution to gait emulation, as previously described, this possibility is difficult to assess.

Gait studies provide an alternative option for attaining more natural ground reaction forces. Human gait is attributed to controlled falling behavior where the next foot is placed to halt the fall [135]. To achieve a fall-like condition, it seems sufficient to focus on the vertical axis of the robot, as this is the primary force-generating degree of freedom; it represents the weight of the body settling onto the prosthetic leg. It is proposed that by controlling this degree of freedom such that it appears as a pure mass during the ground contact portion of the gait cycle, human motion should be better achieved by the hip robot.

An established method, impedance control, that seeks to control the dynamic relationship between forces and tracking was initially experimented with to improve the motion of the test robot in this manner [41–43]. Typical implementations of impedance control within a robotic system require accurate force feedback. Due to issues with obtaining a sufficiently reliable force reading and the lack of robustness perceived in the attempted impedance control, an alternative control method was sought.

Work by Richter, Mobayen, and Simon [96] describes the early development of a sliding mode control approach to this problem. A purely vertical trajectory that emulates weight for a period and then lifts the leg for a period is considered. This cycle is split into contact and off-contact phases. Under the contact phase this work introduces impulse-momentum sliding mode control, which allows for weight emulation. For the off-contact phase a terminal sliding mode control for tracking the

vertical displacement of human gait reference data is applied.

Implementation of sliding mode control requires that a discontinuous function propel system states to a selected switching (sliding) surface where they must remain [21, 131]. This reaching process is robust to matched disturbances, and once the states arrive at the sliding surface, the system takes on lower-order dynamics and insensitivity to matched disturbances. For a tracking problem the sliding surface is commonly composed of a linear combination of the tracking error and derivatives of that error [113]. Under these circumstances, the behavior of the error is asymptotic convergence to zero, which might be too slow when switching back to tracking from the impulse-momentum sliding mode controller. Also, traditional sliding mode control is prone to chattering during reaching due to the discontinuous, high-frequency switching function. The method titled terminal sliding mode control improves upon these shortcomings [134]. By use of nonlinear, non-smooth differential equations for the error in the sliding mode and an extended switching law, the convergence time becomes finite. This eases alternating between the contact and off-contact controllers and reduces the opportunity for chattering.

Motivated by [96], the continuation of that work toward walking is discussed in this chapter. This chapter presents the detail of [96] along with the relevant simulation and experimental results for vertical motion alone in preparation for walking. A method to generate walking gait is then introduced and used to experimentally test the prosthesis prototype of Chapter II. These experiments show consistency in the response of the prosthesis but that the hip robot control requires additional development to better emulate human gait. Directions for improving and then extending of the impulse-momentum sliding mode control conclude the chapter.

### **3.2 Test Robot Vertical Degree of Freedom Model**

The vertical axis of the test robot can be described by Figure 6. The motor driver

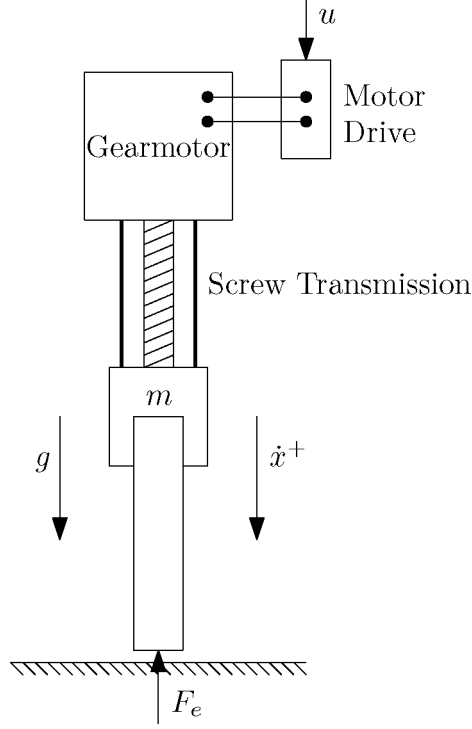


Figure 6: Vertical drive mechanism of the prosthesis test robot

is configured for torque control. The motor actuates a screw which initiates motion of the carriage along guiding rails. For this system the equation of motion is

$$m\ddot{x} + \delta(x, \dot{x}) = ku - F_e, \quad (3.1)$$

where  $x$  is the vertical position coordinate,  $\delta(x, \dot{x})$  represents the uncertainty associated with the friction within the mechanism,  $k$  is a constant containing the motor drive constant and transmission ratio,  $u$  is the control input, and  $F_e$  is the force generated by contact with the environment. Note that the control input has been augmented for gravity compensation  $u = u' + \frac{mg}{k}$  such that  $u'$  is the varying portion of the control input. Boundedness is assumed for the uncertainty  $\delta$

$$|\delta(x, \dot{x})| \leq \Delta, \quad (3.2)$$



Parameter	Value
$m$	146 kg
$k$	600 N/V
$F_f$	83 N
$b$	2570 Ns/m

Table I: Prosthesis test robot parameters [96]

where  $\Delta$  is a known constant. Additionally, it has been identified for the test robot that the friction follows

$$\delta(x, \dot{x}) = F_f \text{sign}(\dot{x}) + b\dot{x} + \delta'(x, \dot{x}), \quad (3.3)$$

where  $\delta'(x, \dot{x})$  is the remaining uncertainty, overall tightening the uncertainty bound. The system parameters are given in Table I, where they are reported after reflecting to the vertical coordinate and accounting for gearing. In particular note that mass  $m$  includes the inertia of the rotary mechanism amplified by a large transmission ratio. The actual vertical carriage mass is significantly less.

### 3.3 Impulse-Momentum Sliding Mode Control

It is desired that the controller during the contact phase emulate a pure mass under the influence of gravity and the contact force  $F_e$ . This can be described simply as

$$M\ddot{x} = W - F_e, \quad (3.4)$$

where  $W = Mg$ . Use of these dynamics to create a sliding surface requires that one differentiation reveal the control input under typical sliding mode control. However, (3.4) has zero relative degree to the control input  $u$ . Alternatively, the impulse-

momentum theorem realization of these dynamics provides a relative degree of one

$$M\dot{x}(t) - M\dot{x}(t_I) = \int_{t_I}^t (W - F_e(\tau))d\tau, \quad (3.5)$$

where  $t_{t_I}$  is the time of contact or impact. The sliding surface is then

$$s_2 = M\dot{x}(t) + \int_{t_I}^t (F_e(\tau) - W)d\tau - M\dot{x}(t_I) \quad (3.6)$$

Clearly, if  $s_2$  reaches zero and remains there, the system will emulate a pure mass under the influence of gravity and an environmental force.

According to the sliding mode control framework, a control law can be formed that will force  $s_2 = 0$  to occur in finite time and to then hold this condition regardless of the system uncertainty  $\delta(x, \dot{x})$ . To obtain this controller, the reaching law  $\dot{s} = -\eta_2 \text{sign}(s_2)$  is set equal to the time derivative of (3.6), and the acceleration  $\ddot{x}$  is eliminated by substitution of the system dynamics (3.1). All terms evaluated at time  $t_I$  are absorbed into the uncertainty. Solving for the control input gives

$$u_2 = -\frac{1}{k}[r(\eta_2 \text{sign}(s_2) - W) + (r - 1)F_e], \quad (3.7)$$

where  $r = \frac{m}{M}$ . The parameter  $\eta_2$  is used to tune the control law. To ensure stability of  $s_2$  under the Lyapunov function  $V_2 = \frac{1}{2}s_2^2$  requires  $\eta_2 \geq \Delta$  if  $\eta_2 > 0$  is assumed as shown by the Lyapunov derivative evaluated along the closed-loop trajectory of  $s_2$  after simplification

$$\dot{V}_2 = -s_2(\eta_2 \text{sign}(s_2) - \Delta). \quad (3.8)$$

By integration of the reaching law, it can be seen that for  $s_2(t_I) > 0$  the reaching time  $t_R$  follows  $t_R \leq \frac{s_2(t_I)}{\eta_2}$ . Similarly, for  $s_2(t_I) < 0$ ,  $t_R \geq \frac{-s_2(t_I)}{\eta_2}$ , leading to the conclusion that the reaching time is finite. Also, omitted steps imply  $t_R > t_I$ , which is consistent with the circumstances.

Under the case where there is known information about the viscous damping in the system ( $\delta$ ), the test robot can be modeled by adding damping with coefficient  $b$  as

$$m\ddot{x} + \delta'(x, \dot{x}) = ku - F_e - b\dot{x}. \quad (3.9)$$

If furthermore the desired behavior of the system includes damping, the goal dynamics are updated as

$$M\ddot{x} = -F_e + W - B\dot{x} \quad (3.10)$$

with  $B$  as the target damping. The sliding surface under these circumstances is determined in the same manner as the undamped case.

$$s_2 = M\dot{x}(t) + Bx \int_{t_I}^t (F_e(\tau) - W)d\tau - M\dot{x}(t_I) - Bx(t_I). \quad (3.11)$$

The resulting control law is then

$$u_2 = -\frac{1}{k}[r(\eta_2 \text{sign}(s_2) - W) + (r - 1)F_e + (Br - b)\dot{x}]. \quad (3.12)$$

For these control laws the integral must be reset at the beginning of each contact period.

It is interesting to note that including an environmental damping within the external force  $F'_e = F_e + B\dot{x}$ , substituting this into (3.11) in place of  $F_e$ , and shifting all damping terms to the integral identifies the damping as an external force because it returns the impulse-momentum description of the nondamped case with an additional impulsive term. This concept could be used to create virtual contact environments.

### 3.4 Terminal Sliding Mode Control

For the off-contact portion of the cycle a tracking controller is required to follow human hip vertical displacement reference data. Because of the switching occurring

between the two control methods, rapid convergence, preferably with a known finite time, is desirable. Terminal sliding mode control was selected for this task.

The test robot when off-contact, meaning  $F_e = 0$ , can be written in state space form with  $x_1 \triangleq x$  and  $x_2 \triangleq \dot{x}$

$$\begin{aligned}\dot{x}_1 &= x_2 \\ \dot{x}_2 &= -\frac{b}{m}x_2 - \frac{\delta}{m} + \frac{k}{m}u\end{aligned}\tag{3.13}$$

The foundation of terminal sliding mode control for such a system is from [83]. Here it is shown that for a specific form of Lyapunov function stability is attained in finite time. If this result is used to determine the control law to make the sliding function stabilize to zero, convergence by a known time can be enforced for the sliding function. Accordingly, a sliding function that is formed as a differential equation is defined

$$s_1 = \dot{e} + \varphi e + \mu e^\eta\tag{3.14}$$

on  $e = x_1 - x_1^d$ , the tracking error. The constants  $\mu > 0$  and  $\varphi > 0$  are tuning parameters, and  $\eta \in (0, 1)$  affects the convergence time. Note that if  $s_1$  reaches zero, the error will also converge to zero. Greater detail regarding these results can be found in [81, 82, 96].

### 3.5 Switching Laws

Given the two control laws, one for contact and one for off-contact, a method of switching between them is required. A discrete value  $q$  will be used to represent the state of the system with  $q = 0$  equivalent to off-contact and  $q = 1$  for contact. When beginning from off-contact, it seems naturally sufficient to use the force  $F_e$  to engage the contact controller (impulse-momentum sliding mode control).

Transitioning back to off-contact, however, cannot be accomplished based on the

force unless the system bounces off of the environment, causing  $F_e$  to drop. This feature was taken advantage of to provide switching in simulation by implementing a hysteresis region to prevent rapid switching. While bouncing is practically possible for real-time experiments as well because the test robot operates on a treadmill and the belt is elastic with a high stiffness, it is not suitable for the final goal, which is emulating human gait. Accordingly, a dwell-time approach was taken here. Force sensing was used to activate the contact controller. It would remain active until a given period of time had passed at which point the off-contact controller would be engaged. This switching law can be written as

$$q^+ = \begin{cases} 1, & q = 0 \text{ and } F_e \geq F_{th} \text{ and } t_{track} \geq T_D^0 \\ 0, & q = 1 \text{ and } t_{cont} \geq T_D^1, \end{cases} \quad (3.15)$$

where  $F_{th}$  is the force threshold,  $T_D^0$  is the contact dwell time, and  $T_D^1$  is the off-contact dwell time. The variables  $t_{track}$  and  $t_{cont}$  are timers for the off-contact and contact modes, respectively. They are reset after the system exits their associated control modes.

Stability of the switched system under the switching law (3.15) can be inferred based on the separate control systems. The individual controllers have been previously shown to be stable in their active regions. A finite period of activity is enforced by the switching law for the contact controller. Once this time has passed, the control is handed back to the off-contact controller, which provides finite time convergence to a trajectory. As long as the dwell period for tracking is sufficient for convergence, the off-contact controller will lead the system into making contact again, triggering the other controller and setting up a periodic cycle.

Extending beyond the solely vertical trajectory of [96], walking implies that the thigh rotation degree of freedom be reinstated. Under this case it is suggested that the periodic trajectory of the thigh could provide a suitable trigger without the use

of dwell times. A candidate for this is suggested as

$$q^+ = \begin{cases} 1, & F_e > F_{th} \text{ and } q_2 > 0 \\ 0, & \ddot{q}_2^d > \ddot{q}_{2,th}^d \text{ and } q_2 < 0 \\ q, & \text{otherwise,} \end{cases} \quad (3.16)$$

where  $q_2$  is the thigh angle coordinate,  $\ddot{q}_2^d$  is the reference acceleration for the thigh angle, and  $\ddot{q}_{2,th}^d$  is a threshold selected near the maximum magnitude for the thigh angle acceleration when it is extended behind the vertical orientation. Because the hip trajectory follows a trajectory similar to  $-\sin(t)$ , this threshold corresponds to the reversal of the thigh after stance phase.  $q_2 > 0$  implies that the thigh is flexed forward of the vertical orientation. It is noted that the cyclic exchange between controllers under switching law (3.16) is guaranteed by the introduction of the reference data as it maintains a fixed timer, much like the dwell times previously used. However, this condition does not require specification by the operator and automatically matches the periodicity of the gait cycle.

### 3.6 Results and Discussion

According to [96], simulations were run without the use of the dwell-time switching rule. Rather, force alone was used. Then experimental tests were completed using the controller under the dwell time switching law. Building upon [96], preliminary results for the walking case will be described as well. The ground contact and prosthesis models proved insufficient in simulation to represent the actual system while walking. Though periodic motions were attained, the resulting trajectories were unrealistic. Therefore, only experimental results are given for the walking case.

### 3.6.1 Simulations

Reference [71] describes one simulation with damping and one without. These primarily show the effects of a switching law without the dwell time. A mass of  $M = 40$  kg was emulated. The hysteresis bound was set to 1 N with lower bound at 0 N.

Without virtual damping the results show the effects of the leg bouncing off of the simulated treadmill surface. This, however, does allow the system to switch between controllers in a cyclic manner. The tracking controller converges when active ( $q = 0$ ) in just over 0.1 s. The alternating sliding functions  $s_1$  and  $s_2$  effectively converge to zero.

The second case simulated included a virtual damping of 2500 Ns/m. The bouncing was completely eliminated. Rather, the system remained in contact mode for the remainder of the simulation under the force-only switching law. However, this provided proof that the force could be well regulated at just under 400 N ( $Mg = 40 \text{ kg} \times 9.81 \text{ m/s} = 392.4 \text{ N}$ ).

### 3.6.2 Experiments

Several trials were run with the test robot system. The prosthesis described in Chapter II was connected to the hip robot for these tests. The knee was locked for the vertical displacement tests and then operated under the control presented in that chapter for the walking test. The shank force measurements from the strain gauges were used for  $F_e$  for each trial.

Reference [96] reports the vertical displacement test. For these trials the switching law including the dwell time was used. Emulation of  $M = 20$  kg and  $M = 60$  kg was attempted. A damping of  $B = 2500$  Ns/m was used in both cases as it is known that the treadmill belt stiffness is quite high, about 37000 N/m. Tuning of the terminal sliding mode controller was completed by trial and error based on the initial tuning

from the simulation.

For each case the sliding functions neared zero. Accordingly, the force approached the desired virtual weight when in contact, and the terminal sliding mode controller quickly regained trajectory tracking during off-contact mode. Also, the dwell time switching law led to a consistent exchange of controllers.

Validation of the dynamics being emulated by the system was completed offline in [96]. By simulating the system (3.10) with the recorded data for  $F_e$  from the real-time experiments, the trajectories expected from the virtual system were generated and showed good agreement with the measured trajectories. Results in terms of root mean square error for both cases (20 kg and 60 kg) are reported as less than 1 cm/s for velocity and 1 mm for position.

Considering the walking case next, the switching law was updated to depend on thigh trajectories (3.16). The thigh rotation degree of freedom was reactivated and the knee allowed to perform according to its independent control. It should also be noted that both the hip vertical and thigh rotary degrees of freedom were under traditional sliding mode control instead of terminal sliding mode control for this trial due to ease of tuning. Virtual mass  $M = 35$  kg was emulated for this case, and the same damping was maintained.

Several features of the desired control can be identified in Figure 7. First, a cyclic transition between controllers is achieved as indicated by  $q$ . Second, the force, after initial impact, regulates near the desired value. However, the tracking appears very poor. This can be attributed to two sources. The desired trajectory is shifted by a bias term according to the operator's judgement. The bias was not adjusted for this trial in the interest of focusing on the force regulation. Also, though it cannot be determined under the circumstances, the use of traditional sliding mode control could have an effect.

The discrete state  $q$  returns to the contact controller ( $q = 1$ ) too quickly to match



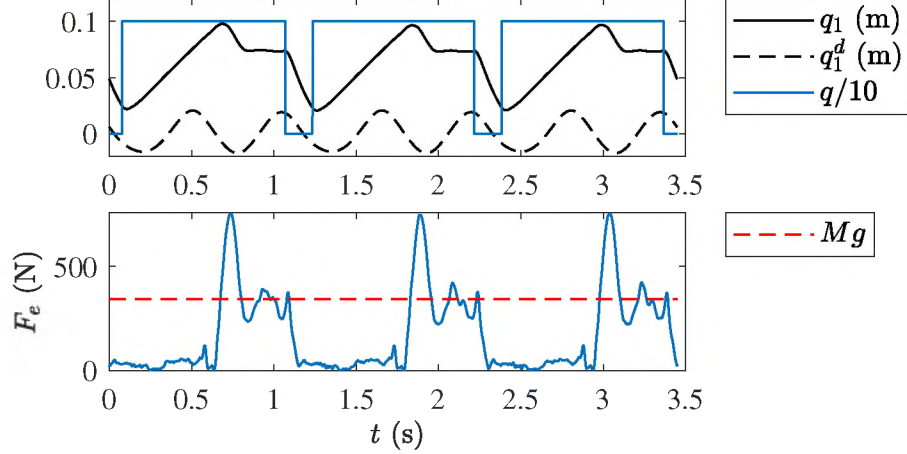


Figure 7: Top: Tracking performance for the vertical degree of freedom for the hip robot.  $q_1^d$  is the desired trajectory, and  $q_1$  is the actual trajectory. The switching state  $q$  scaled by a factor of  $1/10$  is also shown.  $q/10 = 0.1$  indicates that the contact controller is active.  $q/10 = 0$  indicates that the tracking controller is active. Bottom: Shank force measurement  $F_e$  for emulating  $M = 35$  kg

the gait cycle. This is because higher force readings occur when there is no ground contact but the prosthesis is in motion. The switch back to contact mode under these forces is delayed only by the condition on the thigh angle. Significant bouncing is also a notable feature of these results, and is indicated by the positive peak of  $q_1$ . This is likely in part because the prosthetic foot makes initial contact with the heel as opposed to the complete sole. For heel-alone contact the foot is designed to allow a higher displacement of the leaf spring.

Periods during which the force oscillates about the desired value correlate with  $s_2 \approx 0$  as shown in Figure 8. The effects of poor tracking can be identified in the switching function  $s_1$ , which approaches but does not reach zero when the off-contact controller is activated. The control signal spikes with each controller switch. With improved tracking this is anticipated to decrease. Chattering is evident in the control signal when either switching function approaches zero. For the off-contact controller this could be improved by reinstating the terminal sliding mode control.

The prosthesis prototype withstood all mechanical tests, supporting approximately 60 kg in the vertical displacement tests and approximately 35 kg in the walking

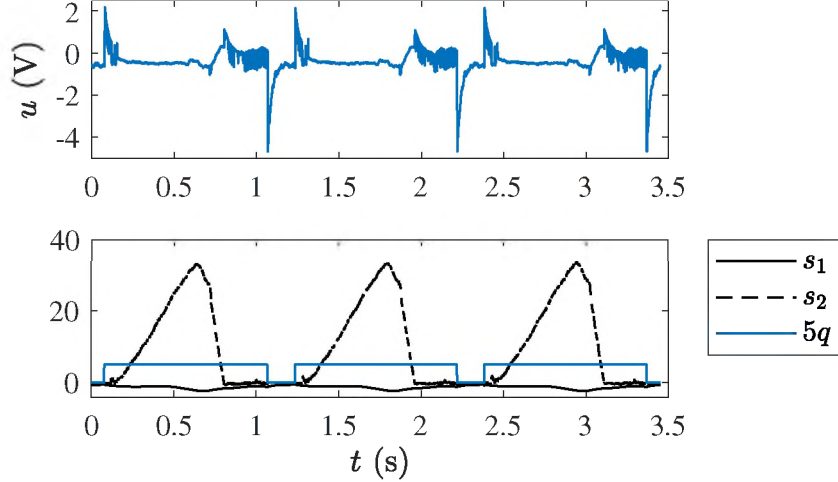


Figure 8: Top: Control input  $u$ . Bottom: Sliding functions for the prosthesis test robot walking trial.  $s_1$  is associated with the off-contact tracking controller.  $s_2$  is associated with the contact controller. The switching state  $q$  scaled by a factor of 5 is also shown.  $5q = 5$  indicates that the contact controller is active.  $5q = 0$  indicates that the tracking controller is active

tests. Due to uncertainty regarding the accuracy of the shank force measurement under these conditions, higher mass values were not tested in an effort to guarantee remaining within the physical limitations of the test robot.

### 3.7 Remarks

The development and results of [96] provided a foundation for controlling the one-legged prosthesis test robot to emulate the weight of a human settling onto the prosthetic leg during walking as opposed to pure-tracking induced contact forces. Reference [96] develops the vertical motion alone. Walking requires adding the thigh rotation and activating the prosthetic knee; it also introduces the dynamics associated with a different region of contact for the prosthetic foot. A switching law to induce walking motion was proposed, and preliminary experimental results under this law were given. Cyclic motion along with contact force regulation were obtained; however, the test results reveal a lack of off-contact tracking and poor switching timing. Even so, the prosthesis maintained steady operation under its independent controller. Due

to the inability of the hip under the current state of the proposed control to emulate more natural walking though, further analysis of the prosthetic gait was not pursued. Shifting the hip reference data and increasing the force threshold are anticipated to provide significant improvements. In addition, terminal sliding mode control should replace the traditional sliding mode control during the off-contact phase, reestablishing the convergence guarantees. These adjustments should improve basic walking gait.

During the walking trial, it was observed that the test robot would occasionally enter a gait cycle involving pure toe or heel walking. Because the control has no means of identifying the difference, the measured shank force is indiscriminate, this pattern would continue for an extended period. If after completion of the previously identified steps to achieve better walking gait these patterns still arise, a method based on the strain gauge data could be developed to return the robot to a normal gait cycle. For example, the raw strain gauge measurements could be recalibrated to provide some information about the moments seen by the foot.

Lastly, it is proposed that the test robot can emulate walking on various surfaces, creating a virtual environment like sand. The impulse-momentum sliding mode control method does not require that the damping remain linear. Rather, a nonlinear model is possible. The control law could be extended for use with a model such as is derived in [18]. The limitations of this concept should be explored, and completion of such a study would significantly extend the capabilities of the hip robot and provide valuable insight into the response of prosthetic legs under various environments.

## CHAPTER IV

### WALKING TRIALS WITH THE POWERED TRANSFEMORAL PROSTHESIS

#### 4.1 Introduction

Two forms of human testing were completed with the prosthesis developed in Chapter II. The first was by an able-bodied individual by use of a bent-knee or bypass adapter. These tests were to confirm that individual features of the control law responded as expected. They were also used to find an initial tuning for the gains, primarily to identify their orders of magnitude. Following this early investigation, trials with a volunteer with a transfemoral amputation were conducted at the Louis Stokes Cleveland VA Medical Center. The experimental methods used during this study are described first. Gait analysis is then performed and followed by analysis of the prosthesis' internal sensor data. Results show the feasibility of the control method and prototype design. Basic walking gait is attained alongside self-powering operation.

#### 4.2 Experimental Procedure for Human Trials

The test protocol was approved by the Louis Stokes Cleveland VA Medical Center's institutional research board. Three constant walking speeds were tested, and

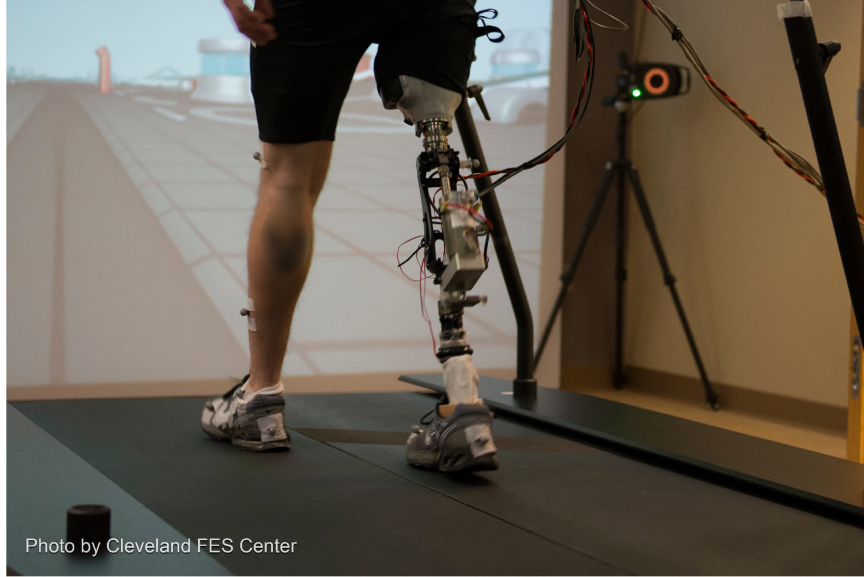


Figure 9: Volunteer test subject wearing the prosthesis prototype © 2018 ASME [59]

one trial starting from standing, reaching the maximum speed comfortable to the test subject, and returning to standing was conducted. The three constant speeds were chosen as the test subject's preferred speed while walking with his daily prosthesis (0.75 m/s) and 0.15 m/s above and below that rate. With exception of the variable speed trial, the same data was collected using both the test subject's daily-use prosthesis and the prototype prosthesis. However, the prostheses were tested on separate days.

Figure 9 shows the 35-year-old male test subject (175.3 cm, 81.7 kg) with a transfemoral amputation of the right leg wearing the prosthesis. The volunteer for this study daily uses a Plié knee from Freedom Innovations and, as previously mentioned, an Ottobock Triton Vertical Shock foot. The Plié knee falls into the category of a microprocessor-controlled passive knee. For each test condition the subject's daily foot and socket were used to conduct the tests. Adjustments were made by a certified prosthetist to fit and align each piece.

For at least fifteen minutes on two days prior to the data recording session the subject used the experimental knee to orient himself to its operation. During these

Parameter	Value
$b_h$ (Ns/mm)	2.5
$q_{threshold}$ (mm)	2
$K$ (N/mm)	200
$K_s$ (N/mm)	0
$q_4^o$ (mm)	0
$B$ (Ns/mm)	-1.743

Table II: Prosthesis control gains

trial sessions, controller tuning was completed starting from the gains established during bent-knee adapter testing and adjusting according to the test subject and prosthetist’s feedback. The final gain set as used for all trials is listed in Table II.

A 10-camera passive marker motion capture system with a 100 Hz sample rate (Vicon, Oxford Metrics, UK) recorded 26 markers placed on standard anatomical locations according to the Human Body Model (Motek Medical, Amsterdam, NL). The force plates of the split belt treadmill measured ground reaction forces for each side (Motekforce Link, Amsterdam, Netherlands). All gait data was post-processed with a second-order zero-lag Butterworth filter with a 6 Hz cutoff frequency [132].

### 4.3 Gait Data Analysis and Results

Inverse dynamics were computed in the sagittal plane for the leg segment on the amputation side according to the method of [145] from the marker and forceplate data. The data were time-normalized to percent gait cycle. Ensemble averaged profiles for hip, knee, and ankle angle, moment, and power across ten gait cycles for each speed tested and both prostheses are shown in Figure 10, which also includes a set of able-bodied data from [105] for comparison.

Gait with both the experimental and daily prostheses resulted in similar hip and knee angles for all speeds. These profiles also approximated the able-bodied data. In particular, one can see increased knee flexion angle amplitude with increasing gait speed [61]. Another feature of able-bodied knee kinematics, stance flexion [105,

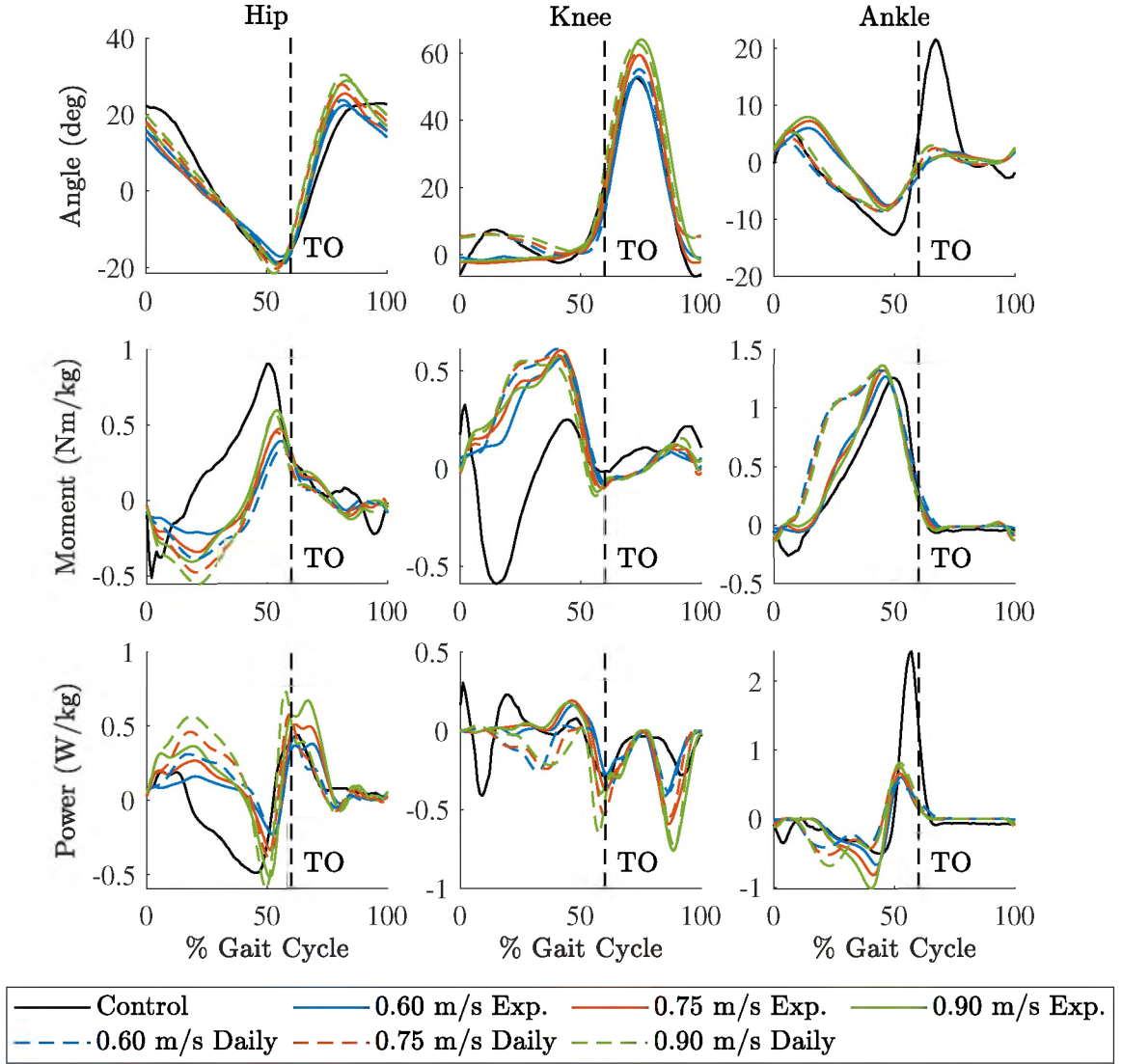


Figure 10: Kinematic and kinetic data for the hip, knee and ankle joints of an able-bodied control subject (black), a volunteer with an amputation wearing the experimental prosthesis (solid), and the same individual wearing his daily prosthesis (dashed) normalized over time. Data for the volunteer with an amputation represent an average of ten gait cycles each at 0.60 m/s (blue), 0.75 m/s (red), and 0.90 m/s (green). Control data is at 1.11 m/s and replicated from [105] (Public Domain). The gait cycle begins with foot strike. Toe off is marked by a black dashed line and denoted by TO. Positive angles and moments correspond to hip and knee flexion and ankle plantarflexion. Positive joint power indicates power production, and negative joint power is associated with power absorption

143, 145], does not appear in Figure 10. This is typically associated with the knee absorbing some of the impact of ground contact and is inconsistent across passive and active knee prostheses for walking [47, 50, 105, 109, 118, 120]. Three possible explanations for this behavior include lack of trust in the knee prosthesis, effects of the prosthetic ankle, and gait habits built up by use of a passive prosthesis. Even though the proposed controller would provide support, lack of experience with the knee lends a measure of caution as knee buckling is a dangerous situation, particularly when one’s prosthesis is seen as unpredictable. The second possibility, the prosthetic ankle is the source, stems from data where individuals with transtibial amputations, those who require a prosthetic ankle alone and possess a natural knee joint, also do not walk with stance flexion [104]. Lastly, most passive prostheses naturally collapse at a slow rate when flexed. To straighten the knee requires the effort of the healthy side. It follows that stance flexion is simply a waste of energy when walking with a passive prosthesis, leading to habitual gait patterns avoiding it. Regardless of the cause or combined causes, the controller of the experimental prosthesis theoretically supports stance knee flexion, and it would likely require training and more experience with the prosthesis for the volunteer to consistently demonstrate it. For example, reference [121] has shown stance flexion for one subject using a powered prosthesis; whether this is due to intensive control tuning or his experience is unclear. The top-right plot of Figure 10 shows that the ankle kinematics are consistent with prosthetic gait. Because it is a passive spring, it is missing the major plantarflexion action during early swing; rather, it returns to equilibrium.

Analyzing the joint kinetics, one can see that the hip moments significantly differ from the able-bodied case but are similar in shape between both prostheses. The negative moment during stance phase might indicate an attempt to keep the knee locked for this period, preventing the aforementioned knee stance flexion. The prostheses also behave similar to one another at the knee joint. While there is actually a



flexion moment at the knee, it appears to be overcome by the hip action, yielding no kinematic response. In addition, this flexion moment clearly opposes the extension moment that should occur during this period; it is likely due to the mechanical hinge limit preventing overextension of either prosthesis. This behavior is consistent with other passive prosthesis walking gait data [105] and precludes the impact absorption provided by stance flexion. Achieving stance flexion with the experimental prosthesis by the methods previously described is expected to correct the sign of the knee moment in this segment of the walking gait cycle. The ankle moment is closer to the control data for the experimental prosthesis than the daily prosthesis. These comparisons are made lightly, however, as Winter concludes that the gait kinetics used to generate what is considered standard kinematics show high variability [144].

Power at the hip indicates significant usage for both prostheses during stance phase; as previously indicated from evaluating the hip moment, this is likely for stabilization. Two features of the knee power curve validate its design and response. First, the lack of positive or negative power for 40% of the gait cycle indicates that the prosthesis is conserving power while in the self-locking position. Second, there is a positive power period beginning at 40%, indicating that the motor is providing power to the system. Positive power is distinctly lacking from the daily prosthesis profiles. Both prostheses show the latter two negative power segments associated with swing phase [143]. Differentiating the prostheses by design though, the experimental prosthesis can store this power while the daily prosthesis releases it as heat. Lastly, evaluating the ankle profile, it is consistent with the power absorption and release that would be expected from a spring type element. Neither case, the experimental or daily prosthesis, provide sufficient positive power for push off, highlighting the importance of future development of an integrated powered ankle solution.

Taking the leg subsystem beginning from the hip interface as an independent system, the work associated with the hip interaction forces and each joint torque can

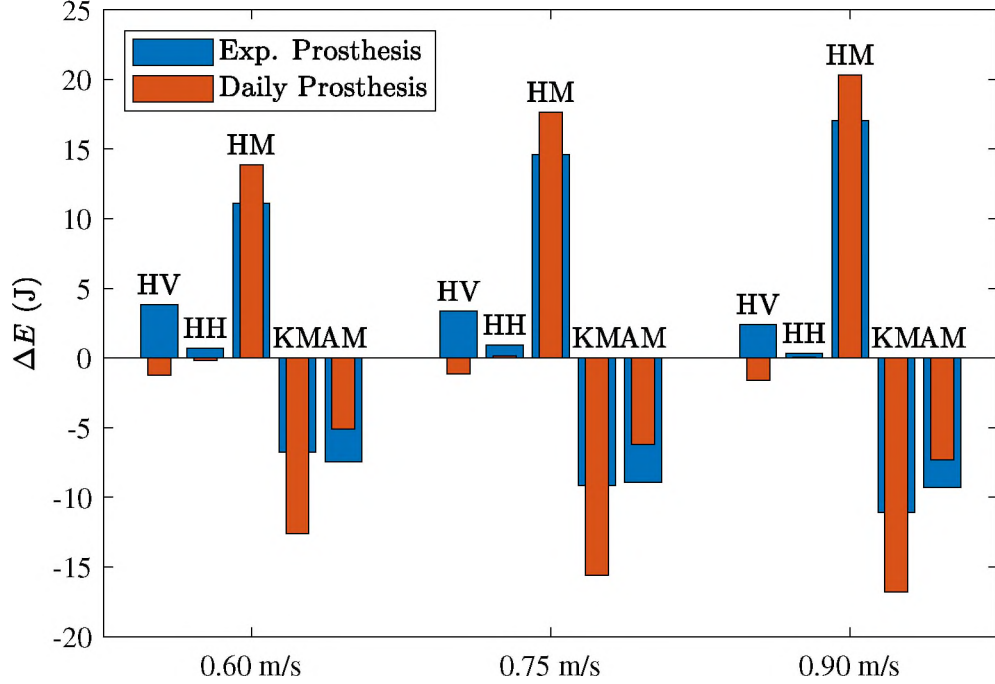


Figure 11: Average change in energies across ten gait cycles for the leg subsystem beginning at the trunk/hip intersection. Terms represented include work done by hip vertical force (HV), hip horizontal force (HH), hip joint moment (HM), knee joint moment (KM), and ankle joint moment (AM) for both the experimental prosthesis and the daily prosthesis. A positive change in energy represents energy added to the leg subsystem

provide insight into the volunteer's energy requirements while walking with either prosthesis [133]. All resulting energy terms are shown for each speed in Fig. 11. The only power sources for this system are the forces and moment between the hip and trunk and the forces associated with ground contact at the foot. Under the rigid body assumption, the ground reaction forces do no work and are, therefore, excluded from the analysis.

The work done by the hip vertical force (HV) during the volunteer's use of the experimental prosthesis results in energy being added to the leg subsystem whereas HV represents a loss of energy from the leg subsystem when the test subject uses his daily prosthesis. The expenditure associated with the experimental prosthesis, however, decreases with increased speed. The horizontal components of the work done by the hip interaction force (HH) are far less patterned according to speed but

do consistently require a small energy input by the volunteer for all speeds with the experimental prosthesis. Completing the analysis of the hip, the work of the hip joint moment (HM) requires less energy from the leg subsystem for the experimental prosthesis than the daily prosthesis, and both prostheses require more energy with increasing speed. A rough sum of the terms associated with the hip suggests that there is a slight increase in energy required at the hip from the test subject when using the experimental prosthesis rather than the daily prosthesis.

The knee joint moment work (KM) of the experimental prosthesis incurs less energy loss from the leg subsystem than the daily prosthesis, and, notably, some of this loss can be stored by the regenerative drive in the experimental prosthesis. The opposite situation holds for the work of the ankle moment (AM); the experimental prosthesis extracts more energy from the leg subsystem than the daily prosthesis, indicating that the volunteer’s changes in gait with the experimental prosthesis might be less efficient for the ankle. It is noted that this type of analysis is susceptible to inaccuracies in marker placement, shifting of joint centers of rotation, soft tissue displacement, and cross-joint energy transfer by the hip muscles that are not captured by this method. However, the relative trends established should be less sensitive to these sources of error [133, 152].

Video of the trial completed at 0.9 m/s is available in [137].

#### **4.4 Prosthesis Sensor Data Analysis and Results**

The data collected from the prosthesis’ sensor suite can provide additional insight into the operation of the system and further substantiates the observations made from the gait data. Considering the control signal in Figures 12 to 14, one can see that there is slight activation of the controller to straighten the knee during stance phase particularly for the two non-preferred speeds. While it is currently anecdotal evidence, perhaps habitual gait with the test subject’s passive prosthesis is more prevalent at

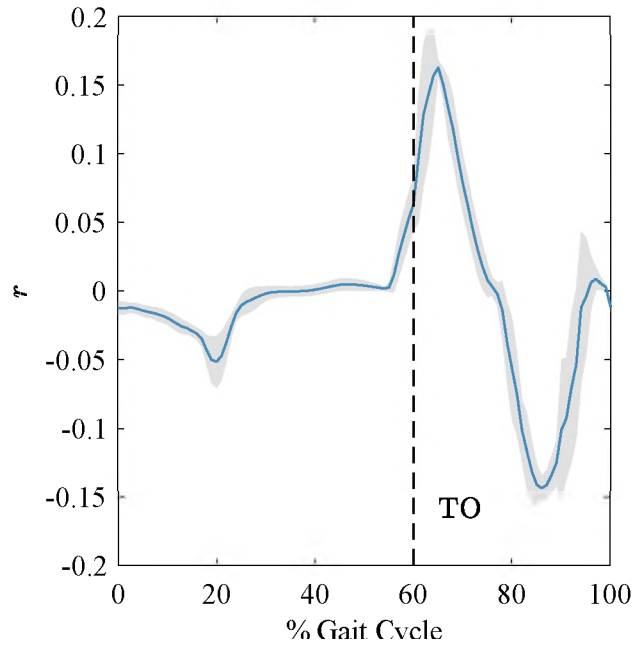


Figure 12: Average control signal  $r$  and one standard deviation for walking at 0.6 m/s. The gait cycle begins with foot strike. Toe off is marked by a black dashed line and denoted by TO

the preferred speed, where there is significantly less evidence of the potential for stance flexion. Further evaluating the generated controls, they maintain magnitudes well within the range for  $r$ , leaving the possibility of more demanding tasks such as sit to stand or stair climbing.

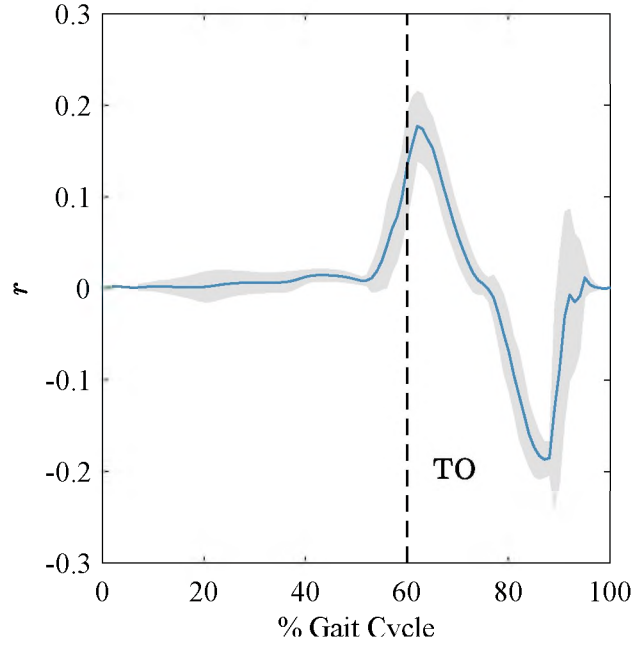


Figure 13: Average control signal  $r$  and one standard deviation for walking at 0.75 m/s. The gait cycle begins with foot strike. Toe off is marked by a black dashed line and denoted by TO

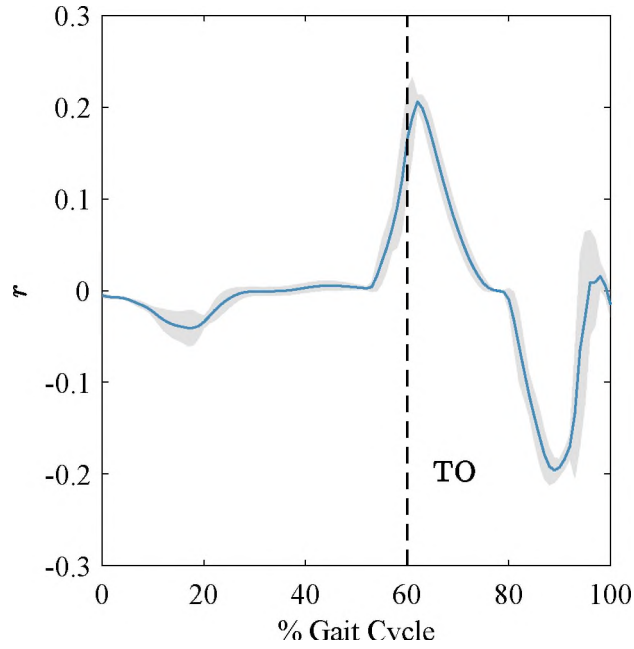


Figure 14: Average control signal  $r$  and one standard deviation for walking at 0.9 m/s. The gait cycle begins with foot strike. Toe off is marked by a black dashed line and denoted by TO

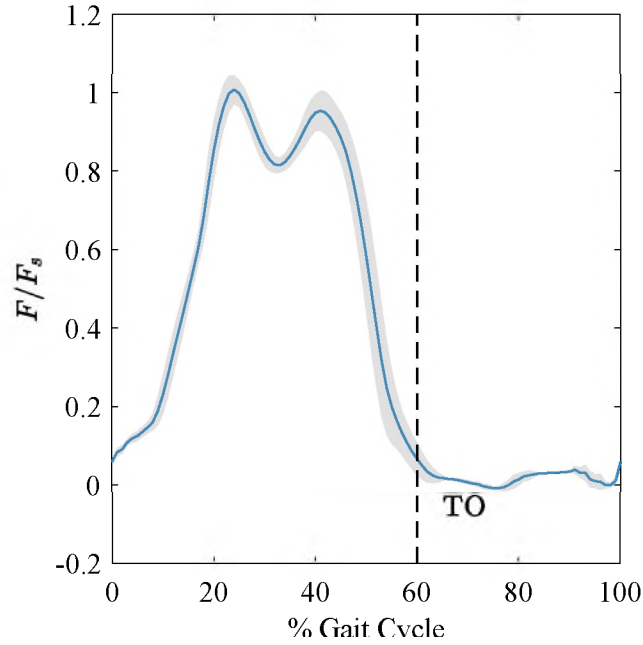


Figure 15: Average normalized shank force measurement and one standard deviation for walking at 0.75 m/s. The gait cycle begins with foot strike. Toe off is marked by a black dashed line and denoted by TO

Validating the measurement used to generate the control, a representative curve for the normalized shank force is given in Figure 15. Here it is observed that the normalization factor was effectively measured and maintained relevance; the limited standard deviation band suggests that for the time period across which a given test was completed strain gauge drift, a common issue with these sensors, was not significant. It is also noted that the force takes on the familiar double-peaked shape of vertical ground reaction force as measured in most gait studies by highly accurate force plates [9].

An internal energy balance of the experimental knee reveals the efficiency of the regenerative actuator; see Figures 16 to 18. The input is the knee moment work, computed from the gait data. The difference between this and the change in energy at the electrical port of the motor approximates the amount lost due to friction or being stored as potential or kinetic energy. To determine the electrical losses,

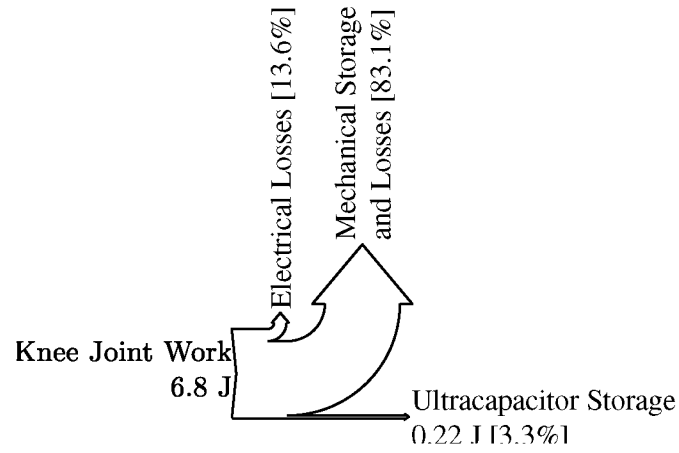


Figure 16: Sankey diagram of the internal energy balance for the experimental prosthesis walking at 0.60 m/s.

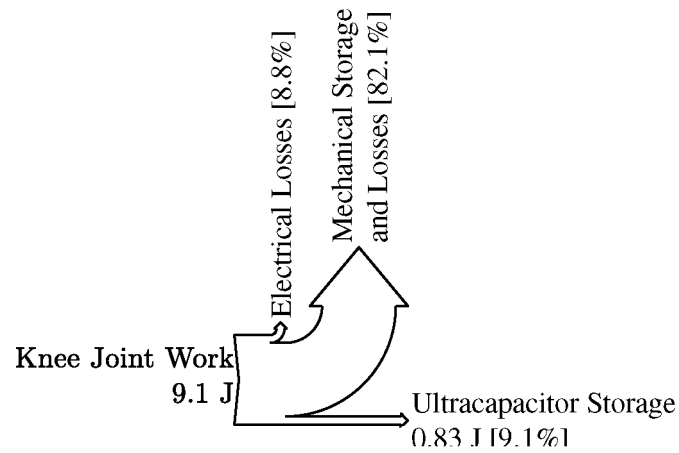


Figure 17: Sankey diagram of the internal energy balance for the experimental prosthesis walking at 0.75 m/s.

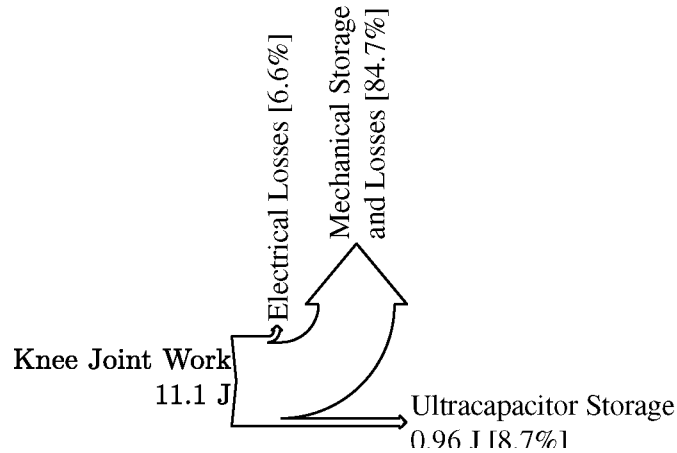


Figure 18: Sankey diagram of the internal energy balance for the experimental prosthesis walking at 0.90 m/s.

neglecting inductance, the difference between the energy entering the capacitor and that available at the electrical port of the motor is evaluated. What remains passes into the capacitors.

The majority of the energy is lost to or remains in mechanical forms. This is consistent with expectations for the system components; for example, an ACME lead screw is used in the transmission and has a reported efficiency of 65%. Electrical losses decrease with increasing speed. The more notable improvement in electrical efficiency occurs between the slow and preferred speeds, suggesting that the motor driver has an optimal minimum voltage and/or current for efficiency and improved efficiency might be attainable for these circumstances with a different driver. The electrical losses can also be partially attributed to a constant power usage of 0.7 W by the motor driver and the Joule losses of the motor armature and tether. At all speeds the capacitor storage bank saw an increase in energy. While this energy is certainly coming from the test subject, it need not be a concern if it stays within the parameters suggested by able-bodied measurements. To truly evaluate this would require metabolic cost measurements, which were not able to be taken during this trial but would be a helpful metric in the future. If the capacitors become discharged,



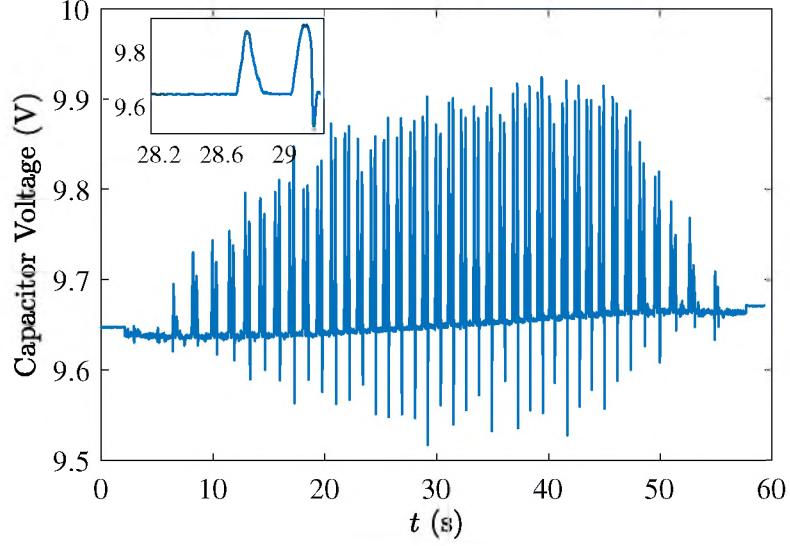


Figure 19: Net increase in capacitor bank voltage during variable speed trial where the volunteer began from and returned to a standing state, reaching a maximum gait speed of 1.35 m/s. Inset shows one representative gait cycle

a battery backup is a likely solution.

Examining the freely variable gait speed test shows that the volunteer chose to walk at up to a maximum speed of 1.35 m/s. No control gains were adjusted to complete this trial, and across a one minute period the test subject transitioned from standing to the peak speed and returned to standing. Furthermore, increasing depth of knee flexion when increasing speed was consistent with able-bodied gait [61], exhibiting the flexibility of the controller. The length of the trial also allows observation of the prosthesis' regeneration capacity. Figure 19 shows that the capacitor bank voltage increased by 0.023 V. It is noted that the voltage drops under load and recovers when the load is removed, which is indicative of the supercapacitor bank's internal resistance. Looking at the inset of a representative gait cycle, there are two positive voltage peaks correlating with the negative power peaks seen at all gait speeds in Figure 10. The voltage drop near the end of the cycle corresponds with activation of the hard stop prevention damping at the end of swing phase.

## 4.5 Test Subject Feedback

Upon concluding all trials, the volunteer provided his thoughts on the experimental prosthesis. He expressed concern about the weight of the device. Indeed, the combined weight of the experimental prosthesis and the foot is 4.23 kg as opposed to 2.21 kg for his daily prosthesis and the foot. The experimental prosthesis likely requires refining to account for the weight associated with the residual limb, socket, and embedding the electronics; however, it is a worthy consideration that anthropometry suggests a weight of up to 4.98 kg for this individual's leg [145]. Additional feedback indicated that he felt the most benefit from the powered prosthesis at faster walking paces.

## 4.6 Remarks

Experimental tests with an individual with a transfemoral amputation have shown the feasibility of a prosthesis prototype that implements a novel control method and energy regeneration. Varying impedance in a continuous fashion dependent on shank force sensing without having to use gain switching makes the control tuning simple and the prosthesis response predictable. This approach also allows for variable gait speeds without introducing further gain scheduling. With five parameters that can be easily related to the gait cycle, tuning is intuitive. The last parameter can be identified analytically to achieve energy regeneration by the method developed in this work. The associated use of negative damping to achieve energy regeneration is also unique. Indeed, this is the first known application of purposeful electrical energy regeneration in a active prosthetic knee that shows self-powered operation in a human trial.

Future study should pursue three directions. First, an active ankle should be designed and integrated into the prosthesis. As a net positive power source to the

gait cycle, an active ankle should improve walking gait. Secondly, efforts should be made to achieve more natural gait kinematics and kinetics with the combined system. Progress in this area should be supported by the implementation of an active ankle but might also include user training to re-integrate previously avoided gait features such as stance flexion. Third, a broader task set needs to be evaluated. For example, the proposed control method could conceivably handle foot-over-foot stair ascent. It can provide support when the intact side is leading, and when the prosthetic side is leading, as the individual increases the force through the shank, the knee will extend. Assuming the individual using the prosthesis has the capacity to support the hip, the action of knee extension will lift the him or her to the next step.

In addition to these broader considerations, the prototype could benefit from extensive design optimization for efficiency. The mechanical system can easily be improved by a ball screw (90-95% efficient). Embedding the electronics and supercapacitors would decrease Joule losses by removing the tether. A more efficient motor and driver would also help; particularly while choosing the motor, guidance can be derived from observing that regeneration is related to the motor torque constant and armature resistance. Truly, if the prosthesis can capture most of the available knee power during gait, it should approach the capacity to power an active ankle [143]. Lastly, to consider longer operation periods, the prosthesis will require a comprehensive power management system to handle both the possibility of overcharging and of extended net positive power usage leading to uncontrollability when discharged.

PART 2:

MUSCULOSKELETAL MODELING FOR  
HUMAN-MACHINE INTERACTION SIMULATION

## CHAPTER V

### BACKSTEPPING CONTROL OF A MUSCLE-ACTUATED LINKAGE HUMAN SIMULATION

#### 5.1 Introduction

With the advancement of computing power, the practice of performing extensive simulation prior to prototyping continues to gain momentum. However, limited literature addresses the case where a human interacting with a robotic system must be simulated. A foremost example is prosthetic leg design, which typically moves directly from mechanical and control design, perhaps considering simulation of the robotic system in isolation, to human-involved physical prototype tests. Similarly, the design of advanced exercise machines and related control algorithms generally proceeds to human trials without simulating the machine and human together. To address this limitation of the human-machine interaction design pipeline, a closed loop simulation of a human represented by an open chain robotic linkage where the system actuators are dynamic muscle models is proposed.

Hill-type muscles have been selected to provide actuation to the system. More advanced muscle models exist, including one based on partial differential equations [46] and another based on finite elements [150], but the accuracy of the generated force

rather than internal dynamics are being considered here. Accordingly, the Hill muscle model is sufficient because it highlights the natural components of the human muscle and is considered both accurate and computationally feasible for simulation [146,151].

Although human models actuated by muscles have previously appeared in the literature, their goals vary from this work and can be classified broadly by two categories, system identification and inverse dynamics. For system identification studies such as [2] the simulation is generally open-loop and formulated as an optimal control problem. Their primary goal is predictive—to seek to identify some feature(s) of the control system of the human. In the second case for which [17, 31, 132] are representative studies, human data is input to a model, and the dynamic response is the output. This data is helpful for medical assessment or for validating the results of the first category of studies [148]. In contrast, the proposed human simulation is closed-loop such that it can track internally produced trajectories and interact with the environment.

Model predictive control (MPC) has been used to close the loop around the previously mentioned optimal control methods. By applying MPC, a cost function associated with standard human motion goals, such as minimizing muscle activations or joint torques, is implemented. Several studies specific to gait employ MPC [53, 91, 116, 117, 129, 147]. However, these works neglect the effects of muscle dynamics, and for examining human-machine interaction, the muscles are fundamental. For instance, applying such a simulation to advanced exercise machine design requires muscle data to evaluate the effectiveness of the machine in general. Moreover, one study where extremum-seeking control was applied to an exercise machine to optimize muscle effort required direct feedback from the muscles [90]. Additionally, recent work has identified the need to simulate musculoskeletal and prosthesis models interacting [31]. In contrast, Mehrabi and colleagues do include muscle dynamics in [79], but they eliminate the muscle tendon states because they limit their

development to an arm model. In contrast, the proposed work will be established for general muscle-actuated linkage models, including all elements of the Hill muscle.

When considering the human controller, the following features can be identified from observing the resulting actions of the human system:

1. Capable of nearly exact tracking if required (Tracking control)
2. Capable of skillful environmental interaction when loads are within capacity (Impedance control)
3. Capable of changing reference mid-activity (Feedback, Toleration of uncertainty)

The control method developed for the muscle-actuated linkage should capture these features. However, it should also be useably convenient as it is intended to be a tool in the assistive roboticist's toolbox.

Hill muscle model-based controllers have been developed for purposes other than modeling the human. Examples are scattered throughout the literature for applications such as exoskeleton and prosthesis controllers [11, 22, 30]. The research performed in the area of functional electrical stimulation (FES) also unites the concepts of muscle actuation and control. Control methods such as active disturbance rejection, reinforcement-learning, adaptive, predictor-based and PD control have been used for FES [48, 51, 52, 64, 128, 149]. In these cases the structure and data contained within the Hill muscle is used to inform model-based control laws. In contrast to the proposed simulation, the human is seen as external to the system in these papers, and the FES controllers do not account for environmental interaction.

Backstepping control was chosen for the human simulation because it offers the framework to apply various controllers, for example a joint-level controller, through the muscle actuators. It, in effect, allows any control method that has a known Lyapunov function to be used for the human while providing analytical stability guaran-

tees [60]. Conceptually then, backstepping can be consistent with the three identified features of human control and the self-evident idea that humans do not mentally consider the details of what needs to happen at the muscle level to accomplish a chosen task. Seeking these same benefits, [63] uses backstepping for an FES application where it is assumed that the muscles will not co-contract. However, in the natural system, it is by the co-contraction mechanism that humans can vary the impedance of joints for a selected pose [40]; this is associated with the second feature previously identified as desirable for the human system when interacting with the environment. Accordingly, the backstepping control framework developed in this work will avoid the limitation of having only one active muscle at each joint, leaving the opportunity for co-contraction available.

Section 5.2 proceeds by presenting background information on the Hill muscle model. A simulation developed to study the constitutive dynamics of an antagonistic muscle pair is discussed next and is used to introduce backstepping control. This is followed by the development of the muscle actuated linkage framework under backstepping control. Within this context two methods for addressing muscle redundancy are introduced. Performance is then evaluated for a human arm simulation example, resulting in good tracking and indicating the importance of constraint protection within the control method. This chapter concludes by addressing future considerations and motivating the next chapter.

## **5.2 Hill Muscle Model as Actuator**

As an alternative to gearmotors, hydraulic pistons, or other typical actuators, a model of the human muscle can provide a means of actuation within simulation.

### **5.2.1 Hill Muscle Model**

Consider the Hill muscle model as depicted in Figure 20. An individual Hill mus-



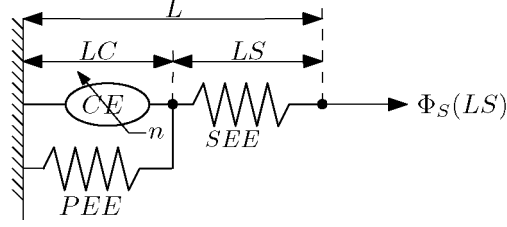


Figure 20: Hill muscle model with series elastic element ( $SEE$ ), parallel elastic element ( $PEE$ ), contractile element ( $CE$ ), and control input  $n$ . The resulting tendon force is denoted  $\Phi_S(LS)$

cle includes several elements. First, a series elastic element ( $SEE$ ) is modeled by a nonlinear spring with a slack region; it embodies the effects of the human tendon. Next, a contractile element ( $CE$ ) represents the muscle body; it is the active force generating element. Finally, the parallel elastic element ( $PEE$ ) represents the nonlinear stiffness of the muscle body that becomes effective once the muscle has been drawn beyond its optimal length. The control input to the system is denoted by  $n$ , the neural input.

According to the geometry of the muscle system shown in Figure 20, each muscle, uniquely identified by index  $j$ , has state  $LS_j$  with dynamics

$$\dot{LS}_j = \dot{L}_j - \dot{LC}_j. \quad (5.1)$$

Figure 20 also supports a force summation for the contractile element  $F_{CE,j}$

$$F_{CE,j} = \Phi_{S,j}(LS_j) - \Phi_{P,j}(LC_j), \quad (5.2)$$

where the  $\Phi_{S,j}$  and  $\Phi_{P,j}$  functions are the force of the  $SEE_j$  and  $PEE_j$ , respectively. Both force functions are composed of a slack region followed by a monotonically increasing function. The slack for  $\Phi_{S,j}$  represents a slack tendon and implies that the total output force of the muscle remains zero. Similarly,  $\Phi_{P,j}$  produces zero force until the muscle is stretched past its optimal length  $L_{o,j}$ .

Composed of a phenomenological model, the contractile element produces force according to

$$F_{CE,j} = a_j f_j(LC_j) g_j(-\dot{LC}_j) F_{max,j}, \quad (5.3)$$

where the first three terms scale the maximum isometric (constant length) force  $F_{max,j}$ . Scaling term  $a_j$  ranges between zero and one and is related to the neural input  $n_j$  by first order lag dynamics, identifying  $a_j$  as the second state associated with each muscle. Details of these dynamics will be discussed in later sections. The second scaling term is the function  $f_j$ , which can be described as the force-length relationship. It is defined by a Gaussian shaped curve with a maximum value of one at the optimal contractile element length  $L_{o,j}$ . Third, the scaling function  $g_j$  adds the effects of the muscle contraction velocity on the force generation capacity. It is described piecewise by the Katz and Hill curves

$$g_j(-\dot{LC}_j) = \begin{cases} \frac{AV_{max,j}(1-g_{max})-g_{max}(A+1)\dot{LC}_j}{AV_{max,j}(1-g_{max})-(A+1)\dot{LC}_j}, & \dot{LC}_j > 0 \\ \frac{AV_{max,j}+A\dot{LC}_j}{AV_{max,j}-\dot{LC}_j}, & \dot{LC}_j \leq 0, \end{cases} \quad (5.4)$$

where  $A$  is the Hill constant,  $V_{max,j}$  is the maximum contraction velocity, and  $g_{max}$  is the eccentric contraction limit. The range of the  $g_j$  function is between  $-A$  and  $g_{max}$  [37, 54].

Equating (5.2) and (5.3) gives a constraining equation for  $\dot{LC}_j$

$$\dot{LC}_j = -g_j^{-1}(z_j), \quad (5.5)$$

where

$$z_j = \frac{\Phi_{S,j}(LS_j) - \Phi_{P,j}(LC_j)}{a_j f_j(LC_j) F_{max,j}}, \quad (5.6)$$

completing the Hill muscle model.

### 5.2.2 Equilibrium Properties

Understanding the equilibrium properties of the muscle dynamics is foundational to constructing the desired simulations. To evaluate equilibrium, assume a constant muscle length,  $\dot{L}_j = 0$ ; this implies that any system being actuated by the muscle subsystem is also at equilibrium. Setting the state derivative of  $LS_j$  to zero gives

$$\dot{LS}_j = 0 = \dot{L}_j + \dot{LC}_j \implies \dot{LC}_j = 0. \quad (5.7)$$

Following this condition through (5.5) and (5.6) leads to  $z_j = 1$  and consequently

$$\Phi_{S,j}(\overline{LS_j}) - \Phi_{P,j}(\overline{LC_j}) = \overline{a_j} f_j(\overline{LC_j}) F_{max,j}, \quad (5.8)$$

which simply indicates that the difference in force between the  $SEE_j$  and  $PEE_j$  must be equivalent to the force generated in the  $CE_j$  under equilibrium conditions, as denoted by the overbars.

The second state associated with each muscle is the activation. Its state derivative is also set equal to zero for equilibrium. Considering that the dynamics of this state are in the form of a first-order lag with the input  $n_j$ , it is evident that equilibrium requires  $\overline{a_j} = \overline{n_j}$ .

Briefly considering the Hill muscle model's stability at a constant length provides insight into the muscle's general behavior. Note that  $\dot{L}_j = 0$  does not imply  $\dot{LS}_j = \dot{LC}_j = 0$ . A brief simulation study of this feature of the muscle dynamics showed invariance to differing initial combinations of  $LS_j$  and  $LC_j$  for a fixed muscle length  $L_j$ . For initial conditions consistent with the muscle dynamics, the dividing point in the constant length  $L_j$  between  $LS_j$  and  $LC_j$  would converge to a combination of  $LS_j$  and  $LC_j$  such that  $z = 1$ .

### 5.2.3 Model Normalization

Because some preliminary studies completed within this work do not directly correlate with any human joint, a normalized model was used, thereby studying the muscle in general without having to assign properties of, for example, the Biceps Brachii and so limiting the results to that case. According to [151], each muscle length parameter can be normalized by  $L_o$ , each velocity term by  $V_{max}$ , and each force by  $F_{max}$ . These three parameters can be specified uniquely for each muscle. For the normalized studies of this work, however, the same parameter values were maintained across muscles. Under these circumstances a normalized time can be determined as

$$\tau \triangleq \frac{t}{\tau_c} \text{ with } \tau_c = \frac{L_o}{V_{max}}. \quad (5.9)$$

With this information the normalization can be extended to non-muscle subsystems. For example, a mass being positioned by a muscle actuator combines these two system types. To normalize a general state equation requires chain-rule expansion in terms of  $\tau$ . Returning to the single muscle actuated mass example and denoting normalized variables with a superscript  $n$ , normalization of a linear velocity  $\dot{x}$  in terms of the muscle parameters and normalized time under the assumption that position  $x^n \triangleq \frac{x}{L_o}$  gives

$$\frac{dx^n}{d\tau} = \frac{dx^n}{dt} \frac{dt}{d\tau} = \frac{dx^n}{dt} \tau_c = \left( \frac{1}{L_o} \frac{dx}{dt} \right) \tau_c = \left( \frac{1}{L_o} \frac{dx}{dt} \right) \frac{L_o}{V_{max}} = \frac{1}{V_{max}} \frac{dx}{dt}, \quad (5.10)$$

where the non-normalized state equation  $\frac{dx}{dt}$  must now be substituted. This simple case leads back to the previous statement that velocities can be normalized by division by  $V_{max}$ . Evaluation of more complex cases can be completed in a similar manner.

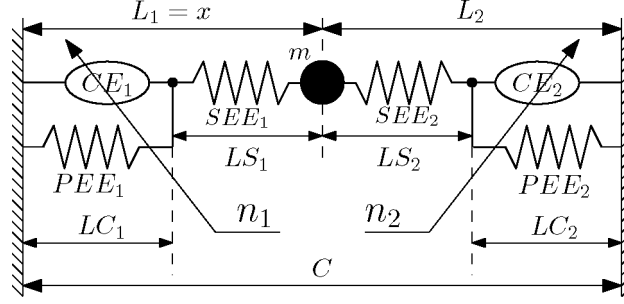


Figure 21: Mass system actuated by an antagonistic pair of muscles that are each anchored to a wall. The walls are distance  $C$  apart

### 5.3 Antagonistic Muscle Pair Actuated Mass

To develop a means of understanding the fundamental dynamics of an antagonistic muscle pair, a simple simulation consisting of a mass between two opposing muscles that were each attached to a wall was developed. Trajectory tracking for the mass is desired. The system construction implies that the force applied to the mass is the net consequence of both muscles; they are redundant actuators. This system has been developed in two stages, without and with the activation dynamics. For details of the simpler case, without activation dynamics, the reader is referred to [101]. Much of the work to be presented here has been published in [139].

#### 5.3.1 Muscle Actuated Mass Model

Figure 21 illustrates the two muscle actuated mass system. In addition to the Hill muscle model as previously described, several further notations have been added. The length of muscle one is selected as the state  $x$ , locating the mass. Also, the system is of constant overall length  $C$ .

Defining  $x_1 \triangleq x$ , the state equations for the two muscle system after normalization

are

$$\dot{x}_1 = x_2 \quad (5.11)$$

$$\dot{x}_2 = \frac{1}{m} (\Phi_{S2}(LS_2) - \Phi_{S1}(LS_1)) \quad (5.12)$$

$$\dot{LS}_1 = x_2 - \dot{LC}_1 \quad (5.13)$$

$$\dot{LS}_2 = -x_2 - \dot{LC}_2, \quad (5.14)$$

recalling that  $\dot{LC}_j$  is not a state but is defined by combining (5.5) and (5.6).

The addition of the aforementioned activation dynamics completes the system model. From [151]

$$\dot{a}_j = -\frac{\beta_{act,j}}{\tau_{act,j}} a_j + \frac{1}{\tau_{act,j}} ([\beta_{act,j} - 1] a_j + 1) n_j, \quad (5.15)$$

where  $\beta$  is the ratio of the muscle activation time  $\tau_{act}$  to the muscle deactivation time  $\tau_{deact}$ . This results in a total of six state equations for the given two muscle system.

Further considering the state equations, a chain structure can be identified. Taking equations (5.11) and (5.12) as a block, they are a function of the next block of state equations, which are for  $\dot{LS}_j$ .  $\dot{LC}_j$  appear in these equations and are a function of the  $\dot{a}_j$ , which can be seen as the final block of state equations. This structure suggests that the system could be a candidate for backstepping control.

### 5.3.2 Overview of Backstepping Control

Backstepping control belongs to the Lyapunov-based control family. The concept is generally that a stable controller can be constructed by consecutively addressing each layer of a system's dynamics [60, 62, 66]. Typical assumptions associated with backstepping include that the first state equation has a known stabilizing controller and associated Lyapunov function and that the entire system fits a strict-feedback

structure. A strict-feedback model implies that consecutive states appear in an affine manner and the control, which also enters the system affinely, is only accessible at the end of such a chain

$$\begin{aligned}
\dot{x}_1 &= f_1(x_1) + g_1(x_1)x_2 \\
\dot{x}_2 &= f_2(x_1, x_2) + g_2(x_1, x_2)x_3 \\
&\vdots \\
\dot{x}_{n-1} &= f_{n-1}(x_1, x_2, \dots, x_{n-1}) + g_{n-1}(x_1, x_2, \dots, x_{n-1})x_n \\
\dot{x}_n &= f_n(x_1, x_2, \dots, x_n) + g_n(x_1, x_2, \dots, x_n)u.
\end{aligned} \tag{5.16}$$

Reference [66] presents backstepping for a pure-feedback system as well, which is more general than a strict-feedback system. With exception of the first state equation, a pure-feedback system removes the affine state and control requirements, allowing general nonlinear functions of, once again, only the fed-back states for each state derivative.

The design of a control law via backstepping proceeds algorithmically. The steps used to recursively find a control law start with the first subsystem and can be summarized as follows:

1. Identify a variable that could act as a control input for the subsystem. This is the synthetic control.
2. Define control law with known Lyapunov function using the synthetic control.
3. Develop error term between synthetic control and selected control law.
4. Determine system dynamics when the error term is non-zero.
5. Augment known Lyapunov function with positive definite function of the error term.

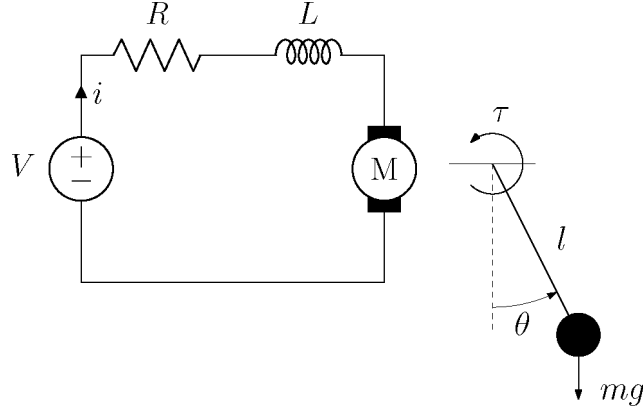


Figure 22: Bob pendulum of length  $l$  and mass  $m$  with viscous damping  $k$  actuated by a motor with armature resistance  $R$ , inductance  $L$ , and motor constant  $K_t$

6. Enforce negative definite Lyapunov derivative algebraically, producing new control law.
7. Repeat procedure for each consecutive subsystem until actual control inputs are revealed.

### Example: Pendulum Setpoint Control

A simple electromechanical system can be used to illustrate these concepts. Figure 22 shows a bob type pendulum and motor. Defining the states as  $x_1 \triangleq \theta$ ,  $x_2 \triangleq \dot{\theta}$ , and  $x_3 \triangleq i$  and selecting the control input as  $V$  produces the following dynamic system description:

$$\begin{aligned} \dot{x}_1 &= x_2 \\ \dot{x}_2 &= -\frac{g}{l} \sin(x_1) - \frac{k}{m} x_2 + \frac{K_t}{ml^2} x_3 \\ \dot{x}_3 &= -\frac{K_t}{L} x_2 - \frac{R}{L} x_3 + \frac{1}{L} V. \end{aligned} \tag{5.17}$$

It is immediately apparent that the state equations fit the definition of a strict-feedback system.

For setpoint control an error system can be developed by defining  $e_1 \triangleq x_1 - x_1^d$  and  $e_2 \triangleq \dot{e}_1$ , where  $x_1^d$  is the desired setpoint. Noting that for setpoint control  $\dot{x}_1^d = \ddot{x}_1^d = 0$ ,



transformation of the system dynamics gives

$$\begin{aligned}\dot{e}_1 &= e_2 \\ \dot{e}_2 &= -\frac{g}{l} \sin(e_1 + x_1^d) - \frac{k}{m} e_2 + \frac{K_t}{ml^2} x_3 \\ \dot{x}_3 &= -\frac{K_t}{L} e_2 - \frac{R}{L} x_3 + \frac{1}{L} V.\end{aligned}\tag{5.18}$$

To initialize the backstepping procedure,  $e_2$  is chosen as the synthetic input to the first state equation  $\zeta_1 \triangleq e_2$ . It can be seen that a control law  $\psi_1(e_1) = -e_1$  stabilizes this first state by use of the positive definite Lyapunov function  $V_1 = \frac{1}{2}e_1^2$ . Its time derivative is

$$\dot{V}_1 = e_1 \dot{e}_1 = e_1 e_2 = -e_1^2,\tag{5.19}$$

which is negative definite, meeting the requirements for stability. While this control law does indeed stabilize the system, there is nothing requiring that  $e_2$  converge to the desired control. Accordingly, stabilization of the error between the state and the control law to the origin is sought. This error is expressed as

$$w_1 = \zeta_1 - \psi_1.\tag{5.20}$$

The dynamics of state  $e_1$  when error exists are found

$$\dot{e}_1 = e_2 + \psi_1 - \psi_1 = w_1 + \psi_1.\tag{5.21}$$

Augmenting the known Lyapunov equation with a positive definite term for this error results in

$$V_{1a} = V_1 + \frac{1}{2}w_1^2.\tag{5.22}$$

The time derivative evaluated along state trajectories under the assumption that  $w_1$

is potentially non-zero, recall (5.21), is

$$\begin{aligned}\dot{V}_{1a} &= e_1 \dot{e}_1 + w_1 \dot{w}_1 = e_1(w_1 + \dot{\psi}_1) + w_1(\dot{e}_2 - \dot{\psi}_1) \\ &= -e_1^2 + w_1 \left[ e_1 - \frac{g}{l} \sin(e_1 + x_1^d) - \frac{k}{m} e_2 + \frac{K_t}{ml^2} x_3 + e_2 \right].\end{aligned}\quad (5.23)$$

To obtain a negative definite Lyapunov derivative, the term in square brackets is set equal to  $-\gamma_1 w_1$  with gain  $\gamma_1 > 0$

$$e_1 - \frac{g}{l} \sin(e_1 + x_1^d) - \frac{k}{m} e_2 + \frac{K_t}{ml^2} x_3 + e_2 = -\gamma_1 w_1. \quad (5.24)$$

Clearly,  $\dot{V}_{1a} \leq \dot{V}_1$  under these circumstances. Solving for  $x_3$

$$x_3 = -\frac{ml^2}{K_t} \left( (1 + \gamma_1)(e_1 + e_2) - \frac{g}{l} \sin(e_1 + x_1^d) - \frac{k}{m} e_2 \right) \quad (5.25)$$

leads to an intermediate control law. If  $x_3$  meets this equality, the pendulum will be controlled to  $x_1^d$ . However,  $x_3$  is not the actual control input. A second backstepping recursion can be completed to determine the control  $V$  that enforces that  $x_3$  meets the equality (5.25).

In the same way as before, a synthetic control is selected from the state derivative equation for  $e_2$ . In this case  $\zeta_2 \triangleq x_3$ . A stabilizing control law with known Lyapunov equation was already determined in the previous step; assign  $\psi_2 =$  equation (5.25). To make the state  $x_3$  follow this condition, again develop an error between the state and its desired value

$$w_2 = \zeta_2 - \psi_2 = x_3 + \frac{ml^2}{K_t} \left( (1 + \gamma_1)(e_1 + e_2) - \frac{g}{l} \sin(e_1 + x_1^d) - \frac{k}{m} e_2 \right). \quad (5.26)$$

The dynamics for  $e_2$  under this error are

$$\begin{aligned}\dot{e}_2 &= -\frac{g}{l} \sin(e_1 + x_1^d) - \frac{k}{m} e_2 + \frac{K_t}{ml^2} x_3 + \frac{K_t}{ml^2} \psi_2 - \frac{K_t}{ml^2} \psi_2 \\ &= -\frac{g}{l} \sin(e_1 + x_1^d) - \frac{k}{m} e_2 + \frac{K_t}{ml^2} w_2 + \frac{K_t}{ml^2} \psi_2.\end{aligned}\tag{5.27}$$

Once more augmenting the Lyapunov function to ensure stability

$$V_{2a} = V_{1a} + \frac{1}{2} w_2^2,\tag{5.28}$$

and taking its time derivative

$$\begin{aligned}\dot{V}_{2a} &= e_1 \dot{e}_1 + w_1 \dot{w}_1 + w_2 \dot{w}_2 \\ &= e_1(w_1 + \psi_1) + w_1(\dot{e}_2 - \dot{\psi}_1) \\ &\quad + w_2 \left( \dot{x}_3 + \frac{ml^2}{K_t} \left( (1 + \gamma_1)(\dot{e}_1 + \dot{e}_2) - \frac{g}{l} \cos(e_1 + x_1^d) \dot{e}_1 - \frac{k}{m} \dot{e}_2 \right) \right) \\ &= -e_1^2 + w_1 \left( e_1 - \frac{g}{l} \sin(e_1 + x_1^d) - \frac{k}{m} e_2 + \frac{K_t}{ml^2} w_2 + \frac{K_t}{ml^2} \psi_2 + e_2 \right) \\ &\quad + w_2 \left[ -\frac{K_t}{L} e_2 - \frac{R}{L} x_3 + \frac{V}{L} + \frac{ml^2}{K_t} \left( \left( 1 + \gamma_1 - \frac{g}{l} \cos(e_1 + x_1^d) \right) (w_1 + \psi_1) \right. \right. \\ &\quad \left. \left. + \left( 1 + \gamma_1 - \frac{k}{m} \right) \left( -\frac{g}{l} \sin(e_1 + x_1^d) - \frac{k}{m} e_2 + \frac{K_t}{ml^2} w_2 + \frac{K_t}{ml^2} \psi_2 \right) \right) \right] \\ &= -e_1^2 - \gamma_1 w_1^2 + w_2 \left[ -\frac{K_t}{L} e_2 - \frac{R}{L} x_3 + \frac{V}{L} \right. \\ &\quad \left. + \frac{ml^2}{K_t} \left( \left( 1 + \gamma_1 - \frac{g}{l} \cos(e_1 + x_1^d) \right) (w_1 + \psi_1) \right. \right. \\ &\quad \left. \left. + \left( 1 + \gamma_1 - \frac{k}{m} \right) \left( -\frac{g}{l} \sin(e_1 + x_1^d) - \frac{k}{m} e_2 + \frac{K_t}{ml^2} w_2 + \frac{K_t}{ml^2} \psi_2 \right) \right) \right].\end{aligned}\tag{5.29}$$

If the term in square brackets is made equal to  $-\gamma_2 w_2$ ,  $\dot{V}_{2a}$  is negative definite, and  $\dot{V}_{2a} \leq \dot{V}_{1a}$ .

$$\begin{aligned}-\frac{K_t}{L} e_2 - \frac{R}{L} x_3 + \frac{V}{L} + \frac{ml^2}{K_t} \left( \left( 1 + \gamma_1 - \frac{g}{l} \cos(e_1 + x_1^d) \right) (w_1 + \psi_1) \right. \\ \left. + \left( 1 + \gamma_1 - \frac{k}{m} \right) \left( -\frac{g}{l} \sin(e_1 + x_1^d) - \frac{k}{m} e_2 + \frac{K_t}{ml^2} w_2 + \frac{K_t}{ml^2} \psi_2 \right) \right) = -\gamma_2 w_2\end{aligned}\tag{5.30}$$

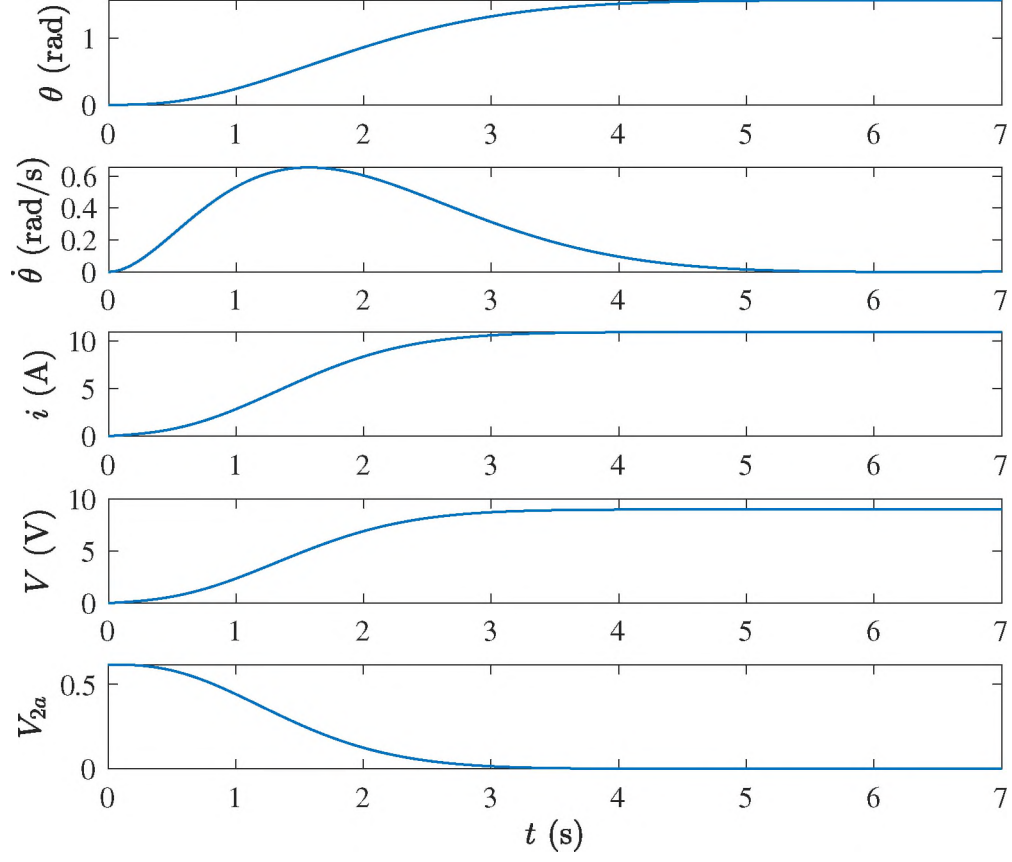


Figure 23: Simulated state and control trajectories and Lyapunov function  $V_{2a}$  for the motor-driven bob pendulum under backstepping control. The angle  $\theta$  converges to the desired setpoint and requires a constant control input  $V$  to maintain the position.

The actual control  $V$  appears in equation (5.30). Solving for  $V$  gives the final control law.

$$\begin{aligned}
 V = & L \left( \frac{K_t}{L} e_2 + \frac{R}{L} x_3 - \frac{ml^2}{K_t} \left( \left( 1 + \gamma_1 - \frac{g}{l} \cos(e_1 + x_1^d) \right) (w_1 + \psi_1) \right. \right. \\
 & \left. \left. + \left( 1 + \gamma_1 - \frac{k}{m} \right) \left( -\frac{g}{l} \sin(e_1 + x_1^d) - \frac{k}{m} e_2 + \frac{K_t}{ml^2} w_2 + \frac{K_t}{ml^2} \psi_2 \right) \right) - \gamma_2 w_2 \right), \quad (5.31)
 \end{aligned}$$

which can be rewritten as a function of the states alone. It is observed that even for a simple system, control law complexity increased rapidly. This is common for backstepping and is often referred to as “explosion of terms.”

Figure 23 illustrates a simulation of the behavior of the system under the constructed control law for zero initial conditions,  $x_1^d = \frac{\pi}{2}$ , and  $\gamma_1 = \gamma_2 = 1$ . System

parameters were selected as  $m = 0.2$  kg,  $l = 0.3$  m, and  $k = 0.1 \frac{\text{N s}}{\text{rad}}$ , and the motor is modeled using values for a Maxon RE 65 24 V motor. Indeed,  $\theta$  moves to  $x_1^d = \frac{\pi}{2}$ , and the pendulum settles there as indicated by  $\dot{\theta}$ . A steady-state current, pointing to a constant torque to hold the system, is established. An associated steady-state control input  $V$  also occurs. The slow movement stays well within the motor's operating conditions. A faster response can be obtained by tuning, and the addition of a geared transmission would allow for faster setpoint changes beyond the current operating conditions. Lastly, the Lyapunov function for the system and controller combination is always positive and decreasing as constructed.

### 5.3.3 Pure-Feedback (Modified Strict-Feedback) Dynamics

Returning to the muscle actuated mass system, the model can be transformed into a format closer to strict-feedback form by utilizing the change of variables  $-LC_j = u_j$  and performing the appropriate substitutions. The final dynamic model is

$$\dot{x}_1 = x_2 \tag{5.32}$$

$$\dot{x}_2 = \frac{1}{m} (\Phi_{S_2}(LS_2) - \Phi_{S_1}(LS_1)) \tag{5.33}$$

$$\dot{LS}_1 = x_2 + u_1 \tag{5.34}$$

$$\dot{LS}_2 = -x_2 + u_2 \tag{5.35}$$

$$\dot{u}_1 = \frac{dg_1^{-1}(z_1)}{dz_1} \frac{dz_1}{dt} = g_1^{-\nu}(z_1) \dot{z}_1 \tag{5.36}$$

$$\dot{u}_2 = \frac{dg_2^{-1}(z_2)}{dz_2} \frac{dz_2}{dt} = g_2^{-\nu}(z_2) \dot{z}_2, \tag{5.37}$$

where the functions  $\dot{u}_j$  have the form

$$\dot{u}_j = f_{1j}(x_1, LS_j, u_j) + f_{2j}(x_1, x_2, LS_j, u_j) n_j \tag{5.38}$$

with general functions of the states  $f_{ij}$  for  $i = 1, 2$ . Clearly, the dynamics fit the definition of a pure-feedback system, but the nonlinear introduction of the next states in (5.33) precludes identifying the stronger strict-feedback form. Viewing the latter four state equations as vectorial pairs, however, they are in strict-feedback form. While having these states in strict-feedback form does not change the pure-feedback classification, this feature simplifies the controller construction process.

#### 5.3.4 Pole Placement Based Backstepping Control

The stated goal for the muscle-driven mass system is that the mass follow a specified trajectory. Accordingly, selecting  $e_1 \triangleq x_1 - x_1^d$  and  $e_2 \triangleq \dot{e}_1$ , where  $x_1^d$  is the desired trajectory, gives the error system

$$\dot{e}_1 = e_2 \quad (5.39)$$

$$\dot{e}_2 = \frac{1}{m}(\Phi_{S2}(LS_2) - \Phi_{S1}(LS_1)) - \ddot{x}_1^d(t) \quad (5.40)$$

$$\dot{LS}_1 = e_2 + \dot{x}_1^d + u_1 \quad (5.41)$$

$$\dot{LS}_2 = -e_2 - \dot{x}_1^d + u_2 \quad (5.42)$$

$$\dot{u}_1 = f_{11}(e_1 + x_1^d, LS_1, u_1) + f_{21}(e_1 + x_1^d, e_2, LS_1, u_1)n_1 \quad (5.43)$$

$$\dot{u}_2 = f_{12}(e_1 + x_1^d, LS_2, u_2) + f_{22}(e_1 + x_1^d, e_2, LS_2, u_2)n_2. \quad (5.44)$$

Two synthetic inputs are chosen. For the first pair of equations  $\zeta_1 \triangleq \frac{1}{m}(\Phi_{S2}(LS_2) - \Phi_{S1}(LS_1)) - \ddot{x}_1^d(t)$ . For the second pair  $\zeta_2 = \begin{bmatrix} \zeta_{21} \\ \zeta_{22} \end{bmatrix} \triangleq \begin{bmatrix} \dot{x}_1^d + u_1 \\ -\dot{x}_1^d + u_2 \end{bmatrix}$ . Rewriting the now linear system (5.39) and (5.40),

$$\dot{e} = Ae + B\zeta_1. \quad (5.45)$$

Also,

$$\dot{L}S = \begin{bmatrix} 1 \\ -1 \end{bmatrix} e_2 + \zeta_2. \quad (5.46)$$

### First Synthetic Design

Considering this linear system, a pole-placement control law can be used for the first synthetic control  $\psi_1(e) = -Ke$ . Stability requires that the closed loop system  $A_{cl} \triangleq A - BK$  have negative real parts of the eigenvalues. For backstepping a Lyapunov function must be established for this closed loop system. It is well known that

$$V_1 = \frac{1}{2}e^T P e, \quad P = P^T > 0 \quad (5.47)$$

is positive definite with the negative definite time derivative evaluated along state trajectories

$$\dot{V}_1 = -\frac{1}{2}e^T Q e \quad \text{where} \quad -Q = PA_{cl} + A_{cl}^T P, \quad Q = Q^T > 0. \quad (5.48)$$

Enforcement of  $\psi_1$  requires that the selected synthetic control converge to  $\psi_1$ . Convergence can be measured by the error  $w_1 = \zeta_1 - \psi_1$ . Revealing  $w_1$  in the system dynamics,

$$\dot{e} = Ae + Bw_1 + B\psi_1. \quad (5.49)$$

Augmenting the Lyapunov function with  $w_1$  to require convergence to zero gives

$$V_{1a} = \frac{1}{2}e^T P e + \frac{1}{2}w_1^2 \quad (5.50)$$

for which the time derivative along state trajectories under the error  $w_1$  is

$$\begin{aligned} \dot{V}_{1a} = & -\frac{1}{2}e^T Q e + w_1 \left[ e^T P B + \frac{1}{m} \Phi'_{S2}(LS_2)(-e_2 + \zeta_{22}) \right. \\ & \left. - \frac{1}{m} \Phi'_{S1}(LS_1)(e_2 + \zeta_{21}) - \ddot{x}_1^d + K A e + K B \zeta_1 \right]. \end{aligned} \quad (5.51)$$

The term in square brackets can be made negative definite algebraically if it is set equal to  $-\gamma_1 w_1$ . This equality can be written as

$$\begin{aligned} \begin{bmatrix} \Phi'_{S1}(LS_1) & -\Phi'_{S2}(LS_2) \end{bmatrix} \zeta_2 = & m(B^T P + K A + \gamma_1 K) e \\ & - m \ddot{x}_1^d - (\Phi'_{S1}(LS_1) + \Phi'_{S2}(LS_2)) e_2 \\ & + (K B + \gamma_1)(\Phi_{S2}(LS_2) - \Phi_{S1}(LS_1) - m \ddot{x}_1^d), \end{aligned} \quad (5.52)$$

where  $\gamma_1 = \gamma_1^T > 0$ . The redundant actuator structure of the system has become apparent at this point; this equation is underdetermined. A mathematically straightforward method to resolve this redundancy is to use a least-squares solution. A solution by this means would minimize  $u_1^2 + u_2^2$ , which according to (5.6) indirectly affects the muscle activations. Due to the linearity of the problem, the Moore-Penrose pseudoinverse can be used

$$\begin{aligned} \zeta_2^* = \begin{bmatrix} \zeta_{21}^* \\ \zeta_{22}^* \end{bmatrix} = & \begin{bmatrix} \Phi'_{S1}(LS_1) \\ -\Phi'_{S2}(LS_2) \end{bmatrix} \frac{1}{\Phi_{S1}'^2(LS_1) + \Phi_{S2}'^2(LS_2)} \\ & \left( m(B^T P + K A + \gamma_1 K) e - (\Phi'_{S1}(LS_1) + \Phi'_{S2}(LS_2)) e_2 \right. \\ & \left. - m \ddot{x}_1^d + (K B + \gamma_1)(\Phi_{S2}(LS_2) - \Phi_{S1}(LS_1) - m \ddot{x}_1^d) \right). \end{aligned} \quad (5.53)$$

The resulting equation defines the requirement for  $\zeta_2$  as input to (5.46) for the pole-placement control law to hold.



## Second Synthetic Design

By the same approach a control law  $\psi_2$  that links the next pair of equations in the chain can be enforced.  $\psi_2$  is set equal to equation (5.53). The required error is written  $w_2 = \zeta_2 - \psi_2$ , and (5.46) under the error  $w_2$  is

$$\dot{L}S = \begin{bmatrix} 1 \\ -1 \end{bmatrix} e_2 + w_2 + \psi_2. \quad (5.54)$$

By augmenting the Lyapunov function

$$V_{2a} = \frac{1}{2}e^T P e + \frac{1}{2}w_1^2 + \frac{1}{2}w_2^T w_2 \quad (5.55)$$

and computing its time derivative along state trajectories

$$\begin{aligned} \dot{V}_{2a} = & -\frac{1}{2}e^T Q e + w_1 \left( B^T P e + \frac{1}{m} \Phi' \left( \begin{bmatrix} 1 \\ -1 \end{bmatrix} e_2 + \psi_2 \right) \right. \\ & \left. - \ddot{x}_1^d + K A e + K B \zeta_1 \right) + w_2^T \left\{ \begin{bmatrix} \ddot{x}_1^d + \dot{u}_1 \\ -\ddot{x}_1^d + \dot{u}_2 \end{bmatrix} - \dot{\psi}_2 + \frac{1}{m} w_1 \Phi'^T \right\}, \end{aligned} \quad (5.56)$$

where  $\Phi' = [-\Phi'_{S1}(LS_1) \ \Phi'_{S2}(LS_2)]$ , it is seen that a similar structure for the Lyapunov derivative arises. The term marked by curly braces can be made negative definite by setting it equal to  $-\gamma_2 w_2$ , where  $\gamma_2 = \gamma_2^T > 0$

$$\begin{bmatrix} \ddot{x}_1^d + \dot{u}_1 \\ -\ddot{x}_1^d + \dot{u}_2 \end{bmatrix} - \dot{\psi}_2 + \frac{1}{m} w_1 \Phi'^T = -\gamma_2 w_2. \quad (5.57)$$

The final control law is revealed by writing (5.38) in matrix form

$$\begin{bmatrix} \dot{u}_1 \\ \dot{u}_2 \end{bmatrix} = \begin{bmatrix} f_{11} \\ f_{12} \end{bmatrix} + \begin{bmatrix} f_{21} & 0 \\ 0 & f_{22} \end{bmatrix} \begin{bmatrix} n_1 \\ n_2 \end{bmatrix} \quad (5.58)$$

and substituting into (5.57)

$$\begin{bmatrix} n_1 \\ n_2 \end{bmatrix} = \begin{bmatrix} f_{21} & 0 \\ 0 & f_{22} \end{bmatrix}^{-1} \left( -\gamma_2(\zeta_2 - \psi_2) + \dot{\psi}_2 - \frac{1}{m}(\zeta_1 + Ke)\Phi^{rT} - \begin{bmatrix} \ddot{x}_1^d \\ -\ddot{x}_1^d \end{bmatrix} - \begin{bmatrix} f_{11} \\ f_{12} \end{bmatrix} \right). \quad (5.59)$$

All terms included in the control can be rewritten as expressions of the system states. In particular, note that  $\dot{\psi}_2$  can be found analytically from (5.53). The control law is feasible as long as the  $f_{2j}$  for  $j = 1, 2$  remain non-zero. According to (5.38), this condition only occurs when the coefficients of the controls  $n_j$  disappear, which is associated with infeasible muscle conditions such as overly large  $CE$  lengths or velocities.

### 5.3.5 Simulation and Results

To simulate the muscle actuated mass system, several functions referred to in general during the discussion of the muscle model must be further specified. In keeping with the normalized system, the nonlinear stiffness functions were fit piecewise

to curves provided in [151].

$$\Phi_{S,j}^n(LS_j^n) = \begin{cases} 0, & LS_j^n < L_{s,j} \\ 6760794.14(LS_j^n)^5 - 68434261.19(LS_j^n)^4 + 277072371.99(LS_j^n)^3 \\ \quad - 560875494.46(LS_j^n)^2 + 567666340.97LS_j^n \\ \quad - 229806913.40, & L_{s,j} < LS_j^n < 1.02L_{s,j} \\ 0.5 + 19.2308(LS_j^n - 1.02L_{s,j}), & LS_j^n > 1.02L_{s,j}, \end{cases} \quad (5.60)$$

where  $L_{s,j}$  is the tendon slack length.

$$\Phi_{P,j}^n(LC_j^m) = \begin{cases} 0, & LC_j^m < 1 \\ 8(LC_j^m)^3 - 24(LC_j^m)^2 + 24LC_j^m - 8, & LC_j^m \geq 1. \end{cases} \quad (5.61)$$

Additionally, the force-length relationship was also based on the properties described in [151] and selected as

$$f_j(LC_j) = e^{-\left(\frac{LC_j - L_{o,j}}{W L_{o,j}}\right)^2}, \quad (5.62)$$

where  $W$  determines the width of the Gaussian.

To provide the greatest insight into the fundamentals of the antagonistic muscle arrangement of this system, the muscles were simulated with identical parameters. These values are presented in Table III; most are dimensionless. The pole-placement controller was tuned to  $K = [2 \ 3]$  with  $Q = I$  to give stable poles at -1 and -2. Selecting  $\gamma_1 = 15$  and  $\gamma_2 = 15I_2$  led to the smooth convergence of errors  $w_1$  and  $w_2$  to zero.

Initial conditions were selected based on the requirements for equilibrium described in Section 5.2.2 and the mass dynamics' requirement that  $\Phi_{S1} = \Phi_{S2}$ . Any combination of  $LS_1$ ,  $LC_1$ , and  $LC_2$  could be selected, determining  $\bar{x}_1$ , and  $LS_2$  could

Parameter	Value
$L_o$	0.01 m
$V_{max}$	$10L_o$ 1/s
$L_s$	2
$W$	0.3
$\tau_{act}$	0.01 s
$\beta_{act}$	0.25
$m$	1
$A$	0.25
$g_{max}$	1.5

Table III: Muscle-actuated mass system simulation parameters [37, 54, 146, 151]

be solved from the force equality. Care was taken that neither tendon length was in the slack region, allowing a solution for  $LS_2$ . In initializing the simulation at this equilibrium point and selecting the sine wave trajectory for the mass to track,  $x_1^d(t) = 0.005\bar{x}_1 \sin(t) + 1.01\bar{x}_1$ , effort was made to restrict the range of motion to an area near the muscles' optimal properties. The system can track alternative reference trajectories. The total displacement or rate of displacement required of the mass for a given trajectory in combination with the initial conditions determines whether the modeled muscles stay within the allowable ranges for  $u_j$ ,  $a_j$ , and  $n_j$  and tendon remains outside of the slack region. Reference trajectories breaking the assumptions of the muscle model can lead to unstable dynamics.

In simulation it was seen that asymptotic tracking can be achieved, Figure 24. The control signals and post-calculated muscle activations, Figure 25, remain in the required range of zero to one after the transient behavior settles. Indicating that the synthetic controls are being applied effectively,  $w_1$  and  $w_2$  converge to zero in Figure 26.

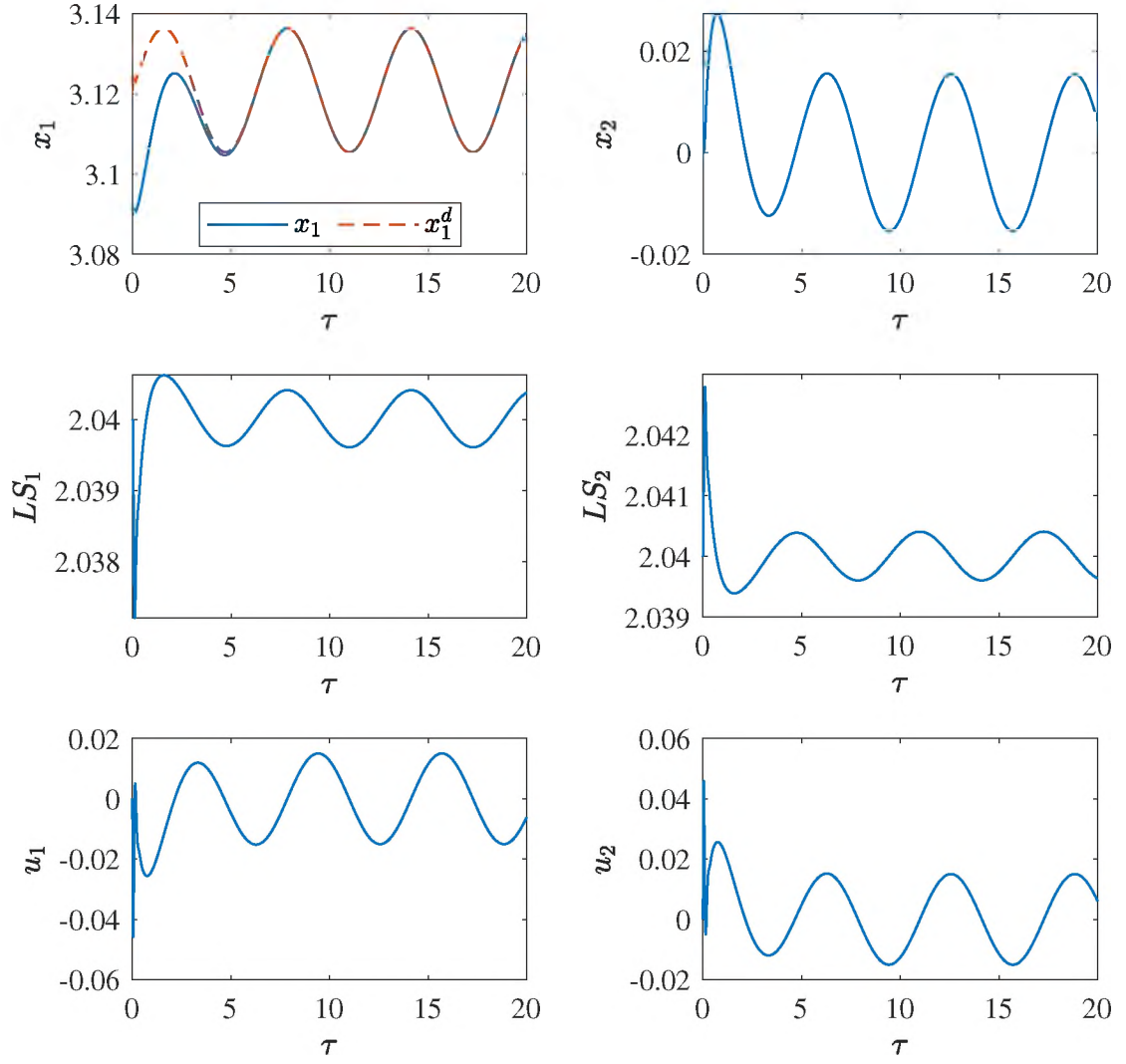


Figure 24: Trajectories of the two muscle system show convergence of the mass position  $x_1$  to the desired sinusoid  $x_1^d$  and the resulting muscle states.

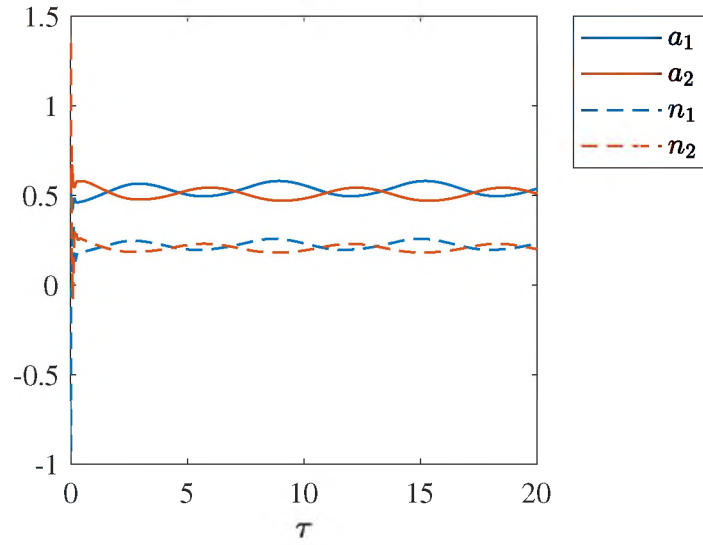


Figure 25: Two muscle system control signals and computed muscle activations

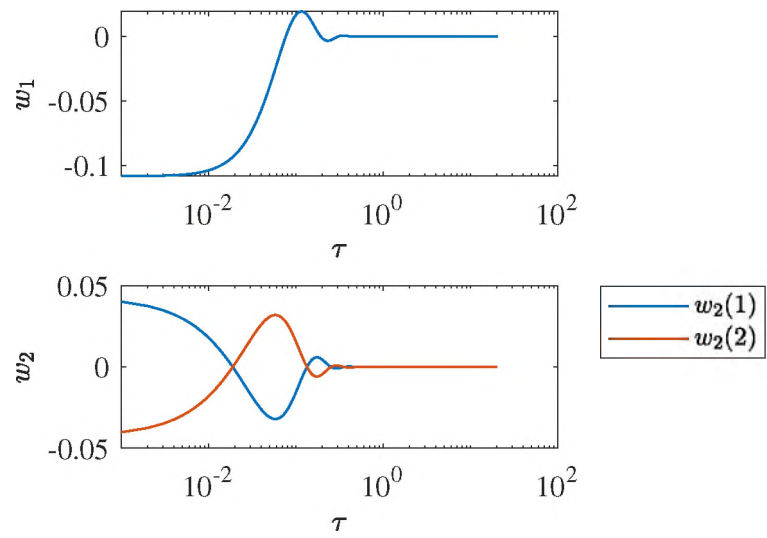


Figure 26: Errors  $w_1$  and  $w_2$  converge to zero for the two muscle system

### 5.3.6 Discussion and Summary of Findings

The completion of this preliminary study showed that muscle redundancy can be resolved and a control solution found that provides accurate tracking within the backstepping framework. Using a normalized model allowed for a general study that illustrated muscle actuator properties without specifying a human joint. Control construction through the backstepping method was shown feasible, suggesting that backstepping could allow any stabilizing controller with a known Lyapunov function to be implemented through muscle actuation. Several topics for further investigation were also identified through this study.

It can be seen from the control signals that the muscles are consistently being called on to co-contract. While it is desirable to avoid complete tendon slack, within a human joint co-contraction generally implies excess energy usage when simply tracking a trajectory without needing to obtain a specific joint impedance. However, because several features of the human system remain unmodeled within this simplified system, addressing this issue was reserved for a model containing increased muscle redundancy, cross-joint muscles, and joint moment arms as well as non-normalized dynamics.

Though not presented here, several simulation conditions exposed some concerns with the chosen activation dynamics. It was determined that this was in part due to the activation dynamics lacking an equal time constant between  $a_j$  and  $n_j$  as shown by manipulating the activation dynamics

$$\dot{a}_j = - \left[ \frac{1}{\tau_{act,j}} (\beta_{act,j} + [1 - \beta_{act,j}] n_j) \right] a_j + \frac{1}{\tau_{act,j}} n_j. \quad (5.63)$$

For example, when the variable time constant of  $a_j$  becomes small, the operator produces a large gain between  $n_j$  and  $a_j$ . A non-unity gain is already evidenced for the

$n_j$  and  $a_j$  trajectories in Figure 25, even when they remain in  $[0,1]$ . Accordingly, this simulation provided the impetus to consider alternative activation dynamics options in future muscle-actuated simulations.

## 5.4 Muscle-Actuated Linkage

The muscle-actuated linkage simulation increases the complexity of the system to include cross-joint muscles and more redundant muscle pairs. It also allows for direct comparisons to be made with published data if the linkage is parameterized to, for example, a human arm or leg. The work presented in this section is being published in [140].

### 5.4.1 Muscle Actuated Linkage Model

The model used to represent the human system developed in this work from a robotics perspective can be viewed as two subsystems, the linkage, or skeleton, and the actuators, or muscles. Additionally, a coupling mechanism between the actuators and linkage must be identified.

#### Linkage Dynamics

The dynamics of a robotic system are given by

$$D(q)\ddot{q} + C(q, \dot{q})\dot{q} + g(q) = \tau, \quad (5.64)$$

where  $D$  is the mass matrix,  $C$  is the Coriolis matrix,  $g$  is the gravity vector, and  $\tau$  is the input vector.

#### *Example: Human Arm*

A human arm operating in two dimensions can be seen as a two-link planar



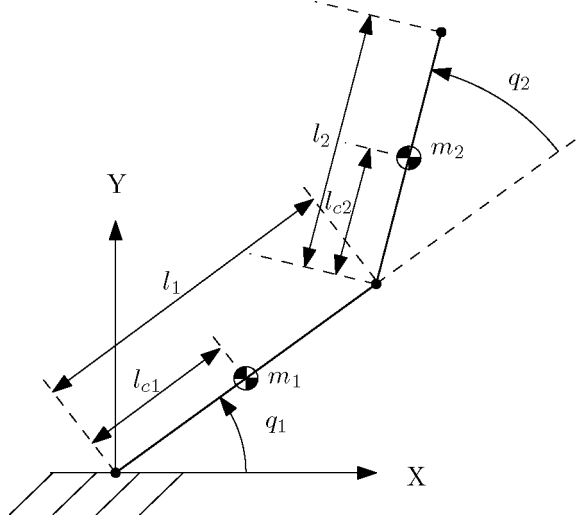


Figure 27: Two degree of freedom planar robot schematic with joint coordinates  $q_1$  and  $q_2$

robot as shown in Figure 27. Specifically considering the case where the arm operates in the horizontal plane, the details of (5.64) can be assigned as

$$D(1,1) = m_1 l_{c1}^2 + m_2 (l_1^2 + l_{c2}^2 + 2l_1 l_{c2} \cos(q_2)) + I_1 + I_2$$

$$D(1,2) = D(2,1) = m_2 (l_{c2}^2 + l_1 l_{c2} \cos(q_2)) + I_2$$

$$D(2,2) = m_2 l_{c2}^2 + I_2$$

$$C(1,1) = h\dot{q}_2 \tag{5.65}$$

$$C(1,2) = h\dot{q}_2 + h\dot{q}_1$$

$$C(2,1) = -h\dot{q}_1$$

$$C(2,2) = 0, \quad h = -m_2 l_1 l_{c2} \sin(q_2)$$

$$g(q) = 0,$$

where  $m_i$  is the mass,  $l_i$  is the length,  $l_{ci}$  is the distance from joint  $i$  to the center of mass, and  $I_i$  is the mass moment of inertia of link  $i$  [114].

## Muscle Actuator Dynamics

Non-normalized Hill muscles as described in Section 5.2.1 are used to actuate the linkage. The activation dynamics of each muscle were updated based on observations made in Section 5.3.6 and can be defined by the following differential equation, implying a first-order lag with bounded time constant and unity DC gain

$$\dot{a}_j = \sigma(n_j)(n_j - a_j), \text{ where } \sigma(n_j) = \frac{C_1}{1 + e^{-C_2(n_j + C_3)}} + C_4. \quad (5.66)$$

The  $C$ s in (5.66) are coefficients to be fit to a linear function with upper and lower saturation limits such that

$$\sigma(n_j) \approx \begin{cases} \frac{1}{\tau_{deact}}, & n_j \leq 0 \\ \frac{1}{\tau_{act}}, & n_j \geq 1 \\ \frac{n_j}{\tau_{act}} + \frac{1-n_j}{\tau_{deact}}, & \text{otherwise,} \end{cases} \quad (5.67)$$

where  $\tau_{act}$  and  $\tau_{deact}$  are the muscle activation and deactivation time constants, respectively. Equation (5.67) is of the general form given in [34], which provides the unity DC gain, and has been modified by use of a sigmoid to maintain a smooth, bounded time constant.

## Linkage-Muscle Actuator Coupling

In this model the muscles create torques to drive the linkage by generating forces  $\Phi_{S,j}$  that are applied to constant moment arms, as modeled in [48]. The moment arm can be derived from the conservation of power for a given muscle  $j$  at joint  $i$

$$-\Phi_{S,j}\dot{L}_j = \tau_{ij}\dot{q}_i \implies \tau_{ij} = -\frac{\partial L_j}{\partial q_i}\Phi_{S,j}, \quad (5.68)$$

where  $\tau_{ij}$  is the torque developed about joint  $i$  by muscle  $j$ . Therefore, given the length of muscle  $j$  as a function of the joint coordinates  $q$ , the moment arm can be defined as  $-\frac{\partial L_j}{\partial q_i}$  [5]. Considering multiple muscles, the cumulative torque  $\tau_i$  for each joint  $i$  is

$$\tau_i = \sum_{j \in J_i} \tau_{ij}, \quad (5.69)$$

where  $J_i$  is the set of the indices of all muscles affecting joint  $i$ .

### ***Example: Human Arm***

According to [48], a suitable muscle length function for the planar arm is

$$L_j = a_{0,j} - d_{1,j}q_1 - d_{2,j}q_2, \quad (5.70)$$

where  $a_{0,j}$ ,  $d_{1,j}$ , and  $d_{2,j}$  are constants. This implies constant moment arms, establishing a pulley-type system.

### **Pure Feedback Model Realization**

In summary, the system dynamics are given by (5.64), (5.1), and (5.66). Constraints (5.5) and (5.6) must hold to satisfy the muscle dynamics. Equations (5.68) and (5.69) couple the linkage and actuator subsystems.

As was noted in the two-muscle system, this system is structured such that each of the consecutive state equations appear as a chain, suggesting that the system is a candidate for the backstepping procedure. Specifically, the inputs to (5.64) are functions of the  $LS_j$  according to (5.68). Similarly, the  $\dot{LC}_j$ , which could be viewed as the inputs to (5.1), are a function of the final states  $a_j$  as seen in (5.5) and (5.6).

The dynamics can be reformulated as a pure-feedback system to further reveal the aforementioned structure. Under the change of variables  $-\dot{LC}_j = u_j$  and definitions

$x_1 \triangleq q$  and  $x_2 \triangleq \dot{q}$ , the dynamic equations can be written in state space as

$$\dot{x}_1 = x_2 \quad (5.71)$$

$$\dot{x}_2 = D^{-1}(x_1)(-C(x_1, x_2)x_2 - g(x_1) + \tau) \quad (5.72)$$

$$\dot{LS}_j = \dot{L}_j(x_2) + u_j \quad (5.73)$$

$$\dot{u}_j = \frac{dg_j^{-1}(z_j)}{dz_j} \frac{dz_j}{dt} = g_j^{-1\prime}(z_j)\dot{z}_j, \quad (5.74)$$

where the term  $\dot{z}_j$  absorbs the state derivative  $\dot{a}_j$ . To show that the appropriate states appear within the final state equation, consider that  $g_j^{-1}(z_j) = u$  implies that  $z_j = g_j(u)$ . Several further substitutions can be made based on previous definitions to reveal the general form

$$\dot{u}_j = f_{1j}(x_1, LS_j, u_j, n_j)\sigma(n_j) + f_{2j}(x_1, x_2, LS_j, u_j) \quad (5.75)$$

for the  $u_j$  state derivative equations.

### 5.4.2 Inverse Dynamics Based Backstepping Control

#### First Synthetic Design

Mirroring the two-muscle case where the cumulative force was selected as the first synthetic control, the first synthetic control  $\zeta_1$  for the muscle-actuated linkage model can be selected as the input torque vector  $\zeta_1 \triangleq \tau$ . The associated synthetic control law is denoted  $\psi_1(e)$ , where  $e = [\tilde{q}^T \ \dot{\tilde{q}}^T]^T$  with  $\tilde{q} \triangleq q - q^d$  and  $\dot{\tilde{q}} \triangleq \dot{q} - \dot{q}^d$ . The superscript  $d$  denotes desired trajectory.

Inverse dynamics has been selected to accomplish the goal of tracking control with the muscle-actuated linkage model. It is perhaps one of the most fundamental robotics control methods and is suitable for illustrating the backstepping approach for this specific problem. Alternative controllers with known Lyapunov functions could

also be considered. Making the synthetic feedback law explicit,

$$\psi_1(e) = Ma + C(q, \dot{q})\dot{q} + g(q), \quad (5.76)$$

where  $a = \ddot{q}^d - K_d\dot{\tilde{q}} - K_p\tilde{q}$  is the synthetic acceleration associated with inverse dynamics and  $K_p$  and  $K_d$  are diagonal, positive gain matrices.

Application of the control law generates the error dynamics

$$\dot{e} = Ae \quad (5.77)$$

where

$$A = \begin{bmatrix} 0 & I \\ -K_p & -K_d \end{bmatrix}. \quad (5.78)$$

For such a linear system the Lyapunov function

$$V_1 = e^T Pe, \quad (5.79)$$

where  $P = P^T > 0$  is known to be globally asymptotically stable with time derivative

$$\dot{V}_1 = -e^T Qe, \quad (5.80)$$

where  $Q = Q^T > 0$  if

$$A^T P + PA = -Q \quad (5.81)$$

holds. When  $\zeta_1 = \psi_1$ , inverse dynamics meets the requirements of an initial synthetic control law to which backstepping can be applied. Namely, tracking is achieved, and a working Lyapunov function can be identified.

Having established the first synthetic control, a means of enforcing it must be considered. Accordingly, an error between the synthetic control  $\zeta_1$  and control law

$\psi_1$  is defined

$$w_1 \triangleq \zeta_1 - \psi_1. \quad (5.82)$$

When the control law  $\psi_1$  is not being perfectly applied, the system dynamics become

$$D(q)\ddot{q} + C(q, \dot{q})\dot{q} + g(q) = \zeta_1 + \psi_1 - \psi_1 = w_1 + \psi_1. \quad (5.83)$$

Under these circumstances the controlled system dynamics are

$$D(q)\ddot{\tilde{q}} + D(q)K_d\dot{\tilde{q}} + D(q)K_p\tilde{q} = w_1. \quad (5.84)$$

Rewriting (5.84) as a function of  $e$  gives

$$\dot{e} = Ae + B_{w_1}w_1, \quad (5.85)$$

where  $B_{w_1}^T = [0 \ D^{-1}]$ .

The Lyapunov function is augmented with a positive definite term in  $w_1$  to require that  $w_1$  approach 0, which implies that the control law is successfully being applied through the synthetic control

$$V_{1a} = e^T P e + w_1^T E w_1, \quad (5.86)$$

where  $E = E^T > 0$ . Evaluating the time derivative of (5.86) along state trajectory (5.85) and using  $\dot{w}_1 = \dot{\zeta}_1 - \dot{\psi}_1$  gives

$$\dot{V}_{1a} = -e^T Q e + 2w_1^T \left[ B_{w_1}^T P e + E \left( \dot{\zeta}_1 - \dot{\psi}_1 \right) \right]. \quad (5.87)$$

Satisfying the need for  $\dot{V}_{1a}$  to be negative definite, the term within square brackets in

(5.87) can be made to follow

$$B_{w_1}^T P e + E \left( \dot{\zeta}_1 - \dot{\psi}_1 \right) = -\Gamma_1 w_1 \quad (5.88)$$

algebraically with  $\Gamma_1 = \Gamma_1^T > 0$ , resulting in a solution for  $\dot{\zeta}_1$

$$\dot{\zeta}_1 = \dot{\psi}_1 - E^{-1} \left( \Gamma_1 w_1 + B_{w_1}^T P e \right). \quad (5.89)$$

Recalling that  $\zeta_1 \triangleq \tau$  and  $\dot{L}S = \dot{L} + u$ , the derivative of  $\zeta_1$  is

$$\dot{\zeta}_1 = \left[ \frac{\partial \tau}{\partial q} \right] \dot{q} + \left[ \frac{\partial \tau}{\partial LS} \right]^T \left( \dot{L} + u \right). \quad (5.90)$$

Equation (5.90) reveals the next state in the chain of state equations  $u$ . Combining (5.89) and (5.90) results in

$$\left[ \frac{\partial \tau}{\partial LS} \right]^T u = \dot{\psi}_1 - E^{-1} \left( \Gamma_1 w_1 + B_{w_1}^T P e \right) - \left[ \frac{\partial \tau}{\partial q} \right] \dot{q} - \left[ \frac{\partial \tau}{\partial LS} \right]^T \dot{L}. \quad (5.91)$$

Notedly,  $\left[ \frac{\partial \tau}{\partial LS} \right]^T$  is not necessarily square but rather is of dimension  $\mathbb{I} \times \mathbb{J}$ , where  $\mathbb{I}$  is the number of joints and  $\mathbb{J}$  is the number of muscles; it is possible for the system to be underdetermined. Therefore, a direct solution for  $u$  by inverting this matrix coefficient is not always possible. This mathematical result is consistent with the model. A muscle-driven linkage in general will not have a one-to-one muscle actuator-to-joint ratio because of the antagonistic arrangement of muscles. Most joints include at least two muscles. Furthermore, the human body employs redundant muscles to vary joint impedance, adding more muscles to a given joint [40]. Both of these features are allowable within the control structure as long as a solution to (5.91) can be found.

## Resolving Muscle Redundancy

One option to easily resolve the control redundancy is a least squares solution for  $u$ , which can be computed by using the Moore-Penrose pseudoinverse of  $[\partial\tau/\partial LS]^T$  when solving (5.91) for  $u$ . This solution would minimize  $\sum_{j=1}^J u_j^2$ , which according to (5.6) indirectly affects the muscle activations.

Alternatively, optimization of other cost functions could be considered as long as it is constrained by exact solution of the equality (5.91). For example, it is desirable for the activations and neural signals to remain between zero and one. To address this more explicitly, one such optimization solution was developed. The control input to the system, the neural signals  $n$ , is closely related to the activation signal  $a$ ; it is being simulated as only separated by a lag. It seems likely, therefore, that constraining the activations alone to the range zero to one will lead to an implied constraint of zero to one on the neural inputs. Recalling equations (5.5) and (5.6), there is a direct connection from the  $u$ , which are being determined at this stage of the control recursion, to the activation, allowing a constraint for  $a$  to be constructed.

From experience with the system, it became clear that addressing the current time solution for the activation was not sufficient for maintaining feasibility of the proposed optimization problem. Accordingly, the optimization candidate  $u$  was used to generate an approximate predicted  $a$  for one time step  $\Delta t$  ahead as follows:

$$\begin{aligned}
 \hat{LC} &= LC - u\Delta t \\
 \hat{L} &= L - \dot{L}(q, \dot{q})\Delta t \\
 \hat{LS} &= \hat{L} - \hat{LC} \\
 \hat{a} &= \frac{\Phi_S(\hat{LS}) - \Phi_P(\hat{LC})}{f(\hat{LC})g(u)F_{max}}.
 \end{aligned} \tag{5.92}$$



Solving for  $u$  can then be stated as the following optimization problem

$$\begin{aligned} & \underset{u}{\text{minimize}} && \sum_{j=1}^J \hat{a}_j(u_j) \\ & \text{subject to} && \text{Equality (5.91) and } 0.01 \leq \hat{a}_j \leq 1 \end{aligned} \tag{5.93}$$

Note that by this method a small saturation value was able to be conveniently implemented as the lower limit for  $\hat{a}$  to prevent numerical issues in (5.6). Assuming some suitable method is selected to give a solution for the  $u$ , the next states in the chain, it is possible to transition into the second synthetic design.

## Second Synthetic Design

In (5.73)  $u$  appears in a way that suggests it as the second synthetic input  $\zeta_2 \triangleq u$ . From the results of the first synthetic design, (5.91) with  $u$  isolated on the left hand side by whatever method chosen can be selected as the synthetic feedback control law  $\psi_2$  with known Lyapunov function (5.86).

The error

$$w_2 \triangleq \zeta_2 - \psi_2 \tag{5.94}$$

must reach zero to enforce the control law through the state equations. The system dynamics when there is some error are determined by

$$\dot{L}S = \dot{L} + \zeta_2 + \psi_2 - \psi_2 = \dot{L} + w_2 + \psi_2. \tag{5.95}$$

Further augmenting the Lyapunov function with a term that is positive definite in  $w_2$  gives

$$V_{2a} = e^T P e + w_1^T E w_1 + w_2^T G w_2, \tag{5.96}$$

where  $G = G^T > 0$ . The time derivative of (5.96) along the state trajectories defined

by (5.85) and (5.95) is

$$\begin{aligned} \dot{V}_{2a} = & -e^T Q e + 2w_1^T \left( B_{w_1}^T P e + E \left[ \left[ \frac{\partial \tau}{\partial q} \right] \dot{q} + \left[ \frac{\partial \tau}{\partial LS} \right]^T (\dot{L} + \psi_2) - \dot{\psi}_1 \right] \right) \\ & + 2 \left\{ (\dot{u} - \dot{\psi}_2)^T G + w_1^T E \left[ \frac{\partial \tau}{\partial LS} \right]^T \right\} w_2. \end{aligned} \quad (5.97)$$

Requiring the term in curly braces to follow

$$(\dot{u} - \dot{\psi}_2)^T G + w_1^T E \left[ \frac{\partial \tau}{\partial LS} \right]^T = -w_2^T \Gamma_2 \quad (5.98)$$

with  $\Gamma_2 = \Gamma_2^T > 0$  results in (5.97) being negative definite.

Substituting (5.75) for  $\dot{u}$  in (5.98) and writing the result in vector form gives

$$[f_1(q, LS, u, n)\sigma(n)]^T = \left( -w_2^T + \dot{\psi}_2^T G - w_1^T E \left[ \frac{\partial \tau}{\partial LS} \right]^T \right) G^{-1} - [f_2(q, \dot{q}, LS, u)]^T. \quad (5.99)$$

This is the final control law as indicated by the appearance of the actual control inputs  $n_j$ . The equation can be solved numerically. Note that all required values are available easily from state feedback except  $\dot{\psi}_2$ , which is evaluated numerically to account for varied solution methods of (5.91). Furthermore, the control approach is insensitive to the muscle function shapes used for the force-length, force-velocity, and nonlinear elastic relationships and activation dynamics as long as some of their derivatives and inverses are available for computation.

There are several situations in which the control law fails. These primarily include extreme values of  $LC$  such that (5.62) approaches zero and conditions where  $u$  approaches  $V_{max}$  because (5.4) equals zero at that point. Such conditions can be avoided through tuning and proper selection of initial conditions, final setpoints, and settling times.

Figure 28 summarizes the system dynamics of a muscle actuated linkage and

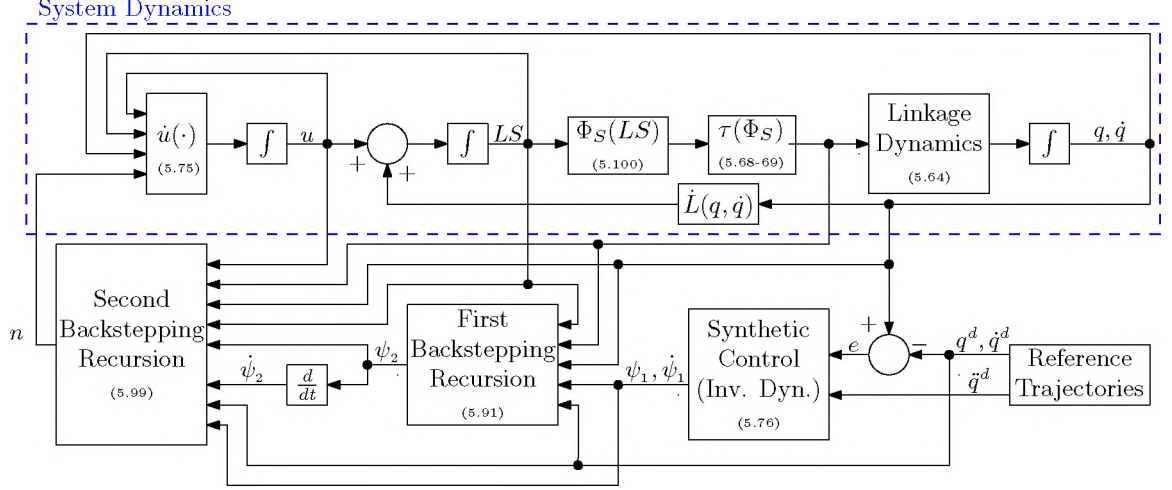


Figure 28: Block diagram of muscle-actuated linkage system dynamics and backstepping control levels. Relevant equations are referenced in parentheses

the control hierarchy of an inverse dynamics synthetic control design implemented through two recursions of backstepping.

### 5.4.3 Simulation and Results

Simulation studies of two cases for resolving muscle redundancy will be presented. The least squares method will be considered first followed by the optimization solution for bounding the activations with attention given to how the former motivated development of the latter.

### Updated Muscle Functions

Now working with a non-normalized system, new selections were made for specifying the details for the muscle system. First, for the nonlinear tendon stiffnesses a simpler, quadratic form was chosen, primarily to allow for comparison to published data.

$$\Phi_{S,j}(LS_j) = \begin{cases} \frac{10^{-3}-10^{-6}}{L_{s,j}} LS_j + 10^{-6}, & LS_j \leq L_{s,j} \\ k_{SEE}(LS_j - L_{s,j})^2, & \text{otherwise,} \end{cases} \quad (5.100)$$

where  $k_{SEE} = \frac{F_{max,j}}{(0.04L_{s,j})^2}$ . A minute slope is introduced in the slack region of this function to maintain its ability to be inverted. Scaling of the quadratic by  $k_{SEE}$  results in the tendon seeing a force of  $F_{max,j}$  when it is extended by 4% beyond the slack limit [78]. The parallel stiffness ( $PEE$ ) engages once the muscle body has been extended past the optimal fiber length  $L_{o,j}$  and has a similar structure to the  $SEE$

$$\Phi_{P,j}(LC_j) = \begin{cases} 0, & LC_j \leq L_{o,j} \\ k_{PEE}(LC_j - L_{o,j})^2, & \text{otherwise,} \end{cases} \quad (5.101)$$

where  $k_{PEE} = \frac{F_{max,j}}{(WL_{o,j})^2}$  [78]. Likewise, the force-length relationship was updated to compare with published data [78],

$$f_j(LC_j) = 1 - \frac{(LC_j - L_{o,j})^2}{W^2 L_{o,j}^2}. \quad (5.102)$$

## Human Arm System

The selected test application for the muscle-actuated linkage was the planar motion of a human arm, as setup within the previous examples in this section. A planar arm was chosen so as to advance toward applying the closed-loop muscle-actuated linkage to advanced exercise machines. The model was used directly from [48] for comparison. The arm was required to track a logistic sigmoid trajectory that was structured in the same way as (5.66) and fit to a transition from 20 to 80 degrees over 0.65 seconds for both the shoulder and elbow joints, providing a continuous, differentiable path similar to the setpoint change presented in [48]. That work uses a PD controller to accomplish the motion. The linkage is scaled according to the parameters given in Table IV.

A total of six muscles are used in this model, including two muscles that cross both joints. The muscles are oriented as shown in Figure 29. General parameters used

Parameter	Value
$m_1$	2.24 kg
$m_2$	1.76 kg
$I_1$	0.0253 kg m
$I_2$	0.0395 kg m
$l_1$	0.33 m
$l_2$	0.32 m
$l_{c1}$	0.1439 m
$l_{c2}$	0.2182 m

Table IV: Physical parameters of the linkage scaled to a human arm from [48]

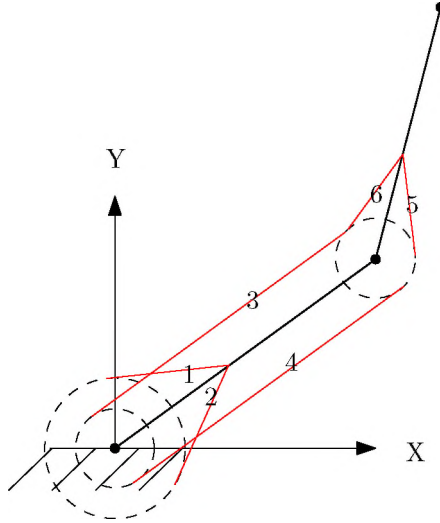


Figure 29: Locations of simulated muscles: (1) Anterior Deltoid, (2) Posterior Deltoid, (3) Biceps Brachii, (4) Triceps Brachii (long head), (5) Triceps Brachii (short head), and (6) Brachialis. Not drawn to scale

Parameter	Value
$V_{max}$	$10L_o$ m/s
$W$	0.56
$\tau_{act}$	0.01 s
$\beta_{act}$	0.25
$A$	0.25
$g_{max}$	1.5

Table V: Muscle-actuated mass system simulation parameters [7, 37, 54, 146]

Muscle ( $j$ )	$F_{max,j}$ (N)	$L_{o,j}$ (m)	$L_{s,j}$ (m)	$d_{1,j}$ (m)	$d_{2,j}$ (m)	$a_{0,j}$ (m)
Anterior Deltoid (1)	800	0.1280	0.0538	0.05	0	0.1840
Posterior Deltoid (2)	800	0.1280	0.0538	-0.05	0	0.1055
Biceps Brachii (3)	1000	0.1422	0.2298	0.03	0.03	0.4283
Triceps Brachii (longhead) (4)	1000	0.0877	0.1905	-0.03	-0.03	0.1916
Triceps Brachii (shorthead) (5)	700	0.0877	0.1905	0	-0.03	0.2387
Brachialis (6)	700	0.1028	0.0175	0	0.03	0.1681

Table VI: Muscle and moment arm properties selected for the human arm simulation from [48]

across all muscles are provided in Table V. For the individual muscles, the remaining parameters are shown in Table VI. Note that for the linkage and range of motion studied in the simulation it is assumed that  $\Phi_{P,j} = 0$  [48].

### Simulation Initialization

Initial conditions for the system were handled such that they were near equilibrium and consistent with the system dynamics and control laws; a slight slope of the sigmoid trajectory in the initial position prevented a true equilibrium. The procedure for initializing the system begins with evaluating each joint position and velocity for the first point along the generated sigmoid trajectory. Next, the initial control  $\psi_1$  was computed under these initial values, which are the same as the desired trajectory. Then an optimization solution for the  $LS$  was completed. The solution was constrained such that the selected  $LS$  were outside the slack region and led to a non-negative  $LC$ . A weighted cost function composed of the forces generated by each muscle and the difference between the resulting joint torques and initial control

$\psi_1$  was used to accomplish the specified torque without excessive co-contraction.

The  $u$  can be initialized by direct solution of (5.91) with the pseudoinverse or by an optimization routine consistent with the selected alternative method of resolving muscle redundancy. Given the initial state description and assuming  $\ddot{L}C = 0$  and  $\psi_2 = 0$  because the initial state is near equilibrium and no information is known about these values, the initial control  $n$  can be computed from (5.99). For the optimization option a constraint requiring that the initial control be non-negative was added.

### Controller Tuning

Identical controller tunings were used for simulations of both methods of resolving muscle redundancy. The lowest values of  $K_p$  and  $K_d$  for which the system would maintain stability were selected,  $K_p = 0.1I_2$  and  $K_d = 0.05I_2$ . Next, the Lyapunov equation  $A^T P + P A = -Q$  was solved for  $Q = I_4$ . The gains defining the weights on the Lyapunov function and its derivative for the first backstepping recursion were chosen as  $\Gamma_1 = I_2$  and  $E = 0.0001I_2$ . Similarly, the weights for the second backstepping recursion were set to  $\Gamma_2 = G = I_6$ .

### Results with Least Squares Muscle Redundancy Resolution

The muscle-actuated arm linkage simulation accurately tracked the generated reference trajectory as shown in Figure 30 for both joints. Compared to the results reported in [48] for a similar setpoint change under PD control, the backstepping controller under the current tuning offers no overshoot and settles directly. Considering the tendon length states  $LS$  in Figure 31, the system achieves smooth transitions and maintains stability. For this particular case the Biceps Brachii enter slack, indicating little force output. Checking internally, the synthetic control laws follow the control laws, Figure 32. The inverse dynamics control design is, therefore, being transmitted accurately through the system dynamics to the joint torques. The states  $u$  are also

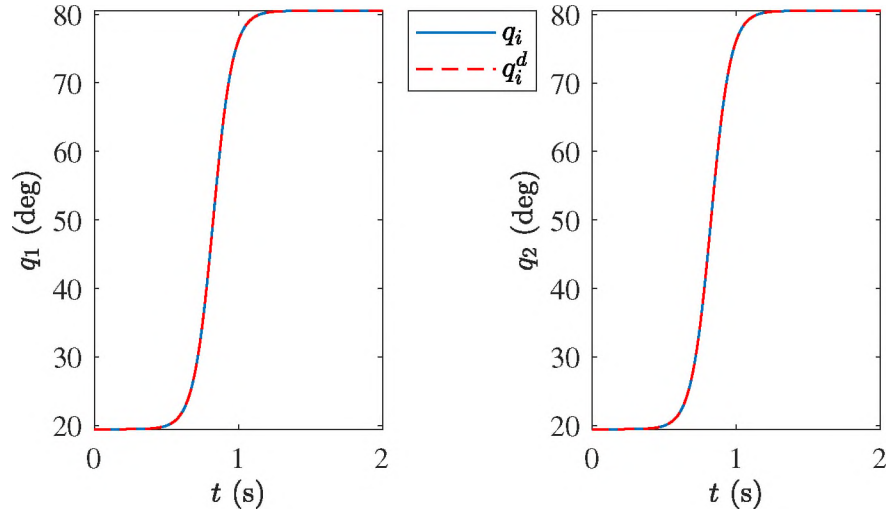


Figure 30: Least Squares Solution: Both joints attain accurate tracking of a 0.65 second long 20-80 degree transition

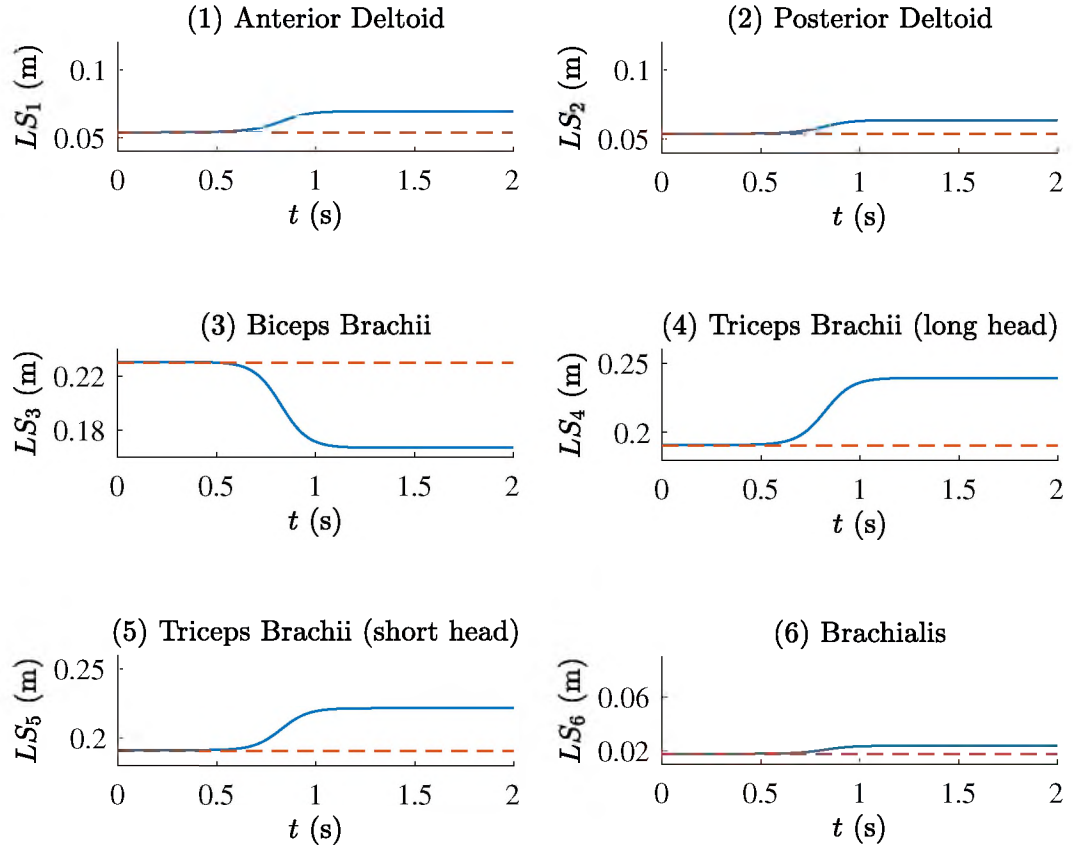


Figure 31: Least Squares Solution: Tendon length states remain bounded. Red dashed lines show slack length limits  $L_{s,j}$



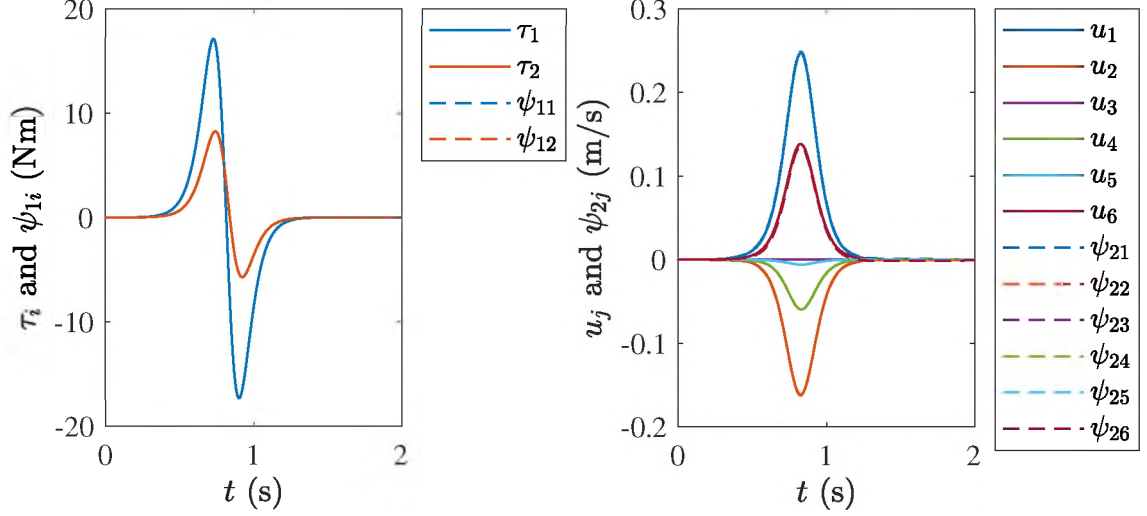


Figure 32: Least Squares Solution: Synthetic control agreement for the first (left) and second (right) recursions

shown in Figure 32. They are bounded and settle back to equilibrium.

Referring to Figure 33, the actual control signals, the neural inputs  $n$ , are overly large. The associated muscle activations are equally large but do lag the neural inputs as expected, validating the sigmoid implementation of the activation dynamics. Recall that both of these signals are supposed to range between zero and one. However, there is no feature within this control law to enforce this constraint. The source of the large control inputs can be identified by observing the individual forces generated by the muscles; see Figure 34. Upon completing the transition between desired joint angles, the forces do not settle back to zero. Because gravity is not being modeled, this is clearly due to co-contraction. Extrapolating this result backward in time, it follows that the entire movement was completed with a high joint impedance.

Further considering the root of the system's tendency toward co-contraction, recall that a similar result was observed in the two-muscle system of Section 5.3.6. The addition of more muscles and multi-joint muscles and the elimination of the normalized dynamics did not lead to notable improvement. Rather, the consistency of the co-contraction between these cases supports the possibility that the cost function, minimizing  $u$ , could be the source of the co-contraction. Considering this effect phys-

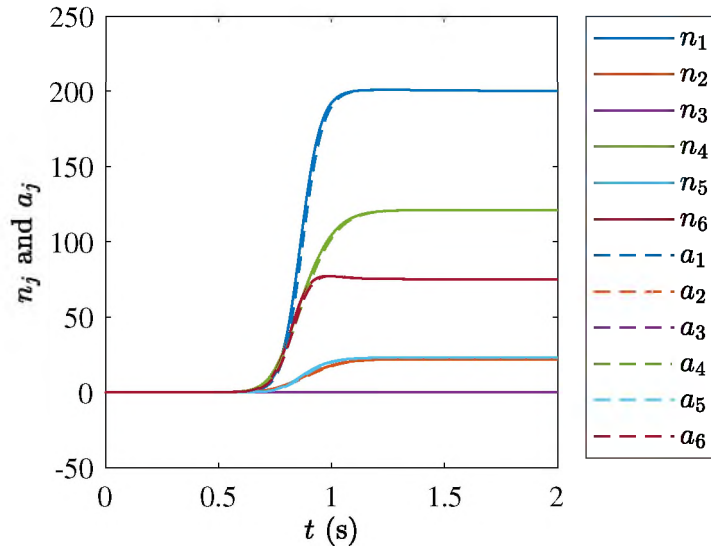


Figure 33: Least Squares Solution: Control inputs  $n$  and associated activations  $a$ , showing the effects of the first order lag

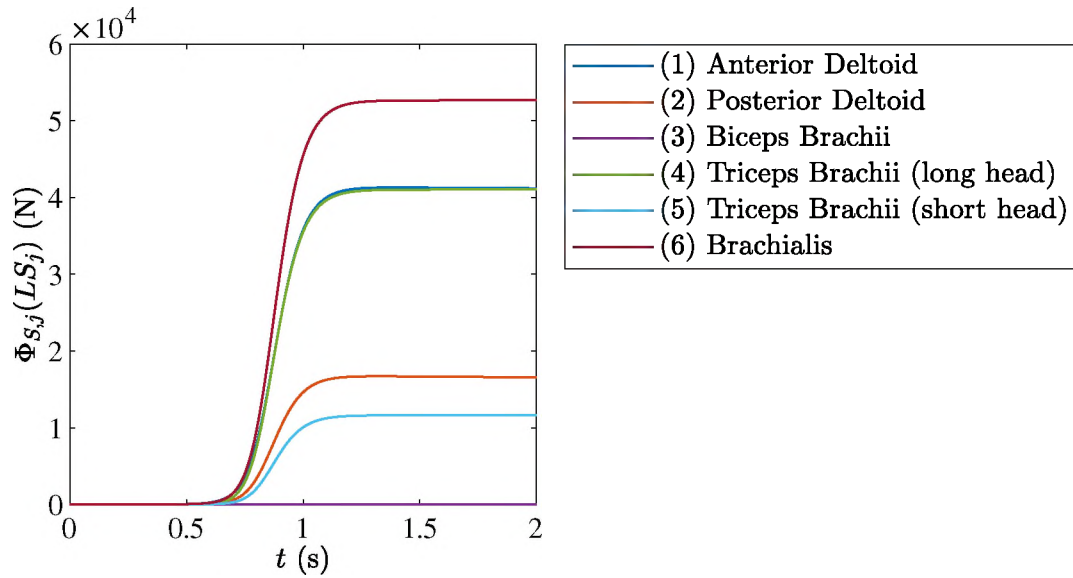


Figure 34: Least Squares Solution: Forces generated by each muscle

iologically,  $u$  can be minimized by the  $CE$  resisting movement, shifting the change in length of the muscle unit to the  $SEE$ . Dependence on the  $SEE$  for a change in length requires a change in muscle-generated force, and achieving the desired joint torque under these conditions necessitates a change in force generated by the muscles on the opposing side of the joint. The implied result is increased co-contraction.

These features motivated the development of the second method previously presented for resolving muscle redundancy. The specific form of the cost function, basing it on the activations, was suggested by the observation that the activations in particular were far outside of their acceptable range. Also, the other functions scaling the muscle force, the force-length  $f(LC)$  and force-velocity  $g(u)$  functions, are inherently bounded at 1 and 1.5, respectively, while the muscle activations are not. To generate a force larger than  $1.5F_{max}$  requires that the activations be the source of this scaling. Focusing the solution of the control level (5.91) where the muscle redundancy is resolved on the activations led to the results presented next.

## **Results with Constrained Optimization Muscle Redundancy Resolution**

Using (5.93) to resolve muscle redundancy led to equally accurate tracking, as shown in Figure 35. However, the  $LS$  trajectories were significantly altered; see Figure 36. They all maintained lengths above the slack limit, a consequence of the lower bound on the activations. Even with this limitation, the tendon lengths all return to the region of their initial lengths once the motion trajectory is completed, indicating a reduction in force.

When checking the consistency between the synthetic controls and the control laws, Figure 37, it is seen that the torque recursion performs equally as well as in the least squares solution. The  $u$  and  $\psi_2$  do not compare as closely. A trend toward convergence is seen, however, with the exception of a brief transient at the peak, which remains bounded.

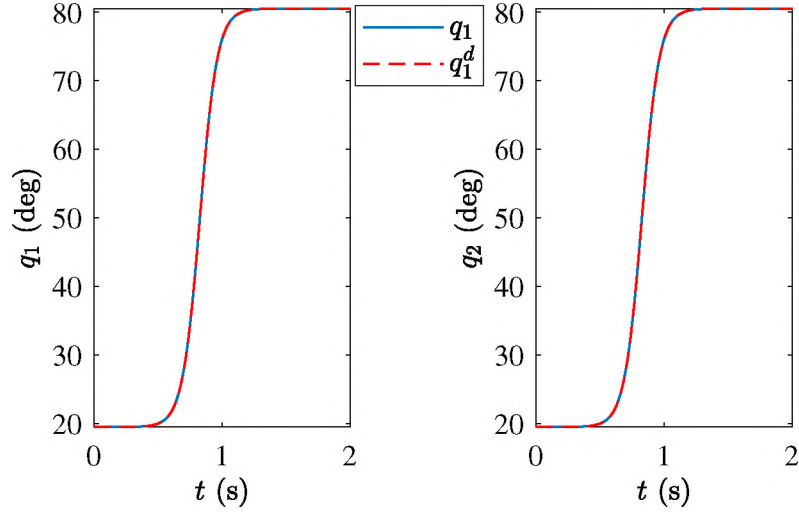


Figure 35: Constrained Optimization Solution: Both joints attain accurate tracking of a 0.65 second long 20-80 degree transition

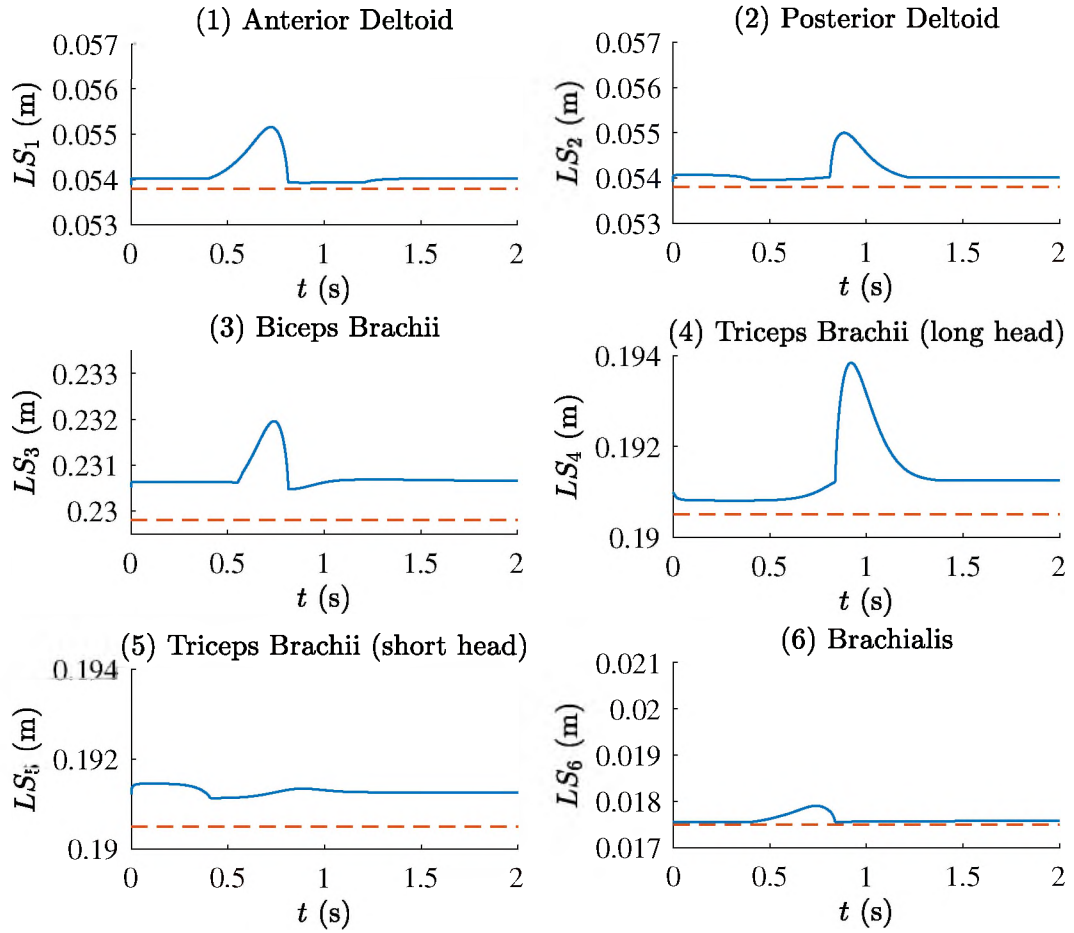


Figure 36: Constrained Optimization Solution: Tendon length states remain bounded. Red dashed lines show slack length limits  $L_{s,j}$

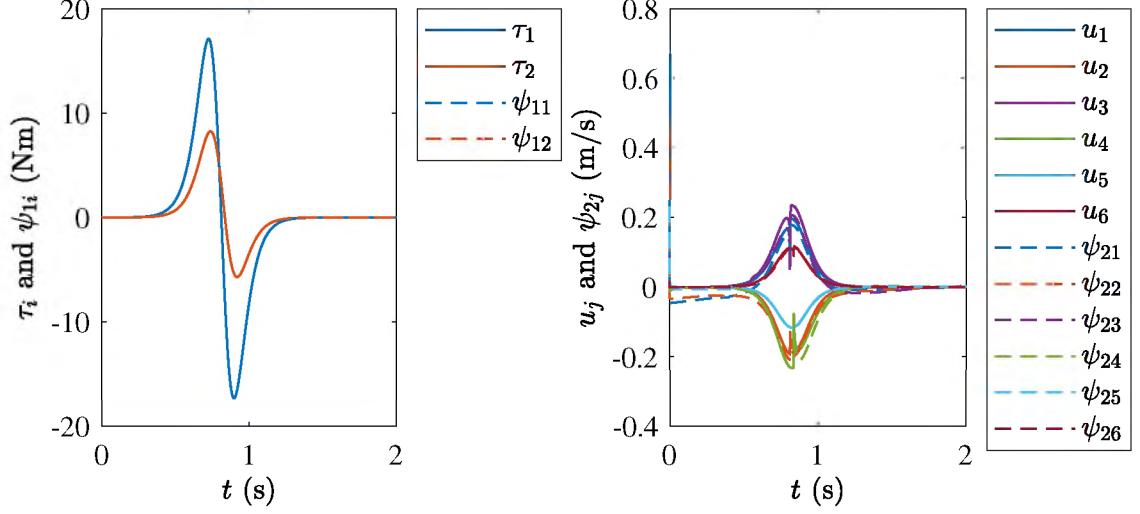


Figure 37: Constrained Optimization Solution: Synthetic control agreement for the first (left) and second (right) recursions

The constrained optimization method achieves reduced neural inputs and activations in comparison with the least squares method; these results are given in Figure 38. All signals meet the required range of zero to one with the exception of brief transients and negative segments in the neural inputs upon initialization and at the transition between the accelerating and decelerating actions of the muscles. It is noted that the activation signal estimates to which the constraints were actually applied strictly follow the constraints. Though not visible at this scale, the estimates are acceptable even where the actual activations negligibly break the lower constraint of 0.01, which led to feasibility of the optimization problem. Moreover, the negative regions of the neural inputs clearly correspond with steeply decreasing segments of the activations. It follows that the leading neural inputs must become negative to induce this steep response. Because there was no constraint placed on the controls, this behavior is not inconsistent with the backstepping controller. It does identify a limitation of this control technique, however.

The resulting muscle forces in Figure 39 are far closer to natural forces than those generated by the least squares solution. Also, looking at the simulation results of [48], the peak magnitudes are similar at just over 300 N. Because the trajectory was

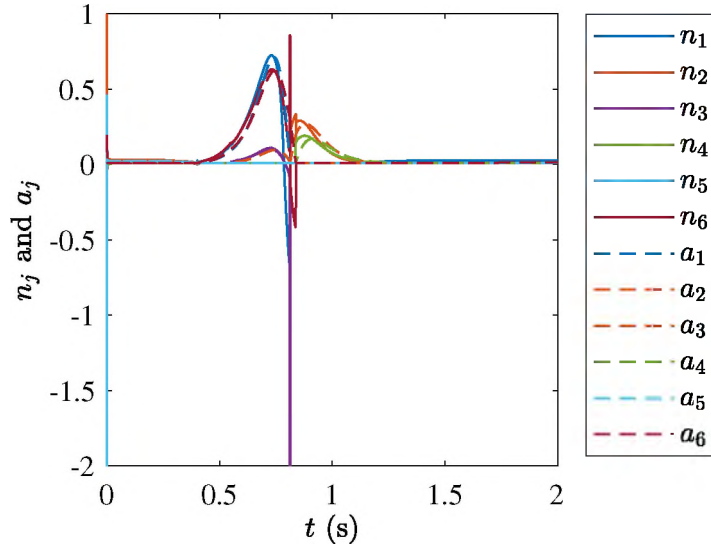


Figure 38: Constrained Optimization Solution: Control inputs  $n$  and associated activations  $a$ , showing the effects of the first order lag. Note that the largest initial transient extends to about  $-5.5$ , and the spike associated with  $n_3$  reaches approximately  $-3.1$

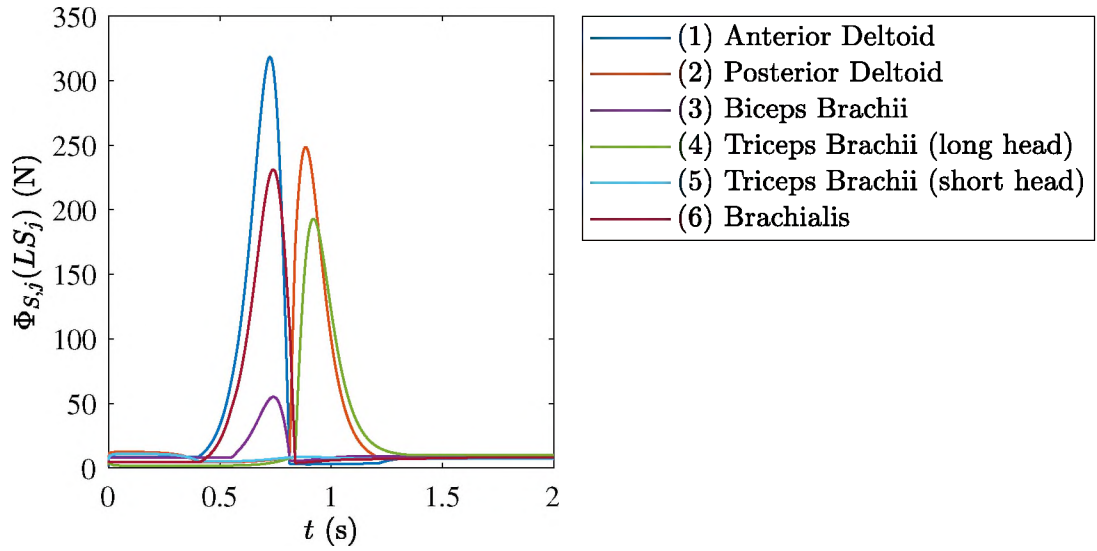


Figure 39: Constrained Optimization Solution: Forces generated by each muscle

specified as a setpoint change in that work, a direct comparison would not be accurate. However, two salient features of the force trajectories are consistent with [48]. First, the initial group of muscles to increase in force production are on the front side of the arm. This is followed by a counter increase in force by muscles on the back of the arm. This alternating activation pattern of the agonist and antagonist muscles also agrees with the human reaching experiments of [13]. Second, the Triceps Brachii (short head) generates little force [48].

#### 5.4.4 Discussion and Summary of Findings

Backstepping control of a general antagonistic muscle pair actuated robotic linkage was developed. Two methods of resolving muscle redundancy were identified. The application of both methods to a realistically scaled human arm for planar movements was demonstrated in simulation. The least squares method resulted in accurate tracking but unrealistic muscle co-contraction. The alternative, a constrained optimization, led to accurate tracking with more realistic muscle forces but revealed that the rate of change produced by the controller was aggressive.

Trajectories allowing more time for the motion or requiring a smaller displacement can help to improve control behavior under either method of resolving muscle redundancy. For the optimization method specifically, reducing the execution time for the motion results in muscle activation trajectories reaching their upper constraint. This case might or might not be feasible depending on whether a single-time step prediction is adequate to make the slope of the activations negative or zero (saturation) and maintain equality (5.91).

Detuning the controller was also attempted to smooth the changes in the control signal, seeking smoother activations and forces as a consequence. However, no combination was found that would keep the muscles within their working ranges. Alternatively, further constraints on the optimization were sought. Of particular interest

was the constraint based on the rate of change of the activation. It was constructed by observing the requirement

$$n = \frac{1}{\sigma(n)}\dot{a} + a \geq 0. \quad (5.103)$$

Taking the worst case scenario (smallest value of  $\sigma(n)$  occurs for large, negative  $n$ ), the approximate constraint  $\dot{a} > -24a$  was identified. No simulation trials where this constraint maintained feasibility were discovered, leading to the conclusion that a single-time step prediction is probably insufficient to solve (5.91) and meet these constraints for the given trajectory.

## 5.5 Remarks

The two muscle actuated mass simulation has provided insight into the agonist-antagonist relationship between muscle pairs. Human-like features such as cross-joint muscles have been implemented in the muscle-actuated linkage model combined with backstepping control framework. By application of this framework to a human arm, it was concluded that backstepping, while it provides the desired stability guarantees and successfully scales with the increased number of joints and muscles, is insufficient in its standard form. This is primarily because it does not inherently protect constraints required by the muscle actuators. An indirect means of introducing constraints was developed, but it would repeatedly find infeasible solutions depending on the constraints applied and the initial conditions for the simulation.

Considering the limitations of standard recursive backstepping, expanding upon this technique by use of barrier Lyapunov functions or constrained command filters could perhaps allow the appropriate constraints to be implemented analytically [125–127,153]. A shift to other control methods could also be considered. The innate ability of model predictive control (MPC) to protect constraints for a larger time horizon



than has been accomplished with backstepping alongside cost function optimization is particularly attractive. Alternatively, a combination of these control approaches, e.g. wrapping backstepping control with MPC to make backstepping the internal solver, might offer the benefits of both methods, internal stability guarantees and constraint protection [107].

In addition to addressing the aforementioned questions, future work could include the expansion of the system to consider non-constant moment arms. A study directly comparing the output of the system with human data could then be completed to better validate the human simulation. The method should then advance to machine interaction, which would likely require implementing an impedance controller through backstepping or an impedance cost function for MPC.

## CHAPTER VI

### OPEN LOOP MUSCLE-ACTUATED LINKAGE HUMAN SIMULATION

#### 6.1 Introduction

Within this chapter an open-loop approach to muscle-actuated linkage human simulation is taken. Maintaining the goals discussed in Chapter V, the work presented in this chapter can serve as an optimal control solver for (1) moving toward a receding horizon approach to closed-loop control such as MPC implementation or (2) open-loop studies of human-machine interaction systems. The solver combines two established methodologies, differential flatness and sum of squares (SOS) polynomials.

The concept of differential flatness was introduced in [28] and has been applied to a wide variety of systems. To state that a system is differentially flat is to say that a parameterization can be found such that the states and inputs of the system can be written in terms of some set of parameters, termed the flat outputs, and their derivatives; a system with  $m$  inputs must have  $m$  flat outputs. If such a parameterization can be found, the state and control trajectories can be determined algebraically from the flat outputs and their necessary derivatives, eliminating the use of differential equations.

A variety of systems have been identified as differentially flat. Several categories

include controllable linear systems, feedback-linearizable systems, and pure-feedback systems [76]. Notably, the musculoskeletal system dynamics discussed in Chapter V are in pure feedback form and should, therefore, have a flatness parameterization. However, existence of such a parameterization does not imply ease in determining the flat outputs. For the musculoskeletal system a flatness parameterization can be identified based on the physical system properties. The linkage joint coordinates define several of the flat outputs and the choice of remaining outputs is inspired by the significance of muscle co-contractions observed in Chapter V.

A SOS polynomial in multiple variables can be generally defined as

$$p(x) = \sum_{i=1}^n h_i^2(x), \quad (6.1)$$

where  $h_i(x)$  is a polynomial in variables  $x = [x_1, x_2 \dots x_m]$ . All SOS polynomials are non-negative. However, non-negative polynomials need not be SOS, and equivalence holds only for quadratic, univariate, and quartic polynomials in two variables [36, 94]. For this work the muscle co-contractions are functions of time. Because a muscle co-contraction, defined as the average tensile force of an agonist-antagonist muscle set, is univariate (in  $t$ ) and must be non-negative, SOS polynomials of sufficient degree can be used to define these functions without added conservatism.

Furthermore, the structure associated with SOS polynomials simplifies the solution of the polynomial coefficients because it transforms the problem into a semidefinite program, which is a convex optimization problem by definition. This transformation is accomplished for even (degree  $2d$ ) univariate polynomials by the SOS property that such a polynomial must be SOS if and only if a positive semidefinite matrix  $Q$  (Gram matrix) exists such that

$$p(x) = z_m^T Q z_m, \quad (6.2)$$

where  $z_m$  is a vector of monomials of degrees 0 to  $d$  [88]. Restating, for a general polynomial  $f(x)$  to be SOS, the semidefinite feasibility problem is to find some  $Q$  such that  $f(x)=z_m^T Q z_m$  and  $Q \geq 0$ . For a solution  $Q$  the SOS polynomial can be extracted by

$$p(x) = ||Lz_m||^2, \quad (6.3)$$

where  $Q = L^T L$ , the Cholesky factorization [88].

As previously outlined, a variety of methods have been developed to either emulate the human system given a set of kinematic data (inverse dynamics) or a set of kinetic data (forward dynamics). A related technique termed dynamic optimization combines both inverse and forward methods to generate fully predictive simulations, often from just minor kinematic guidance (e.g. periodicity of gait) [1, 2, 4, 108]. The solution of the muscle co-contraction flat outputs by SOS polynomial optimization can be termed a control allocation problem [49, 80]. Its combination with the subsequent evaluation of state trajectories from the flat outputs can be identified as a forward dynamics method constrained to a given trajectory [108]. Because of the flatness parameterization, though, the requirement of integrating state equations during forward dynamics is replaced by direct evaluation, reducing computation time relative to published methods [108]. Note that if the complete optimal control solver is wrapped with a trajectory optimization it is more closely associated with a dynamic optimization.

Therefore, by applying an unprecedented parameterization of the musculoskeletal system dynamics based on differential flatness and SOS polynomials, the optimal control solver achieves analytical and computational benefits; this parameterization is being published in [102]. Continuing the work of [102], which focuses on tracking, it is shown that the method can handle interaction forces. The solver is validated by comparing its resultant muscle activations with experimental electromyography (EMG) data. The solver is then applied to the problem of optimal exercise of se-

lected muscles with the planar arm model. This application shows that the solver is capable of isolating single muscles, even with the emphasis on muscle co-contractions, is highly efficient, and can be effectively combined with an outside method for constraint management.

## 6.2 Differential Flatness of Musculoskeletal Systems

Recall the musculoskeletal system dynamics of Chapter V; both the dynamics of the two muscle actuated mass system and the muscle actuated linkage can be summarized by the formulation

$$M(q)\ddot{q} + C(q, \dot{q})\dot{q} + g(q) = A\Phi_S(LS) \quad (6.4)$$

$$\dot{LS} = -A^T\dot{q} + u \quad (6.5)$$

$$\dot{a}_j = \sigma_j(n_j)(n_j - a_j), \quad (6.6)$$

where  $u_j = g_j^{-1}(z_j)$  with

$$z_j = \frac{\Phi_{S,j}(LS_j) - \Phi_{P,j}(L_j(q) - LS_j)}{a_j f_j(L_j(q) - LS_j) F_{max,j}} \quad (6.7)$$

and  $A$  denoting the matrix of moment arms such that  $A(i, j) = d_{ij}$ , where the  $d_{ij}$  are constants as in (5.70) with  $i = 1, 2, \dots, \mathbb{I}$  and  $j = 1, 2, \dots, \mathbb{J}$ .

As previously identified, this pure feedback system should have a differential flatness parameterization. For a total of  $\mathbb{J}$  control inputs, one associated with each muscle,  $\mathbb{J}$  flat outputs must be determined. Beginning with the standard choice of flat outputs for robotics, the joint coordinates  $q$  are selected [76]. This leaves  $p = \mathbb{J} - \mathbb{I}$  additional flat outputs to be chosen. Assuming that there is at least one redundant muscle being modeled ( $p \geq 1$ ), the remaining flat outputs are proposed to be the

muscle co-contractions

$$Y = E\Phi_S(LS), \quad (6.8)$$

where  $E$  is defined as a  $p \times \mathbb{J}$  matrix that results in computing co-contractions of antagonistic muscle pairs. The row sums of  $E$  are each assumed to equal 1. The completed set of flat outputs is then

$$y = \begin{bmatrix} q \\ Y \end{bmatrix}. \quad (6.9)$$

This implies that

$$\begin{bmatrix} \tau(y, \dot{y}, \ddot{y}) \\ Y \end{bmatrix} = \begin{bmatrix} A \\ E \end{bmatrix} \Phi_S(LS) = C\Phi_S(LS), \quad (6.10)$$

where  $\tau$  represents the left-hand side of (6.4). Under the circumstance that  $p > \mathbb{J}/2$ , additional flat outputs are assigned some linear combination of the tendon forces such that  $C$  remains invertible. By making this assumption, the states  $LS$  can be computed from a set of flat outputs as long as the tendons are outside of the slack region, allowing  $\Phi_S(LS)$  to be inverted.

Having shown that the joint coordinates and tendon lengths can be recovered from the flatness parameterization, only the activation states and control inputs  $n$  remain. State derivative  $\dot{LS}$  can be determined by taking the time derivative of the inversion of (6.10)

$$\dot{LS}_j = \frac{1}{\Phi'_j(LS_j)} c_j \begin{bmatrix} \dot{\tau} \\ Y \end{bmatrix}, \quad (6.11)$$

where  $c_j$  is the  $j$ -th row of  $C$  and  $\dot{\tau}$  can be computed from the joint coordinate flat outputs and their derivatives. The  $u_j$  can now be determined from (6.5). After finding  $z_j$  from the definition  $z_j = g_j(u_j)$ , each activation state  $a_j$  can be found from (6.7).

The control inputs result from differentiating  $a_j$  with respect to time and solving (6.6).

The proposed flat outputs are not unique [76]. Indeed, if the same control inputs can be computed from a different set of flat outputs, the choice of flat outputs themselves does not affect the resulting algebraically evaluated state trajectories as they are always equivalent to solving the system's differential equations. Assuming that another set of flat outputs can be found, a method of describing them, such as the SOS polynomials being used here, would need to be determined to fit the circumstances.

### 6.2.1 Example: Differential Flatness of Antagonistic Muscle Pair Actuated Mass System

Revisiting the simple system of Section 5.3 where two opposing muscles are used to drive a central mass to track desired trajectories, the flatness parameterization can be easily exhibited. For this system  $\mathbb{I} = 1$  and  $\mathbb{J} = 2$ , resulting in  $p = 1$ . This model simplifies the system dynamics (6.4) through (6.7) with  $M = 1$ ,  $C = 0$ ,  $g = 0$ , and  $A = [-1 \ 1]$ . Also recall that the constant length constraint induced by mounting the system between two walls further simplifies the system and allows the definition of the  $LC$  and  $u$  directly from  $L_1$  and the  $LS$  and their derivatives.

The two muscles have one input each, implying a total of two flat outputs to be defined. The first flat output is chosen as the coordinate locating the mass  $y_1 = q$ . The second is the average of the tendon forces  $y_2 = Y = \frac{1}{2}(\Phi_S(LS_1) + \Phi_S(LS_2))$ , giving  $E = [\frac{1}{2} \ \frac{1}{2}]$ . Note that the resulting  $C$  can be inverted. Defining all states in

terms of the flat outputs and their derivatives, the full parameterization is

$$\begin{aligned}
q &= y_1 \\
\dot{q} &= \dot{y}_1 \\
LS_1 &= \Phi_S^{-1} \left( y_2 - \frac{M}{2} \ddot{y}_1 \right) \\
LS_2 &= \Phi_S^{-1} \left( y_2 + \frac{M}{2} \ddot{y}_1 \right) \\
a_1 &= \frac{\Phi_S \left( y_2 - \frac{M}{2} \ddot{y}_1 \right) - \Phi_P(L - LS_1)}{f(L - LS_1)g(u_1)F_{max}} \\
a_2 &= \frac{\Phi_S \left( y_2 + \frac{M}{2} \ddot{y}_1 \right) - \Phi_P(L - LS_2)}{f(L - LS_2)g(u_2)F_{max}} \\
n_1 &= n_1(a_1, \dot{a}_1) \\
n_2 &= n_2(a_2, \dot{a}_2)
\end{aligned} \tag{6.12}$$

From the simple example of a two-muscle actuated mass it can be noted that the co-contraction required to perform any trajectory  $q(t)$  compatible with the system limits is arbitrary. This is consistent with the freedom allowed by redundant actuation. Accordingly, an optimization approach to selecting the muscle co-contractions is recommended.

### 6.3 Sum of Squares Representation of Muscle Co-contractions

Human motion studies frequently minimize a measure of muscle effort, a proxy for energy usage, to resolve muscle redundancy [1]. It is proposed that minimizing muscle co-contractions subject to task constraints conforms to this goal, as excessive co-contraction does not conserve energy. SOS polynomial methods can effectively parameterize and solve for minimal co-contraction trajectories. Consequently, the integral of the co-contractions is used to represent the muscle effort.

SOS polynomial solutions can also be subjected to constraints. Two main categories of constraints are of interest when working with the muscle co-contractions.



First, boundary conditions might need to be implemented through equality constraints. For example, in a receding horizon control application of the solver, repeated predictions would require initial condition constraints to enforce continuous predicated trajectories as the optimization recedes. Terminal constraints could also be important in this circumstance. An open-loop application, such as the optimal exercise problem that will be examined, could also have boundary conditions that need to be enforced, periodicity being of particular interest in the provided example. Second, inequality constraints must be defined to prevent muscle slack. To avoid muscle slack throughout a given movement requires that the tendon forces are maintained at or greater than some set of force reserves  $\underline{F}_T$ , explicitly  $\Phi_S(LS) \geq \underline{F}_T$  for some positive vector  $\underline{F}_T$ . In order to implement this inequality, consider that  $\Phi_S(LS)$  can be expanded as follows

$$\Phi_S(LS) = C^{-1} \begin{bmatrix} \tau(y, \dot{y}, \ddot{y}) \\ Y \end{bmatrix} = C_\tau \tau + C_Y Y, \quad (6.13)$$

but because  $\tau(y, \dot{y}, \ddot{y})$  is not a polynomial in general, a polynomial inequality cannot be applied directly to this expression. Circumventing this problem, bounds on the  $\tau$  can be computed from the previously identified joint trajectories and can be combined with the tendon force reserves  $\underline{F}_T$  giving the following vectorial SOS inequality

$$C_Y Y \geq \underline{F}_T - \min_t C_Y \tau(t) = B. \quad (6.14)$$

Alternatively, a potentially less conservative method could be used by finding the elements of  $B$  from

$$\begin{aligned} B_j &= \underline{F}_T - \min c_j \tau \\ \tau &\geq \underline{\tau} \\ -\tau &\geq -\bar{\tau}, \end{aligned} \quad (6.15)$$

which is a linear program in the two-element decision variable  $\tau$  where  $c_j$  is the  $j$ -th row of  $C_Y$  and  $\underline{\tau}$  and  $\bar{\tau}$  are the lower and upper bounds on  $\tau(t)$ , respectively, for given joint trajectories.

In general, the SOS polynomial optimization problem for muscle co-contractions can be summarized as

$$\begin{aligned} \min_{Y} \quad & \int_0^T \sum_{i=1}^p Y_i(t) dt \\ \text{subject to} \quad & Y(t) \text{ is SOS} \\ & \text{initial and terminal conditions on } Y, \dot{Y}, \text{ and } \ddot{Y} \\ & C_Y Y(t) \geq B \end{aligned} \tag{6.16}$$

The solution of (6.16) requires symbolic conversion to a semidefinite program, as previously described. The Matlab sum of squares polynomial optimization toolbox SOSTOOLS is one accessible means of performing this transformation. It also provides for the solution of the resulting semidefinite program by a variety of solvers; for example, the default solver is SeDuMi [92]. Alternatively, because the SOS problem is convex, if the cost function and constraints are affine in the decision variables, it can be simplified further to a linear program, eliminating the computational burden of the symbolic processing [8]. An example of this simplification and its computational benefits will be provided in the context of an exercise application. Solution of a linear program can be completed with the Matlab optimization toolbox routine `linprog`, among other options.

### 6.3.1 Including Interaction Forces

To implement environmental interaction forces, the system model (6.4) can be updated as follows

$$M(q)\ddot{q} + C(q, \dot{q})\dot{q} + g(q) - J(q)^T F_{ext} = A\Phi_S(LS), \quad (6.17)$$

where  $J$  is the velocity Jacobian and  $F_{ext}$  is the vector of forces applied at the “end effector” of the human linkage, for example at the wrist in a two degree of freedom arm model. From this model description it can be seen that the flatness parameterization is maintained. It is then straightforward to extend the SOS solver to account for the external forces, assuming they are known, because they simply appear as an additive term in  $\tau(t)$ , updating the tendon force inequality on  $C_Y Y$ . The assumption that the force trajectories  $F_{ext}(t)$  are known is feasible if they are purely a function of the system kinematics, which have also been assumed given. This is equivalent to saying that the human can track while compensating for these forces. Interesting cases where this assumption can hold include simulated interaction with an impedance-controlled machine, which will be further considered, and typical ground contact models for gait [1].

## 6.4 Validating the Open Loop Solver

While the formulation of the open loop solver is analytically favorable, it is of no use if it does not represent the actual human system. Therefore, the model must be validated against human data. Reference [70] presents a study of the human arm performing planar motions. Tracing actions that are perpendicular to, at a right slant to, parallel to, and at a left slant to the sagittal plane are considered. When superimposed, these actions form a star pattern with the wrist starting each action from the center of the star. A peak-to-peak amplitude of 18 cm was prescribed for

each trajectory. The central point is positioned in line with the shoulder and 40 cm away. These motions are performed at a rate of 2.1 Hz, indicating that the dynamics of the arm should be thoroughly excited. For each action the muscle activity is measured by EMG for the Anterior Deltoid, Posterior Deltoid, Biceps Brachii and Triceps Brachii (short head). Because the EMG signals are not scaled to a maximal contraction, only a qualitative comparison to phase and relative magnitudes can be made with the optimal control solver's resulting muscle activations.

To apply the optimal control solver, trajectories were a collapsed ellipse with the minor axis assigned a value of 5e-3 m, giving the “line” an overall width of 1 mm. This is representative of the accuracy of the human movement. In addition, no external forces were applied to the arm end effector. The co-contraction SOS polynomial was specified as a quartic with periodicity constraints on  $t \in [0 \ T]$ , which can be solved using a linear program; see Section 6.5.3 for details. All tendon force reserves were set to the same value;  $\underline{F}_T = 20$  N, which is less than 3% of the maximum isometric force  $F_{max}$  of each muscle modeled. The co-contraction matrix  $E$  for six muscles (columns) and four flat outputs (rows) was chosen as

$$E = \begin{bmatrix} \frac{1}{2} & \frac{1}{2} & 0 & 0 & 0 & 0 \\ 0 & 0 & \frac{1}{2} & \frac{1}{2} & 0 & 0 \\ 0 & 0 & 0 & 0 & \frac{1}{2} & \frac{1}{2} \\ \frac{1}{3} & 0 & \frac{1}{3} & 0 & \frac{1}{3} & 0 \end{bmatrix}. \quad (6.18)$$

The first three rows compute the force averages for each antagonistic muscle pair. While any arbitrary selection maintaining the row sum assumption and matrix  $C$ 's invertibility could be made for the last row, it does affect the distribution of required effort among the muscle groups formed by the previous three rows. For example, choosing the first element of the final row as one and assigning zeros to the remaining elements can eliminate recruitment of the first pair of muscles (Anterior and Posterior

Trajectory	Solver Time (s)
Vertical	0.01453 $\pm$ 0.002680
Right Diagonal	0.01179 $\pm$ 0.001034
Horizontal	0.02627 $\pm$ 0.003856
Left Diagonal	0.03471 $\pm$ 0.001459

Table VII: Average and one standard deviation over five trials of the time required for the solver to complete the validation problem

Deltoids). Accordingly, the final row chosen here weighs all muscle pairs equally. Alternative weights meeting the assumptions could be used throughout the matrix. For instance, muscle recruitment should be able to be shifted toward or away from emphasizing the biarticular muscles. Further study is required to fully understand how the selection of the elements of  $E$  affects the results.

For all cases the Cartesian trajectories and associated tangential accelerations were accurately replicated. The time required by the linear programming solver is reported in Table VII for each trajectory. Though all cases required little time to complete, the variation in time is indicative of how the solution of some trajectories can be more difficult than others. Analysis will focus on comparing the simulated muscle activations to measured EMG. While only one cycle was solved due to the periodicity of the trajectory, a total of five cycles are replicated in the plots for comparison to the data presented in [70].

Figure 40 presents the results computed for the vertical trajectory. Reference [70] shows alternating bursts of Anterior and Posterior Deltoid activity with a small amount of Biceps activation that occurs slightly ahead of the Anterior Deltoid bursts. The Triceps appears to be inactive. Comparing to the open loop solver, the same alternation between the Deltoids can be seen. The Biceps show minor activation and the Triceps little at all. The phase of the Biceps is closer to the Posterior Deltoid in the simulated case.

The reported data of [70] for the right diagonal trajectory shows decreased activity of both Deltoid muscles. The Anterior Deltoid shows a more constant activation

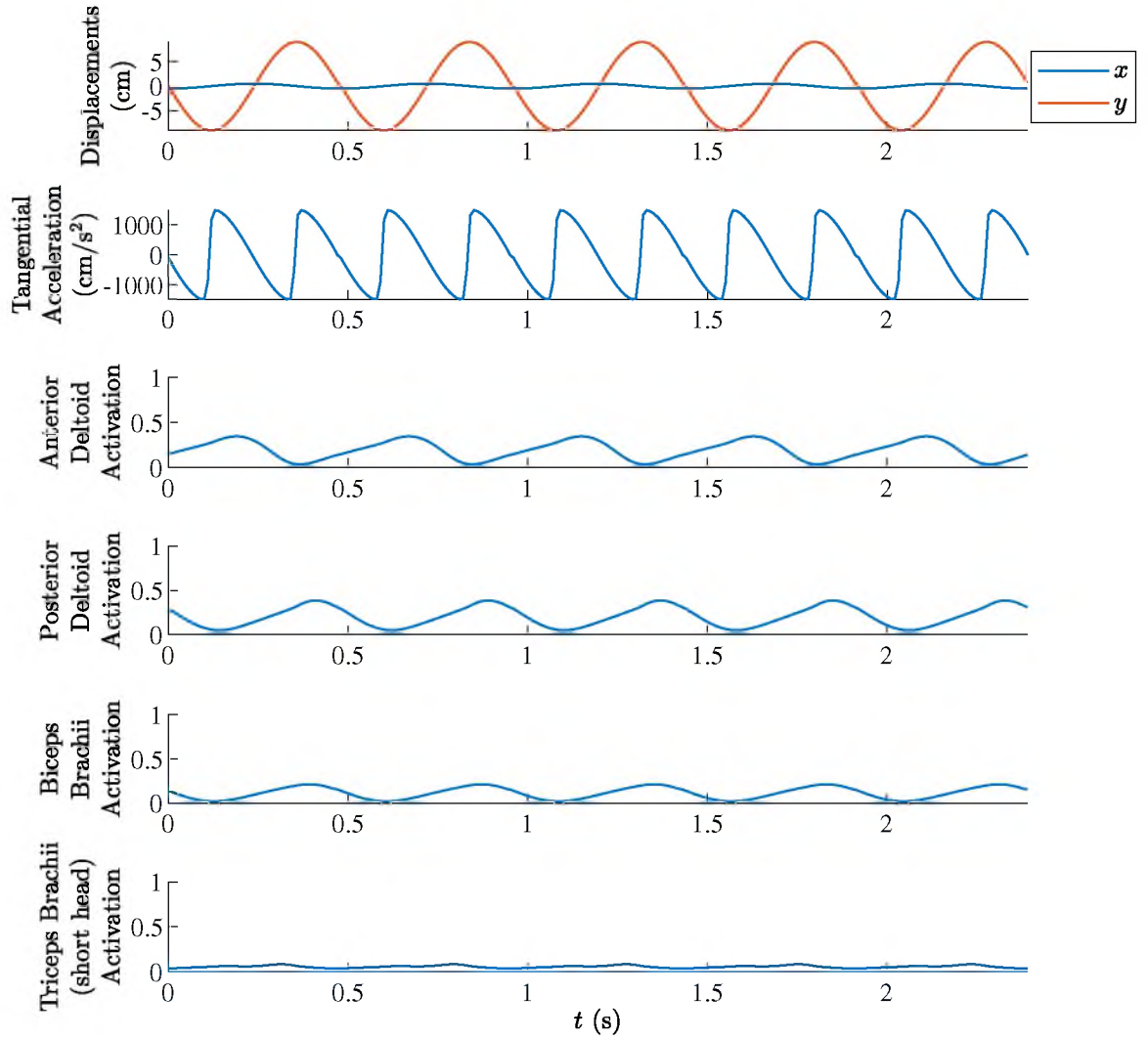


Figure 40: Cartesian trajectories, tangential accelerations, and muscle activations generated by the optimal control solver for a trajectory approximating the vertical (planar but perpendicular to the sagittal plane) trajectory reported in [70]

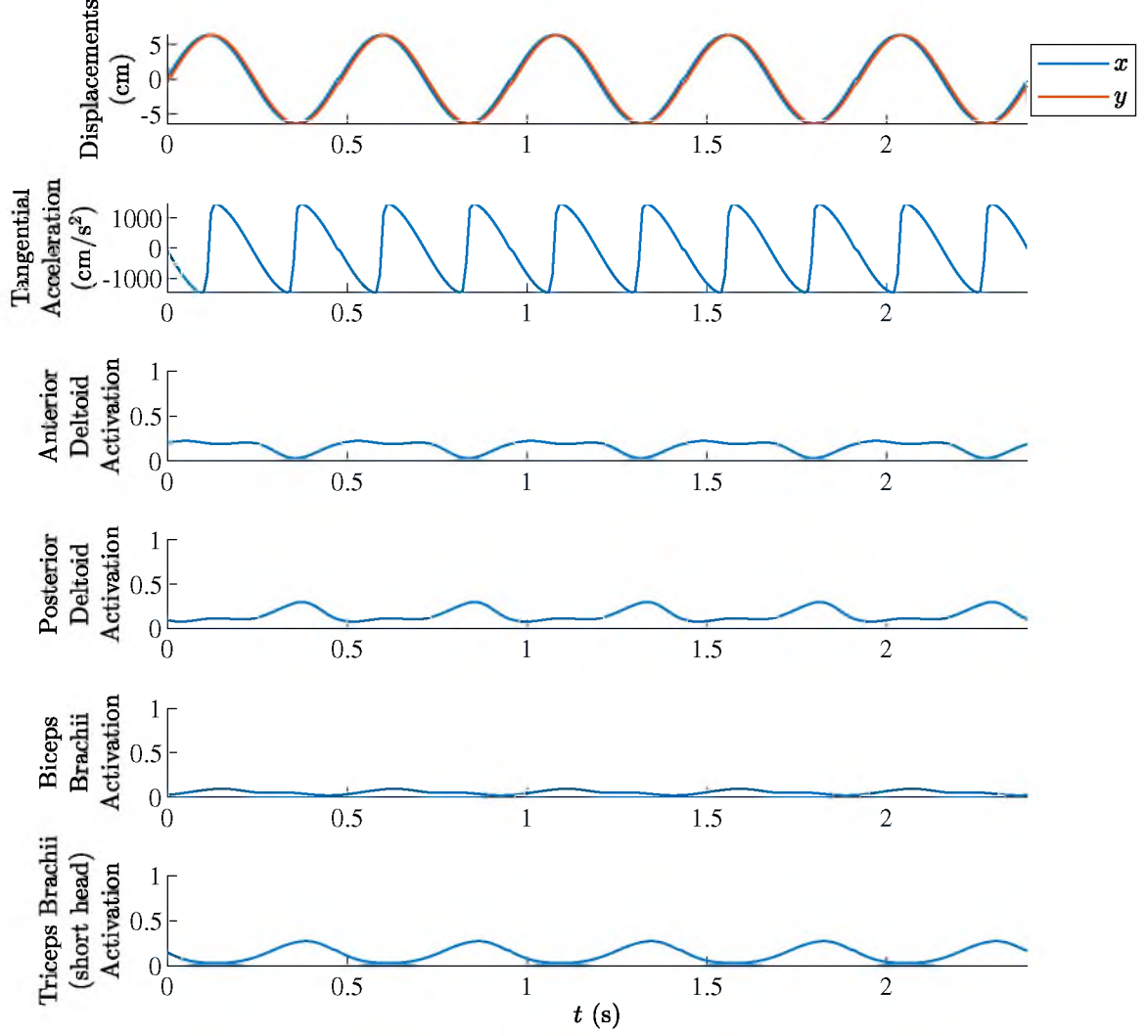


Figure 41: Cartesian trajectories, tangential accelerations, and muscle activations generated by the optimal control solver for a trajectory approximating the right diagonal trajectory reported in [70]

pattern while the Posterior Deltoid exhibits brief bursts. The Biceps and Triceps display an alternating behavior with comparable magnitudes to each other where the Biceps leads the Triceps, causing some overlap. The performance of the simulated muscles generally matches the recorded data in this case; see Figure 41. The primary difference, once again, is in the phase of the Biceps, which is farther behind the Triceps for the simulated case than it is for the measured case.

Continuing to the horizontal trajectory, [70] identifies a strong alternation between the Anterior and Posterior Deltoids and a limited in magnitude but clearly patterned

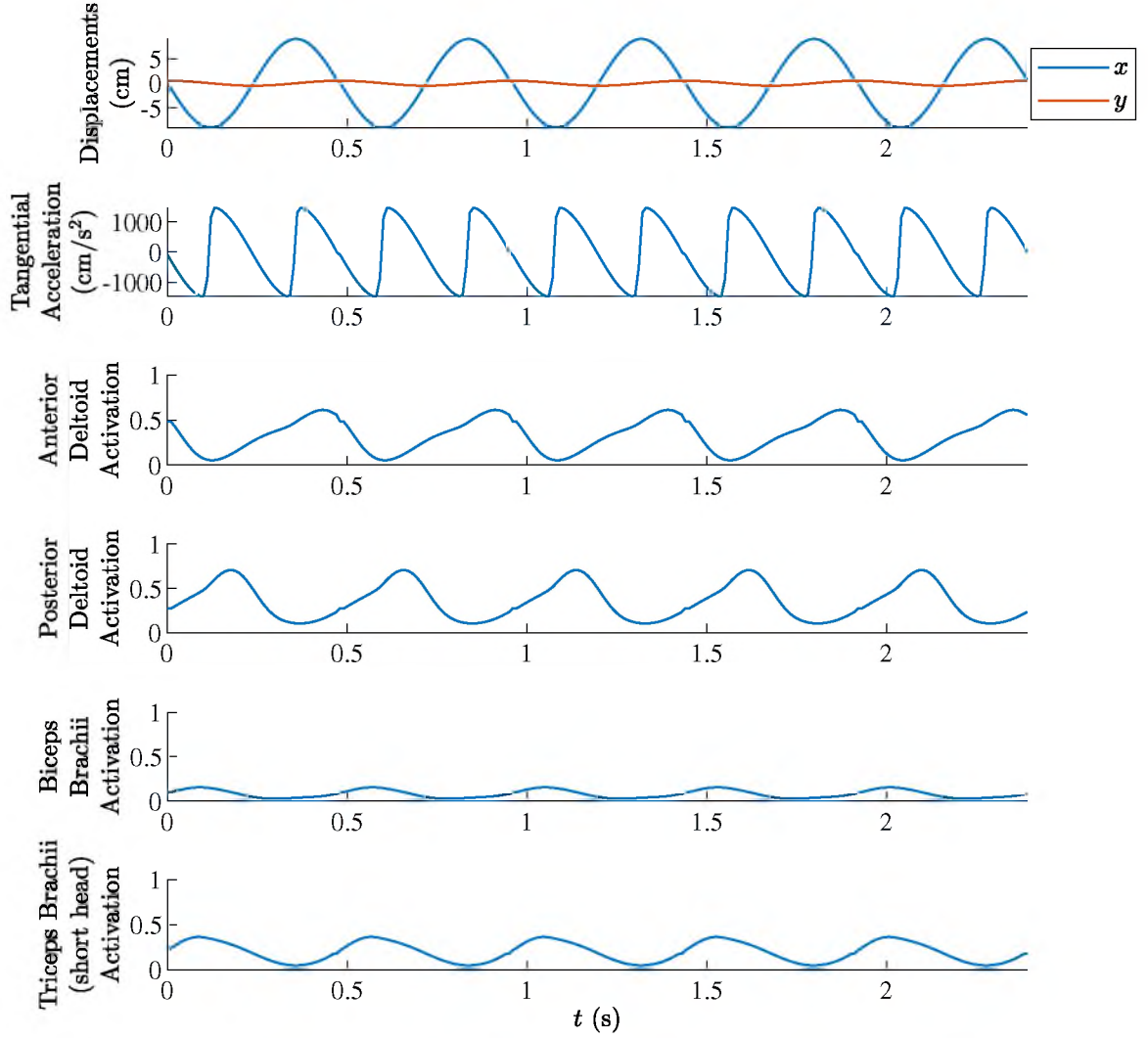


Figure 42: Cartesian trajectories, tangential accelerations, and muscle activations generated by the optimal control solver for a trajectory approximating the horizontal trajectory reported in [70]

Biceps activity that trades off with the Triceps, which demonstrate a magnitude of about double that of the Biceps. With exception of the Biceps' phase, the simulated results reported in Figure 42 match these patterns.

The left diagonal trajectory EMG signals of [70] are similar to the horizontal case except that there appears to be no Triceps activity for this action and the magnitudes of the Anterior and Posterior Deltoids are higher. A simulation of this case presents these major features, except that the Triceps are more active than expected and the Biceps phase remains a concern; see Figure 43.



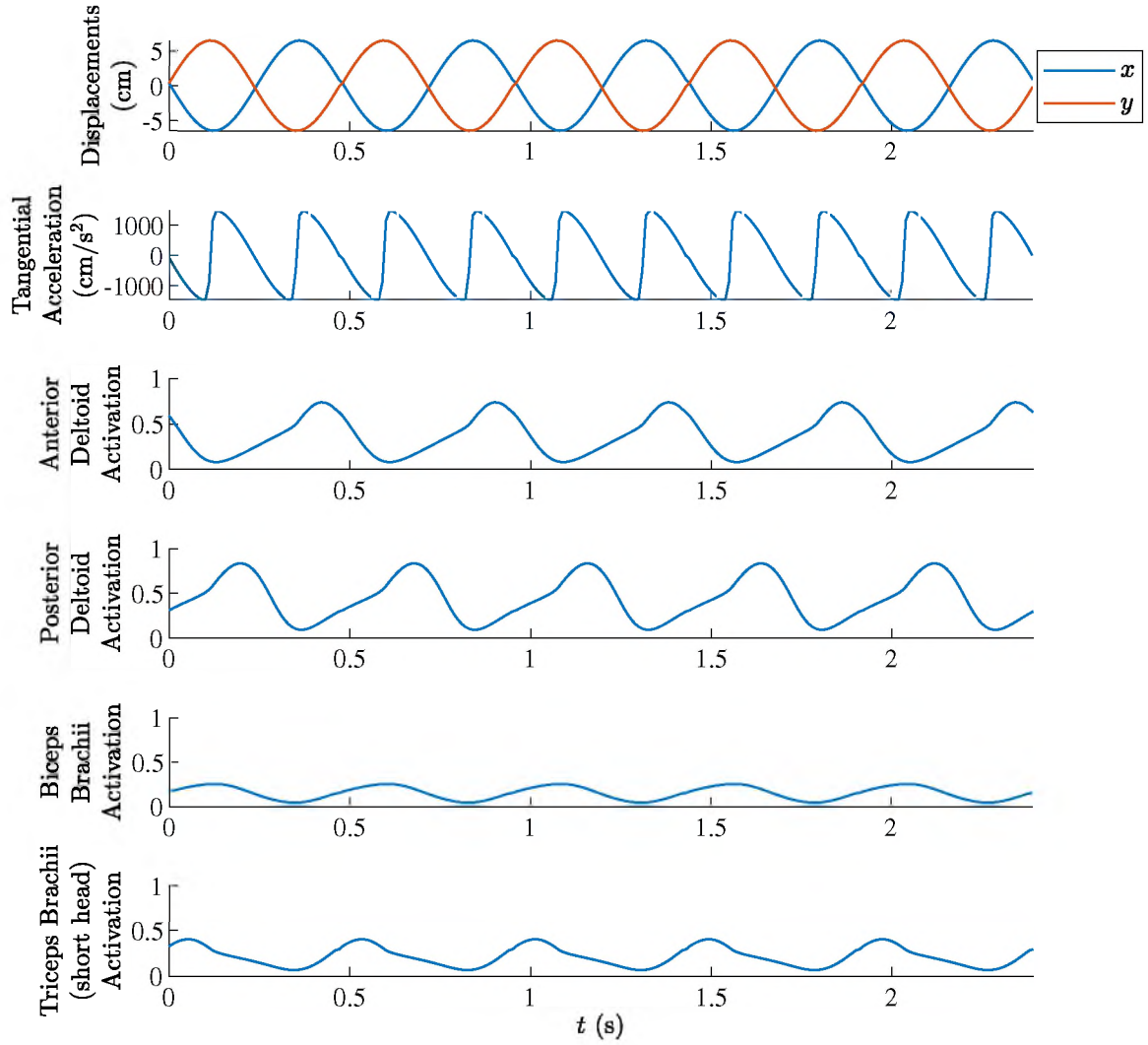


Figure 43: Cartesian trajectories, tangential accelerations, and muscle activations generated by the optimal control solver for a trajectory approximating the left diagonal trajectory reported in [70]

Approximately 70% of the identified features of the EMG data are also represented in the simulated model. The primary discrepancy is in the phase of the Biceps Brachii. With the current information it is difficult to determine whether the model or the data is the source of this inconsistency. For example, it is possible that the EMG data involved some crosstalk, which could skew the data from a particular muscle. Execution of a similar protocol where information about the absolute scaling of the EMG signal relative to maximal contractions, analysis of potential crosstalk, and measurements across a broader variety of trajectories are implemented would allow for an improved validation study.

## 6.5 Application to Optimal Exercise

To illustrate an open-loop application of the solver and gain understanding of the solver's behavior, the problem of optimal exercise will be examined. This application is motivated by the pursuit of advanced exercise machines. For example, extremum seeking control and similar methods are being developed to maximize the impact of an exercise session [71, 72, 90]. The results determined here could be used to provide an initial condition for extremum seeking control or if the necessary feedback signals are not available for extremum seeking control (e.g. EMG), generate exercise protocols that should better inform the muscle strengthening process.

The optimal exercise problem is formulated in the context of a planar arm in contact with an idealized exercise machine capable of applying specified forces to the human arm endpoint. Trajectories for the arm and force profiles for the machine are optimized such that selected muscles' activations are maximized. Note that the opposite question (minimizing usage of a particular muscle or group of muscles) could be addressed in the same manner for a rehabilitation protocol.

In applying the solver to the optimal exercise problem, three features should confirm the solver design. First, effective exercises should be able to be found for

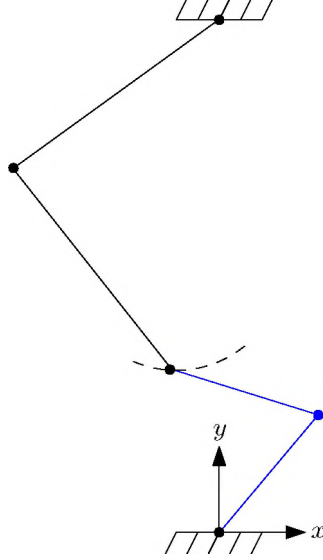


Figure 44: Example of an exercise machine (black) and human arm (blue) joined by a revolute joint and tracing the same trajectory (dashed) in the horizontal plane. The shoulder is located at the origin

every muscle, indicating that the solver's use of co-contractions does not prevent the muscles' independent action. Second, the results should show that an external method for maintaining the muscle constraints is sufficient while remaining timely. Third, the solver should run quickly in comparison to established methods, further supporting the second feature.

### 6.5.1 Exercise Machine and Human Arm Interaction Model

The human arm model presented in Section 5.4.3 is reused here. It is connected by a revolute joint to an exercise machine linkage located opposite it. This arrangement is shown in Figure 44. It is assumed that the exercise machine only generates the external force applied to the arm and does not contribute any other dynamics to the model. Because the method used to determine the external force only requires kinematic analysis of the exercise machine, the machine can briefly be described as being a planar two degree of freedom linkage located 1 m along the positive  $y$ -axis from the arm and composed of two 0.5 m links.

The external force applied to the arm endpoint is generated by a Cartesian impedance controller for the endpoint of the exercise machine. This allows for various combinations of inertia, damping, and stiffness properties to be applied to the arm endpoint. This can be expressed as

$$\begin{bmatrix} I_x & 0 \\ 0 & I_y \end{bmatrix} \begin{bmatrix} \ddot{\tilde{x}} \\ \ddot{\tilde{y}} \end{bmatrix} + \begin{bmatrix} B_x & 0 \\ 0 & B_y \end{bmatrix} \begin{bmatrix} \dot{\tilde{x}} \\ \dot{\tilde{y}} \end{bmatrix} + \begin{bmatrix} K_x & 0 \\ 0 & K_y \end{bmatrix} \begin{bmatrix} \tilde{x} \\ \tilde{y} \end{bmatrix} = -F_{ext}, \quad (6.19)$$

where  $I_x$  and  $I_y$  are the inertia,  $B_x$  and  $B_y$  are the damping, and  $K_x$  and  $K_y$  are the stiffness properties applied to displacements in the  $x$  and  $y$  directions, respectively. Displacements are defined using the convention  $\tilde{x} = x_a - x_d$ , where subscript  $a$  identifies the actual trajectory of the machine endpoint as it is guided by the arm and subscript  $d$  identifies the desired trajectory of the machine endpoint.  $F_{ext}$  is the force applied to the human arm endpoint, assuming perfect tracking by the human.

From a practical standpoint, it is noted that scaling the inertia, damping, and stiffness terms by some value  $S$  scales  $F_{ext}$  by the same amount, which is equivalent to scaling  $F_{ext}$  while maintaining the natural frequency  $\omega_n$  and damping ratio  $\zeta$  of the selected impedance. For a given set of joint trajectories the same scaling passes directly to the joint torques,  $\tau = J^T(q)F_{ext}$ . While the scaling factor  $S$  is not replicated exactly in the muscles, it does have a direct relationship to the muscle forces. Accordingly, recommended practice is to determine an impedance and trajectory combination that maximizes the effort of a muscle of interest and then scale it down as needed.

### 6.5.2 Trajectory Generation

Two task space trajectories need to be generated for the exercise simulation. The first trajectory is the desired trajectory for the machine. This is the trajectory that it will gravitate toward. The second trajectory is the actual trajectory that

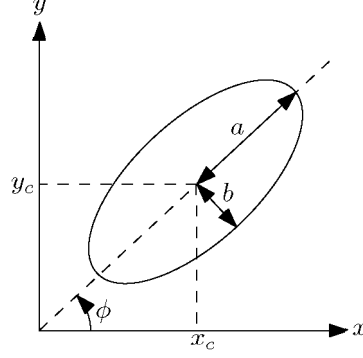


Figure 45: General ellipse trajectory in task space with axes  $a$  and  $b$ , center point  $(x_c, y_c)$ , and orientation  $\phi$

the machine and arm endpoints trace under the volition of the human arm. Both of these trajectories are defined as general ellipses; see Figure 45. From a symbolic form of these trajectories symbolic equations for the joint angles, velocities, and accelerations were determined for each linkage by inverse kinematics [114] and could then be evaluated.

### 6.5.3 SOS Solution Reduced to a Linear Program

Due to the periodicity constraints associated with the elliptical trajectory, periodicity can be extended to the muscle co-contractions. These conditions allow a linear program to be developed to solve for the SOS polynomials representing the muscle co-contractions. To enforce periodicity up to the second derivative of all co-contraction polynomials  $Y$  on  $t \in [0, T]$ , the following constraints are required for each polynomial  $i$

$$\begin{aligned} y_i(0) &= y_i(T) \\ \dot{y}_i(0) &= \dot{y}_i(T) \\ \ddot{y}_i(0) &= \ddot{y}_i(T). \end{aligned} \tag{6.20}$$

These constraints specify that at minimum a cubic polynomial be used to enforce them and maintain one decision variable (polynomial coefficient) for optimization. However, as an odd degree polynomial a cubic cannot be non-negative, and, therefore,

as a univariate polynomial cannot be a SOS. This implies that at least a quartic polynomial must be used. Its general form can be written for polynomial  $i$  as

$$y_i(t) = \alpha_{i0} + \alpha_{i1}t + \alpha_{i2}t^2 + \alpha_{i3}t^3 + \alpha_{i4}t^4. \quad (6.21)$$

Applying periodicity constraints (6.20) results in

$$\begin{aligned} \alpha_{i1} &= 0 \\ \alpha_{i2} &= T^2\alpha_{i4} \\ \alpha_{i3} &= -2T\alpha_{i4}, \end{aligned} \quad (6.22)$$

giving the reduced polynomial

$$y_i(t) = \alpha_{i0} + T^2\alpha_{i4}t^2 - 2T\alpha_{i4}t^3 + \alpha_{i4}t^4 \quad (6.23)$$

in the two decision variables  $\alpha_{i0}$  and  $\alpha_{i4}$ . Note that for an even degree polynomial the leading term determines whether the polynomial opens upward or downward. To enforce non-negativity, it is necessary that the quartic polynomial open upward. In addition, all extreme values must be non-negative. A total of three local optima can be solved from  $\dot{y}_i = 0$ . They occur at  $t = 0$ ,  $\frac{T}{2}$  and  $T$ . Function values at  $t = 0$  and  $T$  show that  $\alpha_{i0}$ , the  $y$ -intercept, must be non-negative. At  $\frac{T}{2}$  the condition

$$\alpha_{i0} + \frac{1}{16}T^4\alpha_{i4} \geq 0 \quad (6.24)$$

is necessary. The conditions on polynomial expression  $C_Y Y(t) - B \geq 0$  can be worked out in the same way. Completing the linear program, the integral cost function for an individual polynomial is

$$\int_0^T y_i(t)dt = T\alpha_{i0} + \frac{1}{30}T^5\alpha_{i4}. \quad (6.25)$$

The complete program can be assembled as

$$\min \sum_{i=1}^p T\alpha_{i0} + \frac{1}{30}T^5\alpha_{i4} \quad (6.26)$$

$$\text{subject to} \quad -\alpha_0 \leq 0 \quad (6.27)$$

$$-\alpha_4 \leq 0 \quad (6.28)$$

$$-\alpha_0 - \frac{1}{16}T^4\alpha_4 \leq 0 \quad (6.29)$$

$$-C_Y\alpha_0 + B \leq 0 \quad (6.30)$$

$$-C_Y\alpha_4 \leq 0 \quad (6.31)$$

$$-C_Y\alpha_0 - \frac{1}{16}T^4C_Y\alpha_4 \leq 0. \quad (6.32)$$

This structure allows for the efficient solution of the muscle co-contractions associated with tracking a known trajectory with known environmental forces; in the example case the forces result from an impedance controller.

#### 6.5.4 Trajectory and Impedance Optimization

To find an optimal trajectory and set of impedance parameters maximizing specified muscle activations, a global optimizer termed biogeography-based optimization (BBO) is used. The algorithm in general, applicable problem constraints, and parameter search space are described next.

#### Constrained Biogeography-Based Optimization

Biogeography-based optimization is a relatively recent addition to the field of evolutionary optimization algorithms [111]. This global optimization method is supported by the mathematical models of biogeography observed in nature, that is the emigration (exiting) of species from and immigration (entering) of species into isolated habitats. Each habitat possesses a set of Suitability Index Variables (SIV); these rep-

resent features of the habitat such as availability of food and water, shelter, climate, etc. The SIV set defines the overall suitability of the habitat, which is measured by the Habitat Suitability Index (HSI). For a given habitat, therefore, a higher HSI indicates that more species will take residence. A larger number of species leads to abundant emigration: species will spread from a high HSI habitat to other habitats. Conversely, this habitat will have a low immigration rate because the resources are already claimed by the resident species. The opposite holds for a low HSI habitat. In this case there are both limited resident species, resulting in little emigration, and excess space, allowing immigration.

Transferring these concepts to the solution of optimization problems, each candidate solution is seen as a unique habitat. Each candidate's HSI in standard optimization terms is the cost function. The SIV represent the features of a candidate solution. The algorithm progresses in a generational manner. The first generation population is initialized randomly within the given ranges for each feature and is sorted; sorting will be discussed in detail later. Copies of a small number ( $n$ ) of the best solutions are stored, and features of the sorted population are then probabilistically shared such that higher HSI candidates more frequently provide (emigrate) features to lower HSI candidates (immigration recipients). Upon concluding this process, some features of some candidates are probabilistically mutated, reducing the likelihood of finding a local minimum. The  $n$  elite solutions are added to the population, and it is sorted.  $n$  of the worst candidate solutions are then eliminated. Note that while the elite solutions are prevented from being the recipients of immigration or mutating, they can still be sorted out of the population in the case that the past generation's elites are the current generation's worst candidates. The resulting population initializes the next generation.

A means of handling constraints must be layered over the basic BBO method. This is addressed within the sorting algorithm by which candidate solutions are



ranked from highest to lowest HSI. The  $\epsilon$ -level comparisons method was chosen for this work because it allows infeasible solutions with superior cost functions to potentially rank as well as feasible solutions with the same cost, yet shifts emphasis to maintaining feasible solutions (assuming existence) within the population during late generations [124]. Using the maximum constraint violation  $M$ , this can be expressed as

$$x \text{ ranks higher than } y \text{ if } \begin{cases} f(x) < f(y) \text{ and } M(x) \leq \epsilon \text{ and } M(y) \leq \epsilon, \text{ or} \\ f(x) < f(y) \text{ and } M(x) = M(y), \text{ or} \\ M(x) < M(y) \text{ and } M(y) > \epsilon \end{cases} \quad (6.33)$$

for two candidate solutions  $x$  and  $y$ , where  $f$  is the cost function and  $\epsilon \geq 0$  defines the level of allowable constraint violation [112].  $\epsilon$  is decreased with increasing generation count. From [112] this can be implemented as

$$\begin{aligned} \epsilon(0) &= M(x_p) \\ \epsilon(t) &= \begin{cases} \epsilon(0) \left(1 - \frac{t}{T_c}\right)^c & \text{if } 0 < t < T_c \\ 0 & \text{if } t \geq T_c, \end{cases} \end{aligned} \quad (6.34)$$

where  $p = N/5$ ,  $N$  is the population size,  $x_p$  is the solution with the  $p$ -th smallest constraint violation,  $t$  indicates the current generation count, and  $T_c$  and  $c$  are tuning parameters. Recommended values are  $c = 100$  and  $T_c = t_{max}/5$  [124].

### Cost and Constraint Functions for Optimal Exercise

Applying BBO to the optimal exercise problem requires the development of a scalar cost function. This work proposes the use of a muscle activation-based cost

function

$$- \frac{1}{\mathbb{J}T} W \int_0^T a(t) dt, \quad (6.35)$$

where  $\mathbb{J}$  is the total number of muscles,  $T$  is the period,  $W$  is a  $1 \times \mathbb{J}$  vector of weights, and the integral of the muscle activations  $a$  over time is of dimension  $\mathbb{J} \times 1$ . The negative indicates that maximization of the muscle activations is desired. To select a single muscle  $j$  for maximization,  $W$  is simply defined as a vector of negative ones except for element  $j$ , which is assigned a positive value. Recommended practice is to start with a positive 1, which has been sufficient for single muscle optimization in the example cases to be shown.

Constraints for this problem can be divided into four categories—trajectory, solver, state and control, and exercise definition. Trajectory constraints ensure reachability of the trajectories and anatomical correctness. All joint trajectories are checked for imaginary solutions, indicating that the trajectory is unreachable. Including the desired and actual trajectories of the exercise machine and the trajectory of the arm for two joints each system leads to a total of six constraints. To maintain anatomically correct trajectories, the shoulder is not allowed to go beyond  $-30$  degrees clockwise. Similarly, the elbow cannot extend beyond  $5$  degrees, preventing hyperextension and acceleration extremes. Lastly, it is confirmed that the inverse kinematics did not jump to a solution adding a multiple of  $2\pi$  to the trajectories. Constraint ( $c$ ) violations in this category are evaluated in a discrete manner.  $V_c = 1$  is assigned for a violation and  $V_c = 0$  is assigned for no violation. The trajectory constraints are summed and then scaled by a factor of 10

$$10 \sum_c V_c \quad (6.36)$$

to ensure that this combined constraint maintained a generally larger magnitude than the state and control constraints. Constraints on the trajectory are applied before enacting the solver, reducing function evaluations. Under this circumstance the cost

	Trajectory Parameters (Figure 45)						Impedance Parameters (6.19)		
	$a_a, b_a,$ $a_d, b_d$	$xc_a,$ $xc_d,$	$yc_a,$ $yc_d$	$\phi_a,$ $\phi_d$	$f$	Direction	$I_x, I_y$	$B_x, B_y$	$K_x, K_y$
Lower Limit	$5 \times 10^{-3}$ m	-0.6 m	0 m	0 rad	0.1 Hz	-1 (CW)	0 kg	0 kg/s	0 N/m
Upper Limit	0.3 m	0.6 m	0.6 m	$\pi$ rad	3 Hz	1 (CCW)	200 kg	500 kg/s	1000 N/m

Table VIII: Parameter range limits for exercise optimization. CW indicates clockwise, and CCW indicates counterclockwise

function is assigned the constraint value.

Second, if the SOS or LP solver fails, both the cost and constraint functions are set to infinity. This also applies to the related cases where no suitable  $FT_{reserve}$ , defined by  $FT_{reserve} \leq \min(F_{max})$ , or solution for  $n$  can be found.

Third, for all solutions having passed both previous levels of constraint checking, the muscle activation state and neural input constraints are applied

$$\begin{aligned}
\min_j \min_t a_j(t) &\geq 0 \\
\max_j \max_t a_j(t) &\leq 1 \\
\min_j \min_t n_j(t) &\geq 0 \\
\max_j \max_t n_j(t) &\leq 1.
\end{aligned} \tag{6.37}$$

These maintain the muscle states and controls within the ranges acceptable for the Hill muscle model.

Lastly, a constraint was implemented to limit the maximum force magnitude applied by the machine endpoint to some value set by the investigator,  $\overline{F}_{ext}$ .

$$\max_t \|F_{ext}(t)\| \leq \overline{F}_{ext} \tag{6.38}$$

## Optimal Exercise Search Space

The parameter limits used for all exercise optimizations are given in Table VIII. The reachable space of the human arm primarily guided the scaling and location of

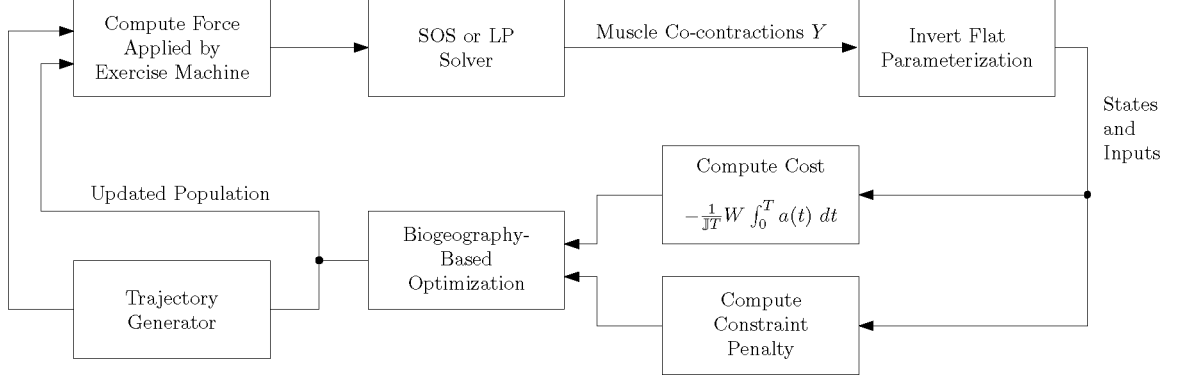


Figure 46: Process for a single trial of the exercise optimization problem

the elliptical trajectories for the machine (actual and desired) and the arm. The arm can reach 0.65 m when fully extended. In addition, the exercise machine can only reach to the shoulder point (origin). The range for the orientation of the ellipse allows all cases. Trajectories ranging in execution time from 1/3 to 10 seconds are allowed, and the trajectory can be executed in either the clockwise or counterclockwise direction. Ample ranges for the impedance parameters permit the optimization to achieve flexibility in the orientation of the resultant force along the trajectory while the force magnitude is managed by the previously described constraint. The upper bounds for the impedance parameters were increased until the optimal solutions were typically not on the boundary. For all trials  $\bar{F}_{ext}$  was set at 45 N  $\approx$  10 lbf.

Figure 46 shows all components of the optimal exercise method combined, providing a summary of Section 6.5.

## 6.6 Results

In applying the solver to the optimal exercise problem, general understanding of the behavior of the solver was sought, especially with respect to muscle independence, effective constraint protection, and solver speed. Selected optimization trials show that individual muscles can be isolated and the external optimizer can maintain the constraints. These trials also reveal the solver's preference toward selecting constant

co-contractions. Repeated timed trials illustrate the speed advantage of the solver.

### 6.6.1 Selected Optimal Exercise Trials

For each individual muscle a maximization problem was solved. A total of five successful Monte Carlo trials with a population size of 50 and 300 generations were completed for each muscle. Successful trials is denoted because it is possible for the population to remain infeasible across all generations. For this reason the epsilon level for constraints was set at  $T_c = t_{max}/1.25$ , allowing exploration for more generations than the recommended value of  $T_c$ . Barring the possibility of a completely infeasible trial, the given combination of population size and generations maintained reasonable run times and good convergence. However, more trials would be required to identify global optima. Nevertheless, a variety of feasible solutions were found, and the variation observed could prove beneficial for clinical selection. According to the procedure previously outlined for choosing weights, a positive weight of 1 was used for the muscle of interest during that trial. The other five muscles' weights were set to negative 1. The best trial from the five Monte Carlo trials completed for each muscle and the associated final cost of that trial are summarized in Table IX.

Examining the effects of the resulting parameters more closely yields insight into the discovered exercise solutions. For each solution assessing the Cartesian trajectories and forces applied to the arm endpoint provides an intuitive understanding of the result. This is then supported by observing the muscle activations, which indicate the effectiveness of the selected cost function.

Muscle Maximized	(1) Anterior Deltoid	(2) Posterior Deltoid	(3) Biceps Brachii	(4) Triceps Brachii (long head)	(5) Triceps Brachii (short head)	(6) Brachialis
Trial Cost	-0.1076	-0.1017	-0.0768	-0.1142	-0.1011	-0.1282
$a_a$ (m)	0.0427	0.0833	0.0206	0.0421	0.0604	0.0058
$b_a$ (m)	0.0489	0.0177	0.0647	0.0323	0.0278	0.0245
$xc_a$ (m)	-0.1706	0.2884	-0.2378	0.2595	0.0300	-0.0025
$yc_a$ (m)	0.5252	0.2699	0.3251	0.4780	0.1892	0.1246
$\phi_a$ (rad)	1.6915	2.5068	2.2007	2.8117	1.4481	2.6590
$a_d$ (m)	0.0293	0.2539	0.1760	0.0247	0.0660	0.0301
$b_d$ (m)	0.0882	0.0461	0.0346	0.0678	0.0412	0.0130
$xc_d$ (m)	0.4721	0.1876	0.2044	0.0890	-0.2662	-0.0748
$yc_d$ (m)	0.2612	0.3455	0.5140	0.2076	0.1177	0.5972
$\phi_d$ (rad)	1.8385	2.7626	3.0363	2.2266	1.2284	3.0286
$f$ (Hz)	0.2785	0.1200	0.1146	0.1835	0.1830	0.1546
Direction	CCW	CW	CW	CW	CW	CW
$I_x$ (kg)	32.8623	1.5144	44.8465	128.1005	167.7276	11.6536
$I_y$ (kg)	35.0128	166.8032	1.3386	197.3658	194.9124	134.7549
$B_x$ (kg/s)	51.9952	1.2646	52.8979	44.9777	378.5293	164.8673
$B_y$ (kg/s)	89.3277	80.7159	286.7059	145.5636	11.8436	5.3669
$K_x$ (N/m)	51.4176	43.0219	23.4450	205.5939	19.7304	15.8905
$K_y$ (N/m)	97.5508	253.2602	222.8894	71.3092	471.8879	87.0280

Table IX: Optimal exercise trajectory and impedance parameters resulting from six trials, one for each muscle. CW indicates clockwise. CCW indicates counterclockwise

### **Trial 1: Anterior Deltoid**

The results for maximizing the Anterior Deltoid are shown in Figures 47 and 48. The orientation of the trajectories and selected impedance parameters give a fairly uniform distribution of  $F_{ext}$ . This combination is effective in realizing an increased activation for the Anterior Deltoid and minimizing all other muscles' activations. The increased activation corresponds to increased tendon force for that muscle, which is shown as an example case in Figure 49. However, it is clear that the Anterior Deltoid tendon force did not reach its maximum capacity ( $F_{max1} = 800\text{ N}$ ) in contrast to what is suggested by the activation. This can be attributed to the influence of the force-length and force-velocity dependencies of the muscle model.

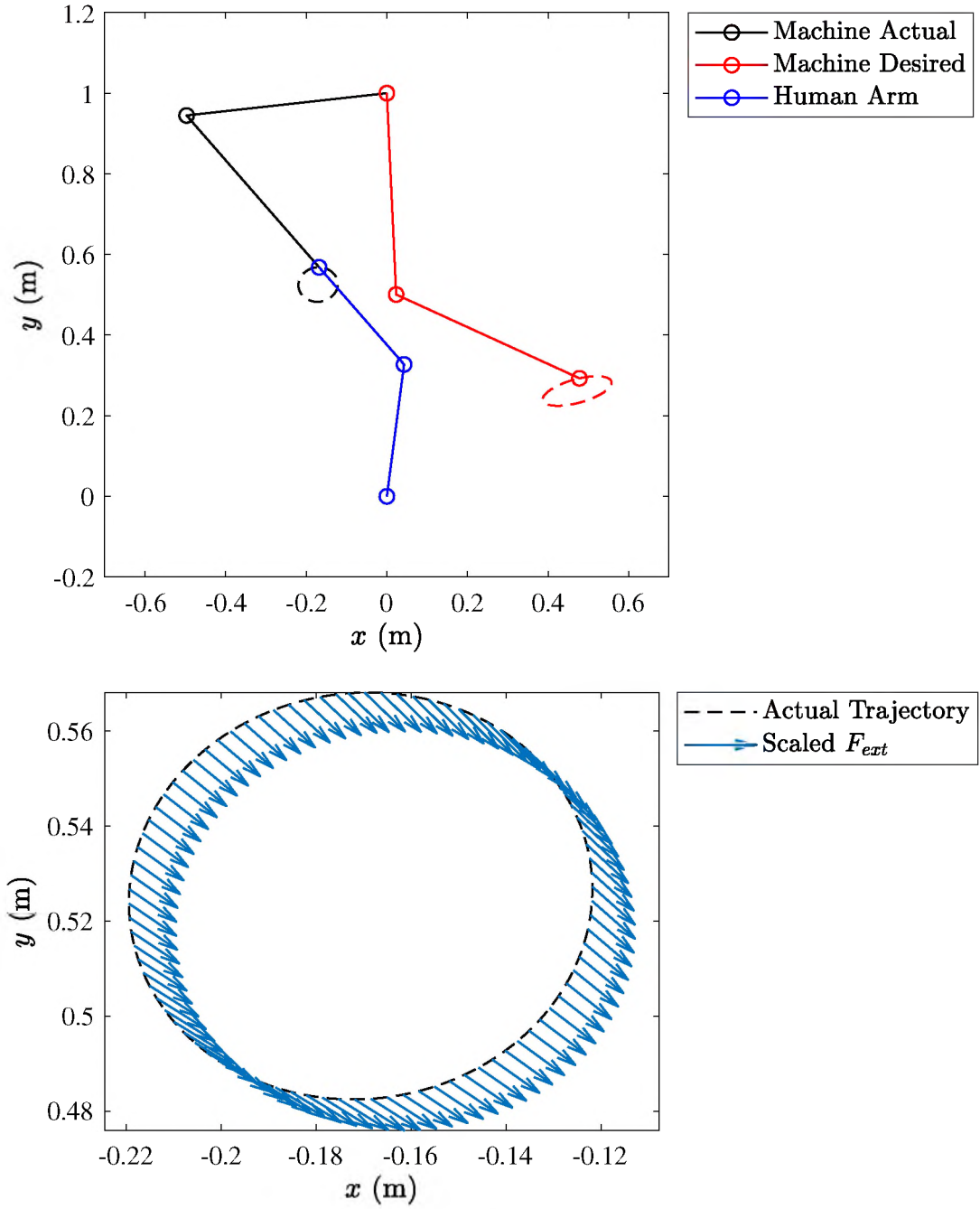


Figure 47: Top: Cartesian representation of the desired (red) and actual (black) trajectories (dashed) found to maximize the Anterior Deltoid muscle activation. The exercise machine is shown in its actual position (black) as guided by the human arm (blue). The exercise machine's desired position that it is drawing the arm toward is also shown (red). Bottom: Scaled forces applied to the arm endpoint along the trajectory



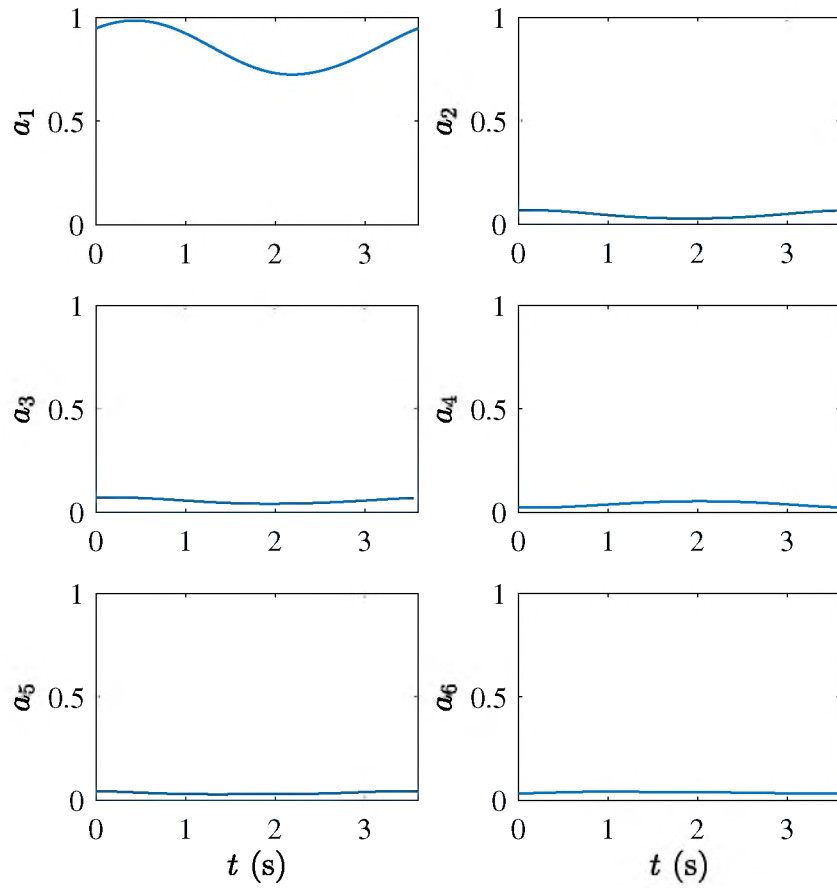


Figure 48: Muscle activations found when maximizing the Anterior Deltoid muscle activation. The muscles are (1) Anterior Deltoid, (2) Posterior Deltoid, (3) Biceps Brachii, (4) Triceps Brachii (long head), (5) Triceps Brachii (short head), and (6) Brachialis

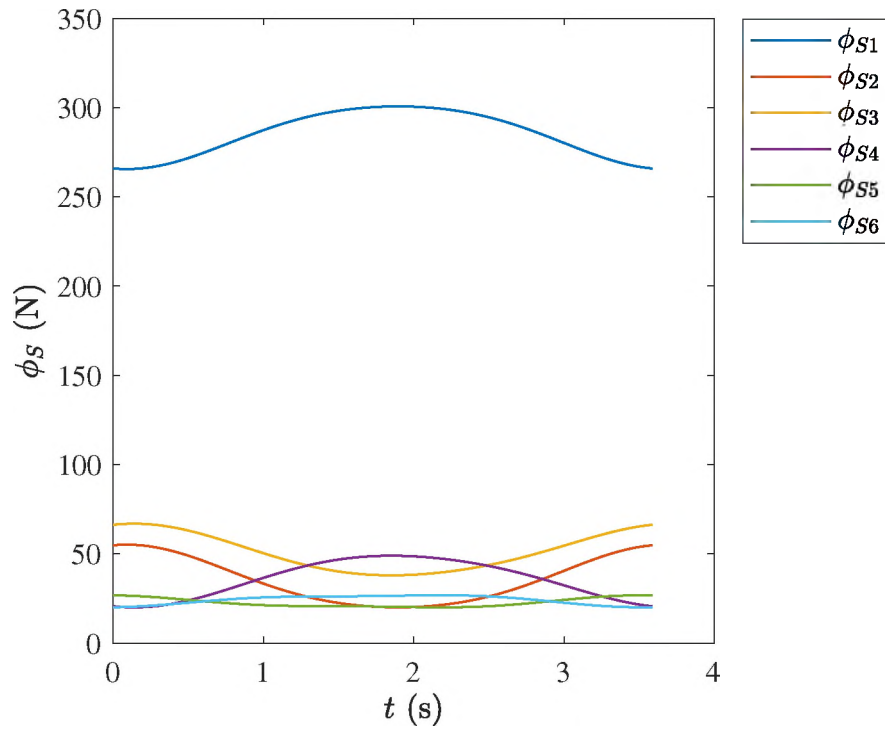


Figure 49: Tendon forces resulting from maximizing the Anterior Deltoid muscle activations. The muscles are (1) Anterior Deltoid, (2) Posterior Deltoid, (3) Biceps Brachii, (4) Triceps Brachii (long head), (5) Triceps Brachii (short head), and (6) Brachialis

## **Trial 2: Posterior Deltoid**

Maximizing the Posterior Deltoid, Figures 50 and 51, gives an example of a relatively slowly executed trajectory. The muscle activations and associated cost show that the optimization was as effective as the Anterior Deltoid case. The combination of trajectories and impedance parameters lend more diversity to  $F_{ext}$  than was seen with the Anterior Deltoid. Accordingly, the tendon forces, Figure 52, have a larger range than the Anterior Deltoid while still emphasizing the Posterior Deltoid.

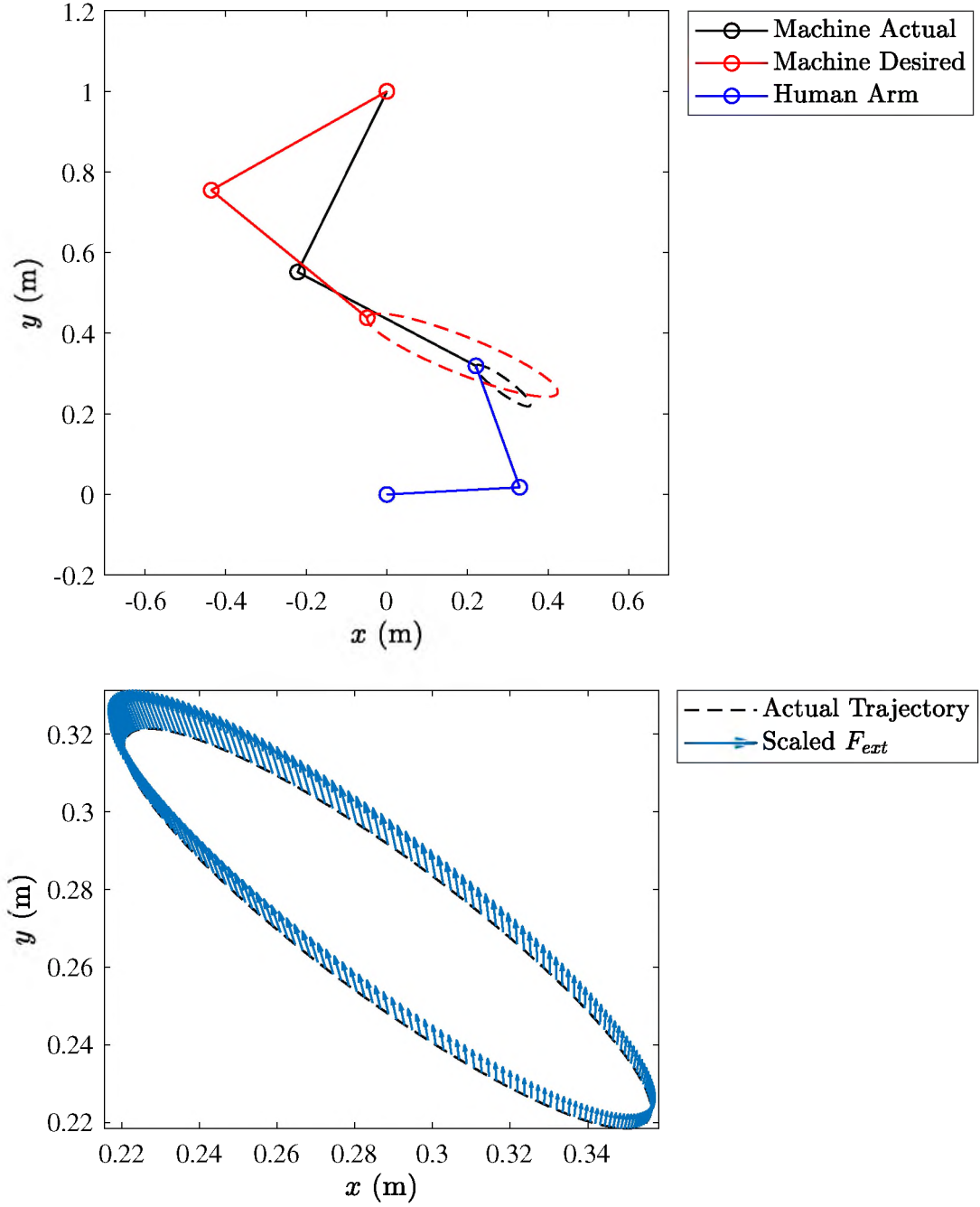


Figure 50: Top: Cartesian representation of the desired (red) and actual (black) trajectories (dashed) found to maximize the Posterior Deltoid muscle activation. The exercise machine is shown in its actual position (black) as guided by the human arm (blue). The exercise machine's desired position that it is drawing the arm toward is also shown (red). Bottom: Scaled forces applied to the arm endpoint along the trajectory

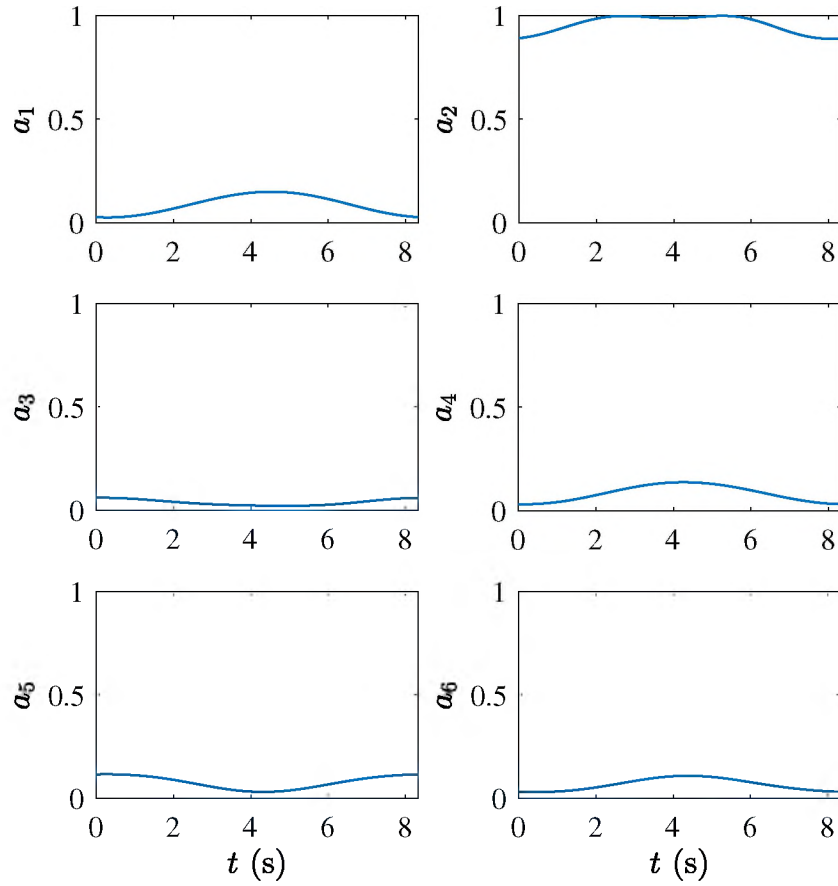


Figure 51: Muscle activations found when maximizing the Posterior Deltoid muscle activation. The muscles are (1) Anterior Deltoid, (2) Posterior Deltoid, (3) Biceps Brachii, (4) Triceps Brachii (long head), (5) Triceps Brachii (short head), and (6) Brachialis

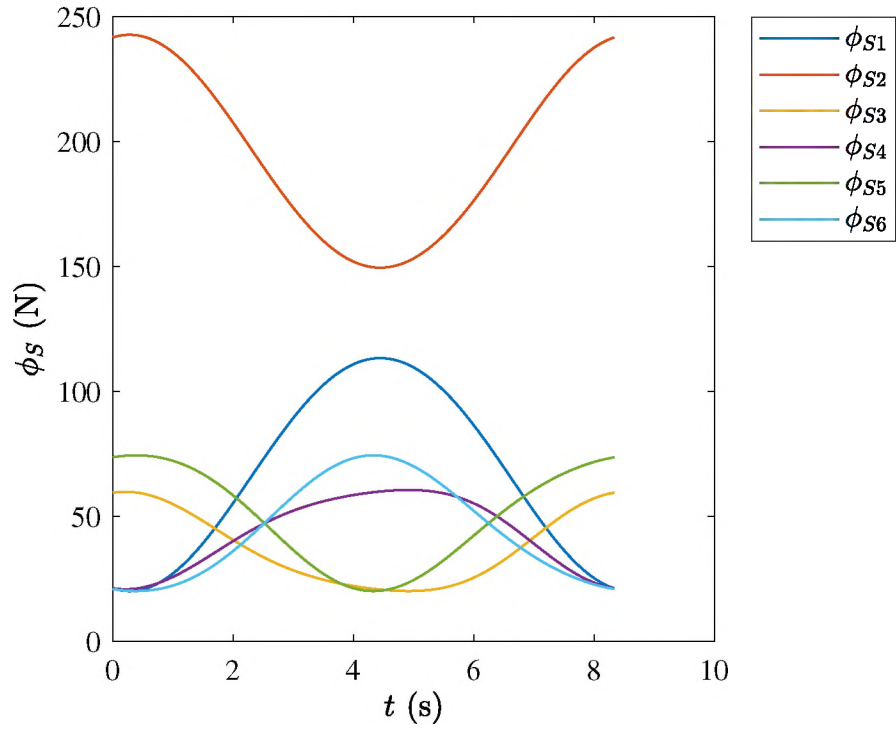


Figure 52: Tendon forces resulting from maximizing the Posterior Deltoid muscle activations. The muscles are (1) Anterior Deltoid, (2) Posterior Deltoid, (3) Biceps Brachii, (4) Triceps Brachii (long head), (5) Triceps Brachii (short head), and (6) Brachialis

### **Trial 3: Biceps Brachii**

The case of maximizing the Biceps Brachii muscle activation indicates increased difficulty in finding solutions for a bi-articular muscle. Figures 53 and 54 provide the associated Cartesian trajectories, external force on the arm endpoint, and muscle activations. The best result found over five successful trials gives an activation of just over  $1/2$  in contrast to the activations nearing 1 found for the Deltoids. Even so, the Biceps muscle is effectively singled-out by the optimization.

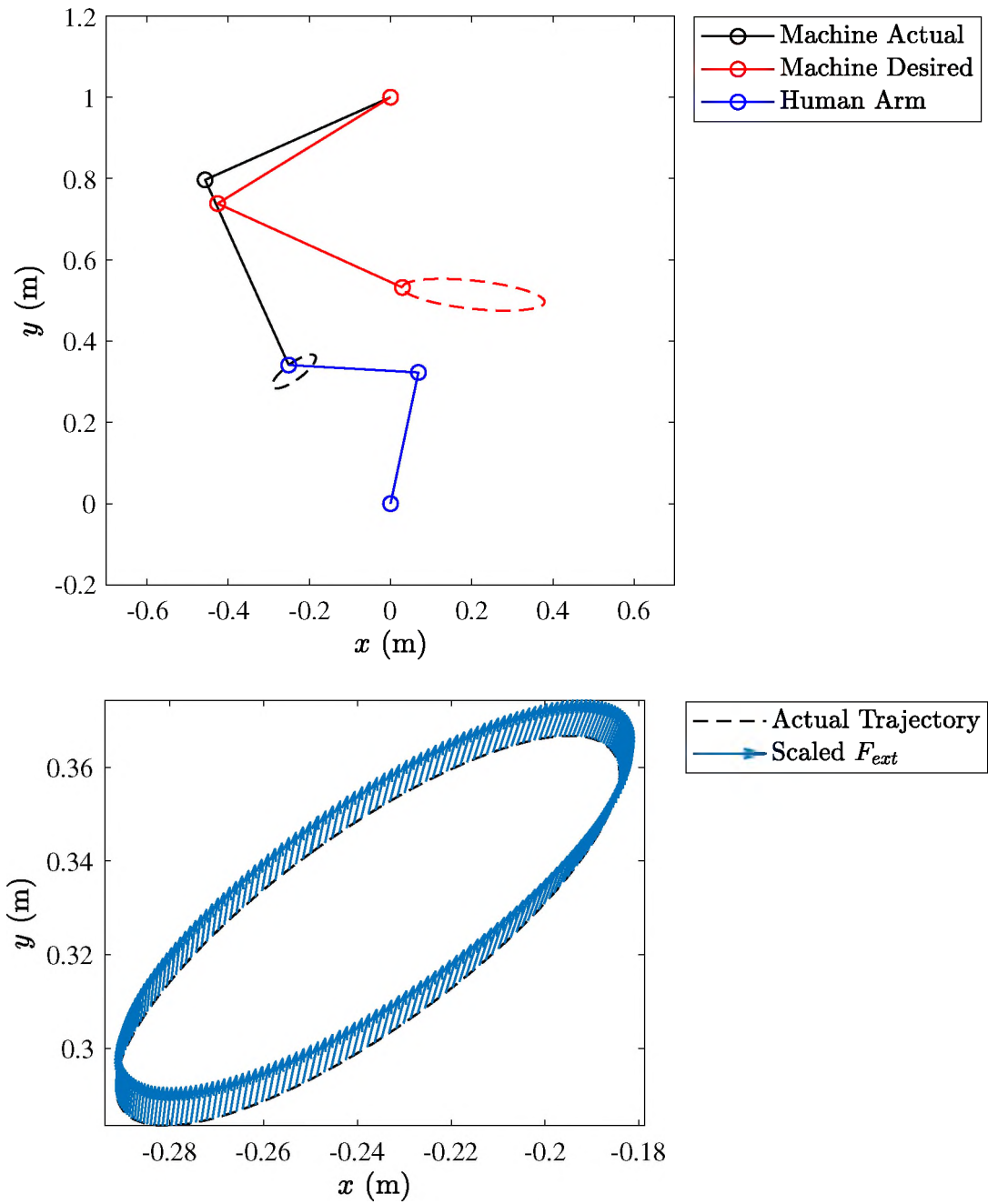


Figure 53: Top: Cartesian representation of the desired (red) and actual (black) trajectories (dashed) found to maximize the Biceps Brachii muscle activation. The exercise machine is shown in its actual position (black) as guided by the human arm (blue). The exercise machine's desired position that it is drawing the arm toward is also shown (red). Bottom: Scaled forces applied to the arm endpoint along the trajectory



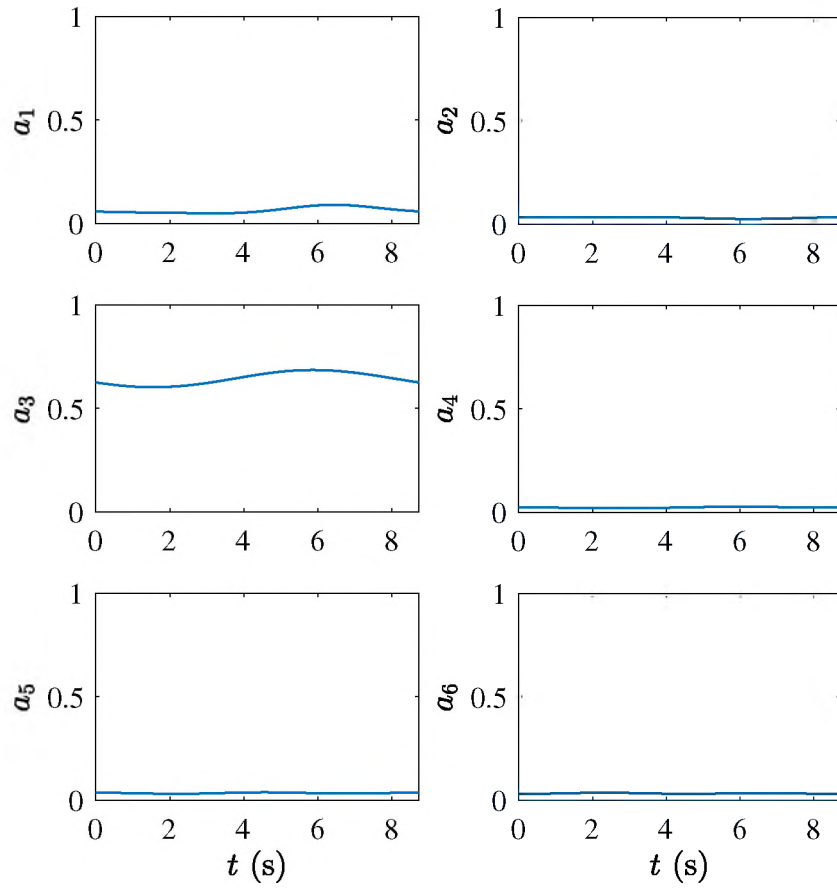


Figure 54: Muscle activations found when maximizing the Biceps Brachii muscle activation. The muscles are (1) Anterior Deltoid, (2) Posterior Deltoid, (3) Biceps Brachii, (4) Triceps Brachii (long head), (5) Triceps Brachii (short head), and (6) Brachialis

#### **Trial 4: Triceps Brachii (long head)**

Examining the other bi-articular muscle, the Triceps Brachii (long head), in Figures 55 and 56, a stronger result can be noted in comparison to the Biceps for the muscle activation. However, thirteen trials were required to achieve five successful trials, again suggesting the higher difficulty level of the bi-articular muscle problem. The location of the desired trajectory of the Triceps Brachii (long head) is directly along the line from the shoulder to the actual trajectory, which should concentrate the effort requirement at the elbow joint [70]. This result in combination with the higher cost function for the Biceps Brachii in comparison to the Triceps Brachii (long head) could indicate that maximizing the Biceps requires a revised search space. For example, the machine desired trajectory being allowed outside of the arm's reach along the same line.

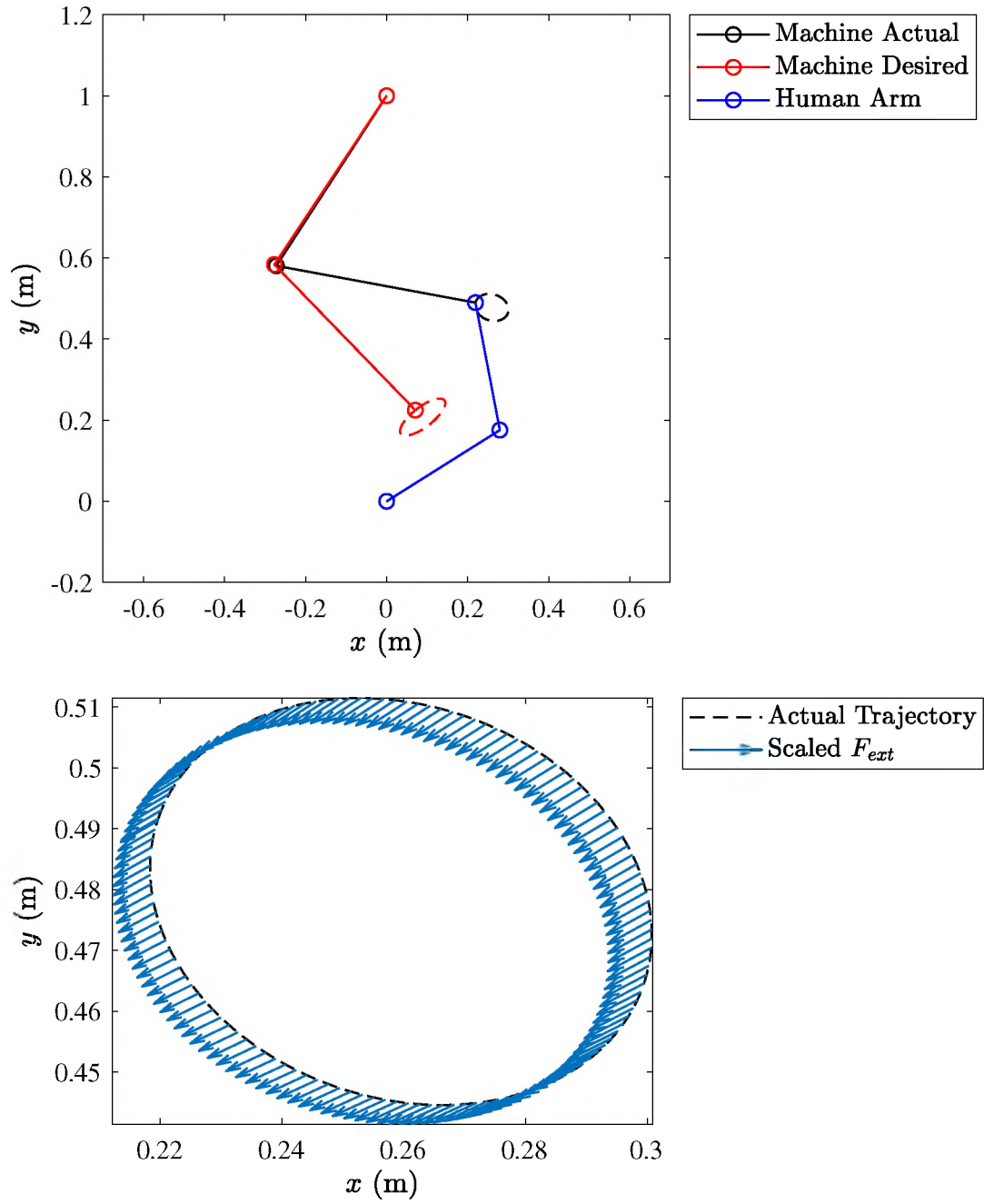


Figure 55: Top: Cartesian representation of the desired (red) and actual (black) trajectories (dashed) found to maximize the Triceps Brachii (long head) muscle activation. The exercise machine is shown in its actual position (black) as guided by the human arm (blue). The exercise machine's desired position that it is drawing the arm toward is also shown (red). Bottom: Scaled forces applied to the arm endpoint along the trajectory

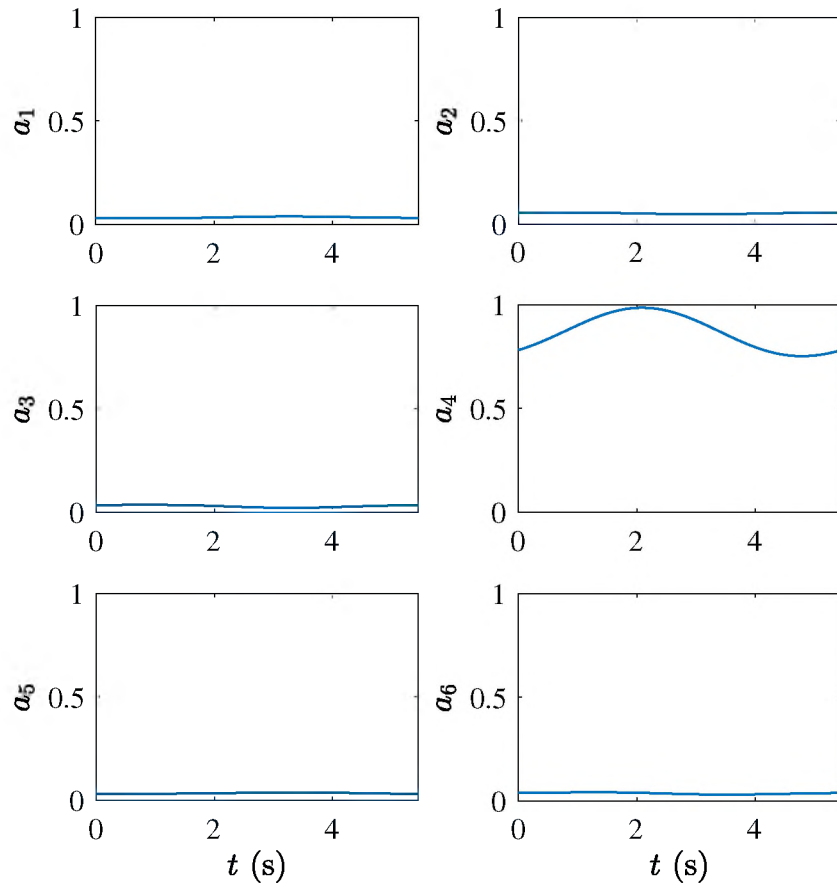


Figure 56: Muscle activations found when maximizing the Triceps Brachii (long head) muscle activation. The muscles are (1) Anterior Deltoid, (2) Posterior Deltoid, (3) Biceps Brachii, (4) Triceps Brachii (long head), (5) Triceps Brachii (short head), and (6) Brachialis

### **Trial 5: Triceps Brachii (short head)**

The selected optimal solution for the Triceps Brachii (short head) also achieves the goal of maintaining higher activations for the muscle being maximized throughout the exercise; see Figures 57 and 58. Within this solution, among others, it is clear that the upper constraint on the muscle activations is being effectively protected. Also, this case can be used as an example of the muscle co-contractions. Figure 59 shows that the co-contractions are constant over the exercise period. This feature can be seen for all trials across all muscles.

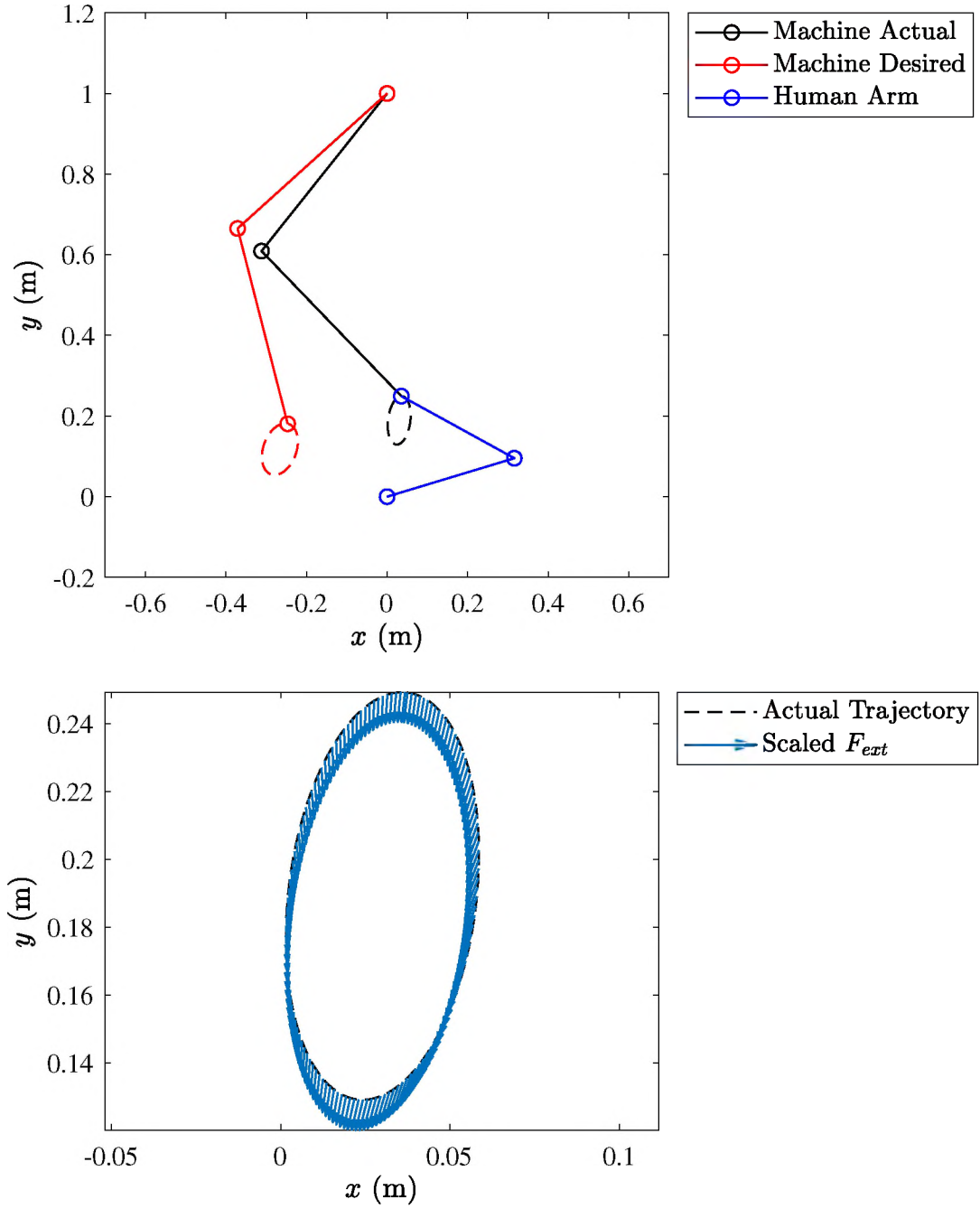


Figure 57: Top: Cartesian representation of the desired (red) and actual (black) trajectories (dashed) found to maximize the Triceps Brachii (short head) muscle activation. The exercise machine is shown in its actual position (black) as guided by the human arm (blue). The exercise machine's desired position that it is drawing the arm toward is also shown (red). Bottom: Scaled forces applied to the arm endpoint along the trajectory

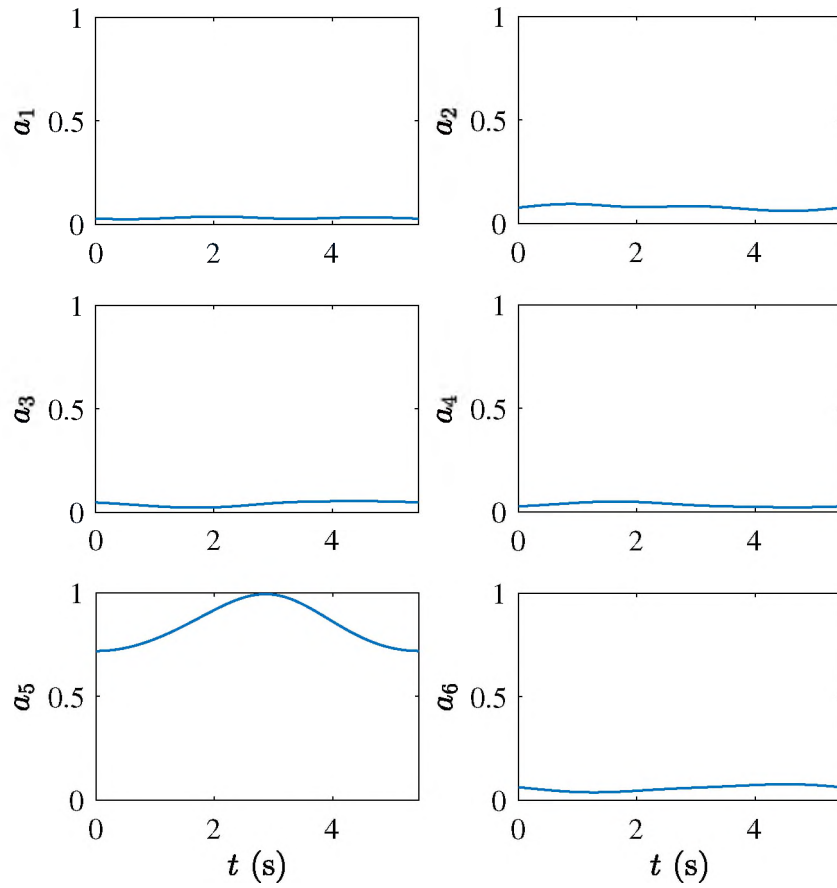


Figure 58: Muscle activations found when maximizing the Triceps Brachii (short head) muscle activation. The muscles are (1) Anterior Deltoid, (2) Posterior Deltoid, (3) Biceps Brachii, (4) Triceps Brachii (long head), (5) Triceps Brachii (short head), and (6) Brachialis

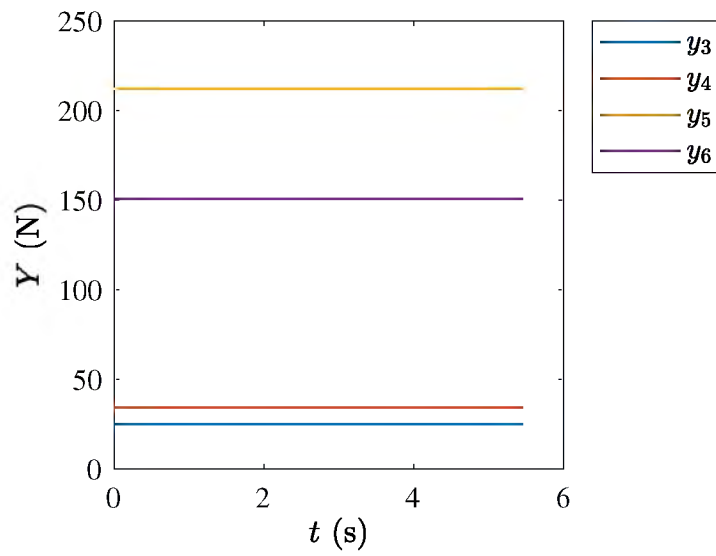


Figure 59: Muscle co-contractions resulting from maximizing Triceps Brachii (short head)



## **Trial 6: Brachialis**

Concluding with the Brachialis muscle, a substantial difference in the activation of the muscle of interest can be observed in Figure 61 for the trajectory of Figure 60. It is nearest to constant full activation out of all of the individual muscle trials as shown by its cost value and the activation plots. From the trajectories it is noted that this is a nearly static exercise. This might be beneficial under some circumstances, or a more dynamic solution could be selected from the set of feasible trials. Solutions can also be influenced toward or away from being static based on the selection of the minimum ellipse axis sizes and the frequency prior to optimization.

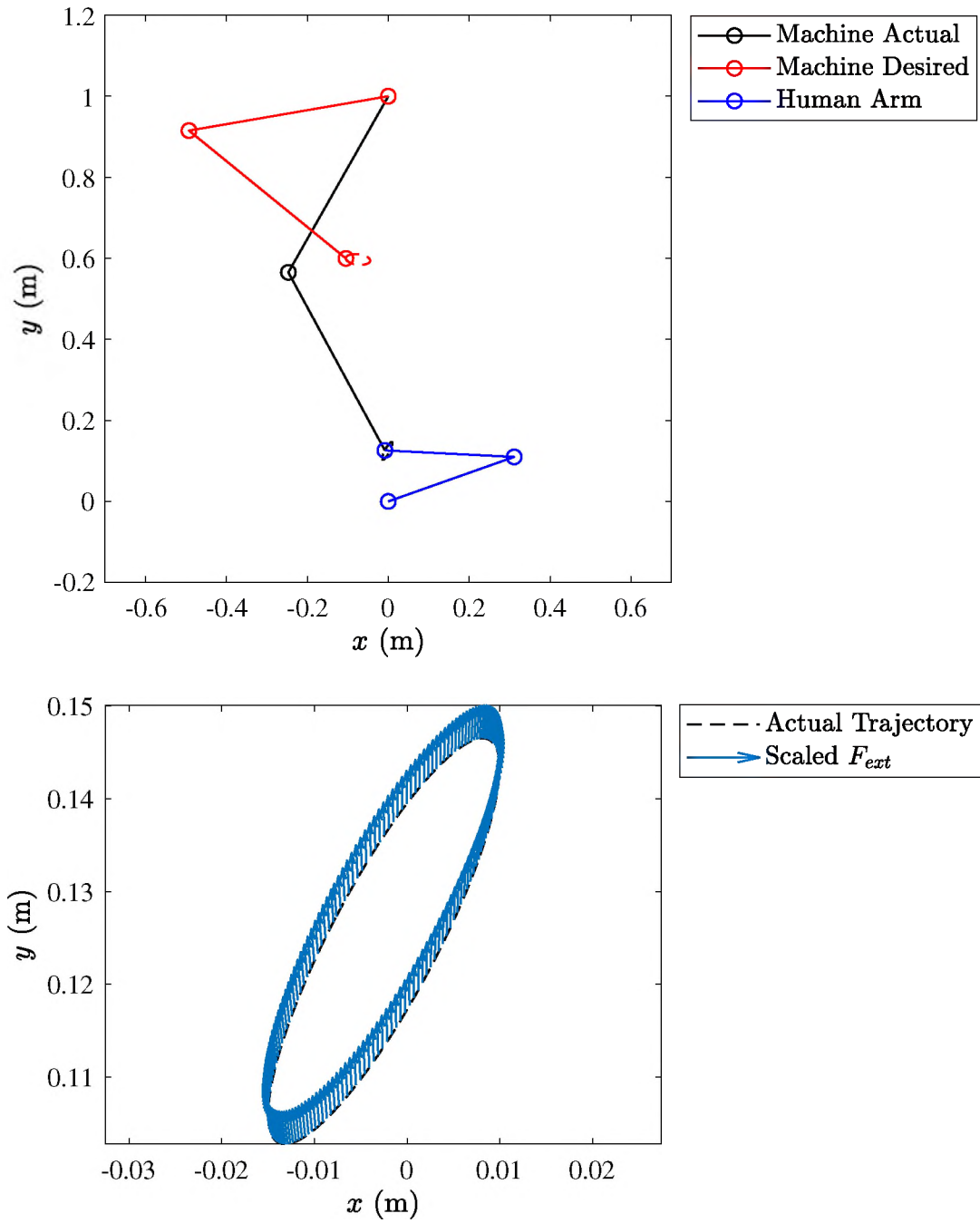


Figure 60: Top: Cartesian representation of the desired (red) and actual (black) trajectories (dashed) found to maximize the Brachialis muscle activation. The exercise machine is shown in its actual position (black) as guided by the human arm (blue). The exercise machine's desired position that it is drawing the arm toward is also shown (red). Bottom: Scaled forces applied to the arm endpoint along the trajectory

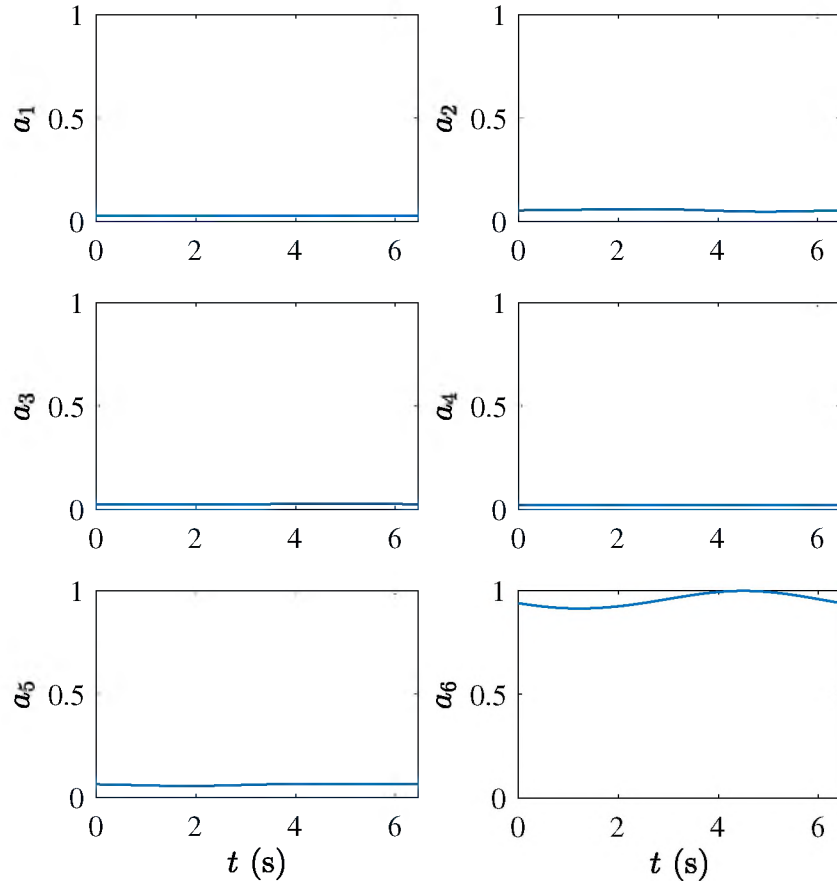


Figure 61: Muscle activations found when maximizing the Brachialis muscle activation. The muscles are (1) Anterior Deltoid, (2) Posterior Deltoid, (3) Biceps Brachii, (4) Triceps Brachii (long head), (5) Triceps Brachii (short head), and (6) Brachialis

### 6.6.2 Constant Co-contractions

It was observed that across all muscles and all computed solutions constant co-contractions are selected by the linear program; the same feature is seen in results from using the SOSTOOLS solver, as expected. The source of this phenomenon can be shown analytically for the quartic polynomial. Consider that because the cost function in the space of polynomial coefficient vectors  $\alpha_0$  and  $\alpha_4$  is linear, leading to a non-zero gradient, the problem would be unbounded without the existence of constraints. With convex, feasible constraints the optimal combination of coefficients will be at an edge or vertex of the constraints.

By elimination each constraint can be identified as either a strict equality or strict inequality. Assume equality for (6.27); substituting into (6.30) requires that  $B \leq 0$ , which is not true in general. The same conclusion can be stated for assuming equality for (6.29) from (6.32). Therefore, it holds that (6.27) and (6.29) are strict inequalities. Now observe that neither the gradient of (6.30) nor of (6.32) is parallel with the gradient of the cost. Therefore, they must both be active equality constraints. Accordingly, combining these two constraints under strict equality requires  $\alpha_4 = 0$ , yielding constant polynomials, because the columns of  $C_Y$  are linearly independent from being extracted from an invertible matrix. This implies that constraints (6.28) and (6.31) are also equalities, which yields no contradiction.

In light of this result for the quartic polynomial with periodicity constraints and testing completed using SOSTOOLS for up to tenth degree polynomials with and without periodicity constraints, it is conjectured that the optimality of constant co-contractions holds for SOS polynomial solutions in general under the current structure of the open-loop solver. Improved EMG data from new experiments as discussed in Section 6.4 can help to validate how realistic constant tendon force averages

are. It seems likely that there are circumstances under which modeling human co-contractions would require more freedom than is allowed by constant polynomials. Concurrently, it is noted that this is not a limitation of the open-loop solver concept as it is capable of non-constant co-contractions. For example, if  $\alpha_4 > C$  is used rather than non-negativity, where  $C$  is some positive constant, the co-contractions are forced to be non-constant. Further study is required to identify whether the constant co-contractions are a consequence of the system or due to a yet unrecognized assumption.

### 6.6.3 Computational Efficiency

To provide insight into the computation efficiency of the solver, it was timed while running the best case found for the Anterior Deltoid. The optimal control solver was evaluated using both the SOSTOOLS and linear programming solution methods on a computer with an Intel Core i7-7700HQ processor running at the “Turbo Boost” clock speed of 3.60 GHz with 16 GB of RAM. Over five trials SOSTOOLS required an average of 6.69 s. In contrast, the linear program was able to be completed in 0.029 s on average. While the linear programming solution is indeed specialized to the problem of interest, the computation savings support the effort of developing a linear program where possible. As another point of comparison, it has been reported that the method termed forward static optimization, which also uses a predefined trajectory, requires 7.9 s to complete an arm simulation with what appears to be the same model on a comparable processor [108]. The SOSTOOLS method is competitive with this result and could represent computational savings of up to 18%. The linear program runs 272 times faster than the example provided for forward static optimization.

While an equivalent model could not be found to compare the optimal control solver wrapped in a trajectory optimization to dynamic optimization, some more general observations can be made. Reference [1] reports a 35 minute solution time

using direct collocation for 1/2 of a walking gait cycle for a planar model. One trial with BBO for the Anterior Deltoid optimization using the linear program required an average across 5 trials of 10.5 minutes with a range of 7.8–12.1 minutes. The variation in speed partially depends on which generation iteration the population begins to be feasible and the number of feasible individuals needing to be evaluated each generation. For example, the fastest time correlates with the trial with the largest sum of the average constraint violation across the 300 evaluated generations. Likewise, the slowest time correlates with the trial with the smallest average constraint violation sum. Though a direct comparison cannot be made, it seems possible that the trajectory optimization and solver combination computation time could at least be comparable to direct collocation. Arguably, the implementation of differential flatness should provide an advantage because the system dynamics need not be included in the set of constraints as it is in direct collocation.

## 6.7 Remarks

A novel parameterization of musculoskeletal dynamics produces a analytically amenable and computationally feasible optimal control solver. Differential flatness simplifies model evaluation and contributes computational speed. SOS polynomial techniques allow analytical expressions for muscle co-contractions, which is based on insight from the previous chapter into the importance of muscle co-contractions. The solution of these co-contractions can be reduced to a linear program under various circumstances and further simplifies to constant co-contractions in many cases. The results of the solver were shown valid against EMG data. Measured computation times indicate that the solver is competitive with published methods when utilizing SOSTOOLS and sees a significant speed advantage when employing a linear program.

### 6.7.1 Exercise Optimization

In applying the optimal control solver to exercise optimization, a variety of results were produced, but for all cases a specific muscle could be almost completely isolated. Additionally, the optimization effectively protected the required constraints. The variation in the results provides insight into ways to improve the optimal exercise approach. First, stronger results for some muscles might be possible by extending the search space for the desired trajectory. It is noted, however, that the chosen ranges provide a measure of safety considering the physical implementation of these trajectories. Assuming some safety controls could be implemented though, this extended search space could be particularly important for the desired trajectories as they are currently limited to the same search space as the actual trajectories. For example, the placement of the desired ellipse could be behind the exercise subject's back, adding different dynamics than have been considered here.

Second, the results also revealed the effects of the cost function. In particular, the activations can be fully maximized when the muscle force is not due to additional dependence on the force-length and force-velocity relationships. Therefore, a muscle force-based cost function might reduce the variety seen in the chosen trajectories, yielding global optima. On the other hand, muscle activations are closest to the clinically feasible measurement EMG. To use muscle force in practice would require implementing a form of estimation at least.

While this approach does not guarantee quick solution of global optima, it can facilitate exercise studies, as was completed here. Additionally, it can provide initialization conditions for applications like extremum seeking control in practice.

### 6.7.2 Receding Horizon Control

A major impetus to the development of the optimal control solver is receding horizon control, in particular MPC, due to the inherent ability of these methods to

protect constraints. These methods require the repeated solution of an open-loop optimal control problem, application of the result for one simulation time step, and reevaluation of the optimal control problem starting at the updated initial conditions. These extensive function evaluations demand computational efficiency. In addition, implementation requires recursive feasibility of the optimal control solution. A proof of this property for the optimal control solver developed in this chapter is provided in [102]. Alongside this requirement to implement MPC, a linear program handling more general initial and final conditions would be beneficial. Fully establishing the optimality of constant co-contractions should support this endeavor.



## CHAPTER VII

## CONCLUSION

### 7.1 Summary

This work began with involvement in powered transfemoral prosthesis research. Out of that came a prototype prosthesis and controller. The prosthesis proved capable during tests with an individual with an amputation of attaining basic gait features while performing energy regeneration under a unifying control law that could handle variation in gait speed. Though yet untested, the controller is anticipated to be able to handle climbing slopes and stairs and the sit-to-stand motion.

Through engaging with prosthetics, a gap in the capacity to test machines designed for human interaction was identified. Two distinct methods of closing this discrepancy have been proposed with an emphasis on lower-limb prosthesis and exercise applications. First, a control method based on impulse-momentum sliding mode control for implementation in a hip emulation robot has been proposed as a prototype pre-human trial test solution. This control had already been shown to produce the effect of human weight settling onto the prosthesis being tested in a vertical motion. Extension to walking by determining the necessary switching law exposed the need for improved swing-phase tracking, and several steps to achieve better gait were outlined.

Additional evaluation of the force measurements is called for due to the possibility of generating appropriate forces but walking on the heel or toe alone. Finally, a unique direction for gait emulation, namely creating virtual environments, is opened by this research.

Second, muscle-actuated linkage simulation methods for human subsystems have been offered as a pre-prototype solution. The fundamental dynamics of such a system were initially studied, providing direction for the linkage simulation. Control by the backstepping method was identified as a well-structured framework to complete such simulations, and it inspired two methods for resolving redundancy in the muscle actuators. However, the lacking ability to apply constraints within backstepping as formulated guided investigations toward an alternative method capable of prediction.

Beginning to address the need for computationally efficient predictive methods in musculoskeletal modeling, an optimal control solver was invented. This solver employs differential flatness to parameterize the system dynamics in terms of the muscle co-contractions, which are represented with SOS polynomials. The combination of these techniques results in measurably faster solutions to the system dynamics given a trajectory, particular for cases that can analytically be reduced to a linear program. Implementation of the solver in the context of an optimal exercise problem exhibited its capacity to support open-loop musculoskeletal system studies involving human-machine interaction, and the groundwork has been laid for closed-loop receding horizon models.

In summary, the dissertation comprised two projects related to the boundaries between humans and assistive-robotics. First, efforts to close the boundary formed when a human is joined with a robot are considered via the realm of powered trans-femoral prostheses. Second, two methods to further widen the boundary between machine ideation and human tests are established. One focuses on prototype testing, and the other concentrates on pre-prototype simulation. The combination of these

two projects represent an improved development path for human-machine systems.

## 7.2 Contributions

**Objective 1: To design a simplified powered prosthesis controller and prototype with energy regeneration**

- **Chapter II:** Invented a control method that is force modulated and can handle variable walking speeds while explicitly considering energy regeneration.
- **Chapter IV:** Validated the prosthesis prototype, control method, and energy regeneration by holding trials with an individual with a transfemoral amputation. Measurable features of walking gait and self-powered operation are achieved.

### *Publications*

1. Warner, H., Khalaf, P., Richter, H., Simon, D., Hardin, E., and van den Bogert, A. J., 2020. “Powered transfemoral prosthesis with force-modulated impedance control and energy regeneration: A walking gait trial”. *IEEE Transactions on Biomedical Engineering*. (under review).
2. Khalaf, P., Warner, H., Hardin, E., Richter, H., and Simon, D., 2018. “Development and experimental validation of an energy regenerative prosthetic knee controller and prototype”. In Proceedings of the American Society of Mechanical Engineers Dynamic Systems and Control Conference, p. V001T07A008.

**Objective 2: To extend impulse-momentum sliding mode control to emulate weight-bearing gait with a robot for prosthesis mechanical testing**

- **Chapter III:** Identified a switching law to enable walking gait for the weight simulating controller, and performed mechanical testing of the prosthesis with the gait emulation system.

**Objective 3: To develop a framework for closed-loop muscle-actuated linkage simulation of a human**

- **Chapter V:** Designed a framework for simulating human subsystems as muscle-actuated linkages under closed-loop control. Assessed the closed-loop simulation by application to a human arm model.

***Publications***

1. Warner, H., Richter, H., and van den Bogert, A. J., 2019. “Backstepping control of open-chain linkages actuated by antagonistic Hill muscles”. *Journal of Dynamic Systems, Measurement, and Control*. (under review).
2. Warner, H., Richter, H., and van den Bogert, A., 2017. “Nonlinear tracking control of an antagonistic muscle pair actuated system”. In Proceedings of the American Society of Mechanical Engineers Dynamic Systems and Control Conference, p. V001T38A006.
3. Nguyen, T. T., Warner, H., La, H., Mohammadi, H., Simon, D., and Richter, H., 2019. “State estimation for an agonistic-antagonistic muscle system”. *Asian Journal of Control*, **21**(1), pp. 354–363.
4. Richter, H., and Warner, H., 2017. “Stable nonlinear control of an agonist-antagonist muscle-driven system”. *IFAC Proceedings Volumes*, **50**(1), pp. 7199–7204.
5. Nguyen, T., Warner, H., Mohammadi, H., Simon, D., and Richter, H., 2017. “On the state estimation of an agonistic-antagonistic muscle system”. In Proceedings

of the American Society of Mechanical Engineers Dynamic Systems and Control Conference, p. V001T37A005.

**Objective 4: To establish an efficient open-loop musculoskeletal system solver**

- **Chapter VI:** Introduced a novel parameterization for musculoskeletal system dynamics. Evaluated its accuracy by comparison to published data and computational efficiency by application to exercise optimization.

### ***Publications***

1. Warner, H., and Richter, H., 2020. “Musculoskeletal dynamics simulation by differential flatness and sum of squares methods: Application to optimal exercise”. (in preparation).
2. Richter, H., and Warner, H., 2020. “Motion optimization for musculoskeletal dynamics: A flatness-based sum of squares approach”. *IEEE Transactions on Automatic Control*. (under review).

## **7.3 Future Work**

The field of powered prostheses leaves much space for progress. The limited commercial availability of powered devices attests to this fact. For the prosthesis developments presented in this dissertation, future directions should include an investigation into the frontiers of the proposed controller, expanding its recognized capacities to other activities of daily living besides walking. In addition, movement toward adding an integrated powered ankle should take place alongside a general design optimization, particularly emphasizing energy efficiency.

Advancing the mechanical testing of prostheses by robotic gait emulation is a relatively new concept. The impulse-momentum sliding mode control approach improves

gait fidelity for such a robot, but it also allows for emulation of virtual environments. The extent to which this can be attained is an open question.

Pre-prototype simulation of human-machine interaction can bolster the design process and provide an increased measure of safety. The results of this dissertation point to the significance of prediction when closing the loop for these methods. Progress in computational methods enable prediction in practice. Formally defining this problem in terms of receding horizon control, or preferably MPC which provides stronger guarantees, might finish opening the door to a more rigorous concept testing methodology to be applied before human trials.

## BIBLIOGRAPHY

- [1] Ackermann, M., and van den Bogert, A. J., 2010. “Optimality principles for model-based prediction of human gait”. *Journal of Biomechanics*, **43**(6), pp. 1055–60.
- [2] Ackermann, M., and van den Bogert, A. J., 2012. “Predictive simulation of gait at low gravity reveals skipping as the preferred locomotion strategy”. *Journal of Biomechanics*, **45**(7), pp. 1293–1298.
- [3] Alias, N. A., Huq, M. S., Ibrahim, B., and Omar, R., 2017. “The efficacy of state of the art overground gait rehabilitation robotics: A bird’s eye view”. *Procedia Computer Science*, **105**, pp. 365–370.
- [4] Anderson, F. C., and Pandy, M. G., 2001. “Dynamic optimization of human walking”. *Journal of Biomechanical Engineering*, **123**(5), pp. 381–390.
- [5] Andrews, G., 1985. “A general method for determining the functional role of a muscle”. *Journal of Biomedical Engineering*, **107**(4), pp. 348–353.
- [6] Au, S. K., Weber, J., and Herr, H., 2009. “Powered ankle-foot prosthesis improves walking metabolic economy”. *IEEE Transactions on Robotics*, **25**(1), pp. 51–66.

- [7] Blana, D., 2006. <https://simtk.org/svn/multidomain/MMS/mdl/arm2d/das1.bio>. Accessed: 2018-10-27.
- [8] Boyd, S., and Vandenberghe, L., 2004. *Convex Optimization*. Cambridge University Press.
- [9] Burnett, D. R., Campbell-Kyureghyan, N. H., Cerrito, P. B., and Quesada, P. M., 2011. “Symmetry of ground reaction forces and muscle activity in asymptomatic subjects during walking, sit-to-stand, and stand-to-sit tasks”. *Journal of Electromyography and Kinesiology*, **21**(4), pp. 610–615.
- [10] Cao, W., Yu, H., Zhao, W., Meng, Q., and Wei, X., 2017. “Simulation and evaluation prototype of intelligent lower limb prosthesis based on function requirements of human-machine system”. In *Proceedings of the 17th International Conference on MMESE*, Springer, pp. 307–313.
- [11] Cavallaro, E. E., Rosen, J., Perry, J. C., and Burns, S., 2006. “Real-time myoprocessors for a neural controlled powered exoskeleton arm”. *IEEE Transactions on Biomedical Engineering*, **53**(11), pp. 2387–96.
- [12] Conway, B. E., 2013. *Electrochemical supercapacitors: scientific fundamentals and technological applications*. Springer Science & Business Media.
- [13] Cooke, J. D., and Brown, S. H., 1994. “Movement-related phasic muscle activation: III. The duration of phasic agonist activity initiating movement”. *Experimental Brain Research*, **99**(3), pp. 473–482.
- [14] Davis, R., Richter, H., Simon, D., and van den Bogert, A., 2014. “Evolutionary optimization of ground reaction force for a prosthetic leg testing robot”. In *Proceedings of the American Control Conference*, pp. 4081–4086.



- [15] Davis, R. J., 2014. “Evolutionary ground reaction force control of a prosthetic leg testing robot”. Master’s thesis, Cleveland State University.
- [16] de las Casas, H., Richter, H., and van den Bogert, A., 2017. “Design and hybrid impedance control of a powered rowing machine”. In Proceedings of the American Society of Mechanical Engineers Dynamic Systems and Control Conference, p. V001T38A002.
- [17] Delp, S. L., Anderson, F. C., Arnold, A. S., Loan, P., Habib, A., John, C. T., Guendelman, E., and Thelen, D. G., 2007. “Opensim: open-source software to create and analyze dynamic simulations of movement”. *IEEE Transactions on Biomedical Engineering*, **54**(11), pp. 1940–1950.
- [18] Ding, L., Gao, H., Deng, Z., Song, J., Liu, Y., Liu, G., and Iagnemma, K., 2013. “Foot–terrain interaction mechanics for legged robots: Modeling and experimental validation”. *The International Journal of Robotics Research*, **32**(13), pp. 1585–1606.
- [19] Dixon, J., Nakashima, I., Arcos, E. F., and Ortúzar, M., 2010. “Electric vehicle using a combination of ultracapacitors and zebra battery”. *IEEE Transactions on Industrial Electronics*, **57**(3), pp. 943–949.
- [20] dos Santos, E. G., and Richter, H., 2019. “Design and analysis of novel actuation mechanism with controllable stiffness”. *Actuators*, **8**(1).
- [21] Edwards, C., and Spurgeon, S., 1998. *Sliding Mode Control: Theory and Applications*. CRC Press.
- [22] Eilenberg, M. F., Geyer, H., and Herr, H., 2010. “Control of a powered ankle–foot prosthesis based on a neuromuscular model”. *IEEE Transactions on Neural Systems and Rehabilitation Engineering*, **18**(2), pp. 164–173.

- [23] Embry, K. R., Villarreal, D. J., and Gregg, R. D., 2016. “A unified parameterization of human gait across ambulation modes”. In Proceedings of the Institute of Electrical and Electronic Engineers Engineering in Medicine and Biology Society Annual Conference, p. 2179.
- [24] Fakoorian, S., Azimi, V., Moosavi, M., Richter, H., and Simon, D., 2017. “Ground reaction force estimation in prosthetic legs with nonlinear kalman filtering methods”. *Journal of Dynamic Systems, Measurement, and Control*, **139**(11), p. 111004.
- [25] Fey, N. P., Simon, A. M., Young, A. J., and Hargrove, L. J., 2013. “Knee swing-initiation and ankle plantar flexion control using an active prosthesis across walking speeds and users”. In Proceedings of the Annual meeting of the American Society of Biomechanics, pp. 85–86.
- [26] Ficanha, E., Dallali, H., and Rastgaar, M., 2017. “Gait emulator for evaluation of a powered ankle-foot prosthesis”. In Proceedings of the American Society of Mechanical Engineers Dynamic Systems and Control Conference, p. V001T36A001.
- [27] Ficanha, E., Rastgaar, M., and Kaufman, K. R., 2015. “Gait emulator for evaluation of ankle-foot prostheses capable of turning”. *Journal of Medical Devices*, **9**(3), p. 030908.
- [28] Fliess, M., Lévine, J., Martin, P., and Rouchon, P., 1995. “Flatness and defect of non-linear systems: introductory theory and examples”. *International Journal of Control*, **61**(6), pp. 1327–1361.
- [29] Gailey, R., Allen, K., Castles, J., Kucharik, J., and Roeder, M., 2008. “Review of secondary physical conditions associated with lower-limb amputation and

- long-term prosthesis use”. *Journal of Rehabilitation Research and Development*, **45**(1), pp. 15–29.
- [30] Geyer, H., and Seyfarth, A., 2019. *Neuromuscular Control Models of Human Locomotion*. Springer Netherlands, pp. 979–1007.
- [31] Grabke, E. P., and Andrysek, J., 2018. “Applications of musculoskeletal modelling and simulation for lower-limb prosthesis design optimization”. In *Proceedings of the American Society of Mechanical Engineers International Design Engineering Technical Conferences and Computers and Information in Engineering Conference*, p. V02BT03A027.
- [32] Gregg, R. D., Lenzi, T., Hargrove, L. J., and Sensinger, J. W., 2014. “Virtual constraint control of a powered prosthetic leg: From simulation to experiments with transfemoral amputees”. *IEEE Transactions on Robotics*, **30**(6), pp. 1455–1471.
- [33] Hafner, B. J., and Askew, R. L., 2015. “Physical performance and self-report outcomes associated with use of passive, adaptive, and active prosthetic knees in persons with unilateral, transfemoral amputation: Randomized crossover trial”. *Journal of Rehabilitation Research and Development*, **52**(6).
- [34] He, J., Levine, W. S., and Loeb, G. E., 1991. “Feedback gains for correcting small perturbations to standing posture”. *IEEE Transactions on Automatic Control*, **36**(3), pp. 322–332.
- [35] Helbostad, J. L., Leirfall, S., Moe-Nilssen, R., and Sletvold, O., 2007. “Physical fatigue affects gait characteristics in older persons”. *The Journals of Gerontology Series A: Biological Sciences and Medical Sciences*, **62**(9), pp. 1010–1015.
- [36] Hilbert, D., 1933. “Über die darstellung definiter formen als summe von formenquadraten”. In *Algebra: Invariantentheorie: Geometrie*. Springer, pp. 154–161.

- [37] Hill, A. V., 1938. “The heat of shortening and the dynamic constants of muscle”. *Proceedings of the Royal Society of London B: Biological Sciences*, **126**(843), pp. 136–195.
- [38] Hitt, J., Sugar, T., Holgate, M., Bellman, R., and Hollander, K., 2009. “Robotic transtibial prosthesis with biomechanical energy regeneration”. *Industrial Robot*, **36**(5), pp. 441–447.
- [39] Hitt, J. K., Sugar, T. G., Holgate, M., and Bellman, R., 2010. “An active foot-ankle prosthesis with biomechanical energy regeneration”. *Journal of Medical Devices*, **4**(1), p. 011003.
- [40] Hogan, N., 1984. “Adaptive control of mechanical impedance by coactivation of antagonist muscles”. *IEEE Transactions on Automatic Control*, **29**(8), pp. 681–690.
- [41] Hogan, N., 1985. “Impedance control: An approach to manipulation: Part I–Theory”. *Journal of Dynamic Systems, Measurement, and Control*, **107**, pp. 1–7.
- [42] Hogan, N., 1985. “Impedance control: An approach to manipulation: Part II–Implementation”. *Journal of Dynamic Systems, Measurement, and Control*, **107**, pp. 8–16.
- [43] Hogan, N., 1985. “Impedance control: An approach to manipulation: Part III–Applications”. *Journal of Dynamic Systems, Measurement, and Control*, **107**, pp. 17–24.
- [44] Hood, S., and Lenzi, T., 2018. “Preliminary analysis of positive knee energy injection in a transfemoral amputee walking with a powered prosthesis”. In Institute of Electrical and Electronic Engineers Engineering in Medicine and Biology Society Annual Conference, pp. 17–21.

- [45] Hunter, B. L., 1981. “Design of a self-contained, active, regenerative computer controlled above-knee prosthesis”. Master’s thesis, Massachusetts Institute of Technology.
- [46] Huxley, H. E., 1957. “The double array of filaments in cross-striated muscle”. *The Journal of Biophysical and Biochemical Cytology*, **3**(5), pp. 631–648.
- [47] Ingraham, K. A., Fey, N. P., Simon, A. M., and Hargrove, L. J., 2016. “Assessing the relative contributions of active ankle and knee assistance to the walking mechanics of transfemoral amputees using a powered prosthesis”. *PloS one*, **11**(1), p. e0147661.
- [48] Jagodnik, K. M., and van den Bogert, A. J., 2010. “Optimization and evaluation of a proportional derivative controller for planar arm movement”. *Journal of Biomechanics*, **43**(6), pp. 1086–1091.
- [49] Johansen, T. A., and Fossen, T. I., 2013. “Control allocation—a survey”. *Automatica*, **49**(5), pp. 1087–1103.
- [50] Johansson, J. L., Sherrill, D. M., Riley, P. O., Bonato, P., and Herr, H., 2005. “A clinical comparison of variable-damping and mechanically passive prosthetic knee devices”. *American Journal of Physical Medicine & Rehabilitation*, **84**(8), pp. 563–575.
- [51] Karafyllis, I., Malisoff, M., de Queiroz, M., Krstic, M., and Yang, R., 2014. “A new tracking controller for neuromuscular electrical stimulation under input delays: Case study in prediction”. In *Proceedings of the American Control Conference*, pp. 4186–4191.
- [52] Karafyllis, I., Malisoff, M., de Queiroz, M., Krstic, M., and Yang, R., 2015. “Predictor-based tracking for neuromuscular electrical stimulation”. *International Journal of Robust and Nonlinear Control*, **25**(14), pp. 2391–2419.

- [53] Karimian, M., Towhidkhah, F., and Rostami, M., 2006. “Application of model predictive impedance control (MPIC) in analysis of human walking on rough terrains”. *International Journal of Applied Electromagnetics and Mechanics*, **24**(3-4), pp. 147–162.
- [54] Katz, B., 1939. “The relation between force and speed in muscular contraction”. *The Journal of Physiology*, **96**(1), p. 45.
- [55] Khademi, G., Mohammadi, H., and Simon, D., 2019. “Gradient-based multi-objective feature selection for gait mode recognition of transfemoral amputees”. *Sensors*, **19**(2), p. 253.
- [56] Khalaf, P., and Richter, H., 2016. “Parametric optimization of stored energy in robots with regenerative drive systems”. In Proceedings of the Institute of Electrical and Electronic Engineers International Conference on Advanced Intelligent Mechatronics, pp. 1424–1429.
- [57] Khalaf, P., and Richter, H., 2018. “On global, closed-form solutions to parametric optimization problems for robots with energy regeneration”. *Journal of Dynamic Systems, Measurement, and Control*, **140**(3), p. 031003.
- [58] Khalaf, P., and Richter, H., 2019. “Trajectory optimization of robots with regenerative drive systems: Numerical and experimental results”. *IEEE Transactions on Robotics*.
- [59] Khalaf, P., Warner, H., Hardin, E., Richter, H., and Simon, D., 2018. “Development and experimental validation of an energy regenerative prosthetic knee controller and prototype”. In Proceedings of the American Society of Mechanical Engineers Dynamic Systems and Control Conference, p. V001T07A008.
- [60] Khalil, H. K., 2002. *Nonlinear systems*, 3 ed. Prentice Hall, Upper Saddle River, New Jersey.

- [61] Kirtley, C., Whittle, M. W., and Jefferson, R., 1985. “Influence of walking speed on gait parameters”. *Journal of Biomedical Engineering*, **7**(4), pp. 282–288.
- [62] Kokotovic, P. V., 1992. “The joy of feedback: nonlinear and adaptive”. *IEEE Control Systems Magazine*, **12**(3), pp. 7–17.
- [63] Koo, B., and Leonessa, A., 2011. “An adaptive block backstepping control design for functional electrical stimulation of agonist–antagonist muscles”. In Proceedings of the American Society of Mechanical Engineers Dynamic Systems and Control Conference and Symposium on Fluid Power and Motion Control, pp. 479–486.
- [64] Kotina, R., Zheng, Q., van den Bogert, A. J., and Gao, Z., 2011. “Active disturbance rejection control for human postural sway”. In Proceedings of the American Control Conference, pp. 4081–4086.
- [65] Krebs, H. I., Volpe, B. T., Aisen, M., Hening, W., Adamovich, S., Poizner, H., Subrahmanyam, K., and Hogan, N., 2003. “Robotic applications in neuromotor rehabilitation”. *Robotica*, **21**(1), pp. 3–11.
- [66] Krstic, M., Kanellakopoulos, I., and Kokotovic, P., 1995. *Nonlinear and adaptive control design*. Wiley New York.
- [67] Laschowski, B., McPhee, J., and Andrysek, J., 2019. “Lower-limb prostheses and exoskeletons with energy regeneration: Mechatronic design and optimization review”. *Journal of Mechanisms and Robotics*, **11**, pp. 1–39.
- [68] Lawson, B. E., Mitchell, J., Truex, D., Shultz, A., Ledoux, E., and Goldfarb, M., 2014. “A robotic leg prosthesis: Design, control, and implementation”. *IEEE Robotics and Automation Magazine*, **21**(4), pp. 70–81.

- [69] Lawson, B. E., Varol, H. A., Huff, A., Erdemir, E., and Goldfarb, M., 2013. “Control of stair ascent and descent with a powered transfemoral prosthesis”. *IEEE Transactions on Neural Systems and Rehabilitation Engineering*, **21**(3), pp. 466–473.
- [70] Levin, O., Ouamer, M., Steyvers, M., and Swinnen, S. P., 2001. “Directional tuning effects during cyclical two-joint arm movements in the horizontal plane”. *Experimental Brain Research*, **141**(4), pp. 471–484.
- [71] Li, P. Y., and Horowitz, R., 1997. “Control of smart exercise machines—Part I: Problem formulation and non-adaptive control”. *IEEE/ASME Transactions on Mechatronics*, **2**(4), pp. 237–247.
- [72] Li, P. Y., and Horowitz, R., 1997. “Control of smart exercise machines—Part II: Self-optimizing control”. *IEEE/ASME Transactions on Mechatronics*, **2**(4), pp. 248–258.
- [73] Marinelli, C., 2016. “Design, development and engineering of a bench for testing lower limb prosthesis, with focus on high-technological solutions”. PhD thesis, Polytechnic University of Milan.
- [74] Marinelli, C., Giberti, H., and Resta, F., 2015. “Conceptual design of a gait simulator for testing lower-limb active prostheses”. In Proceedings of the Research and Education in Mechatronics Conference, pp. 314–320.
- [75] Martin, A. E., and Gregg, R. D., 2017. “Stable, robust hybrid zero dynamics control of powered lower-limb prostheses”. *IEEE Transactions on Automatic Control*.
- [76] Martin, P., Murray, R. M., and Rouchon, P., 2003. Flat systems, equivalence and trajectory generation. Tech. rep., California Institute of Technology.



- [77] Martinez-Villalpando, E. C., and Herr, H., 2009. “Agonist-antagonist active knee prosthesis: A preliminary study in level-ground walking”. *Journal of Rehabilitation Research & Development*, **46**(3).
- [78] McLean, S. G., Su, A., and van den Bogert, A. J., 2004. “Development and validation of a 3-D model to predict knee joint loading during dynamic movement”. *Journal of Biomechanical Engineering*, **125**(6), pp. 864–874.
- [79] Mehrabi, N., Sharif Razavian, R., Ghannadi, B., and McPhee, J., 2017. “Predictive simulation of reaching moving targets using nonlinear model predictive control”. *Frontiers in Computational Neuroscience*, **10**, p. 143.
- [80] Menegaldo, L. L., de Toledo Fleury, A., and Weber, H. I., 2006. “A ‘cheap’ optimal control approach to estimate muscle forces in musculoskeletal systems”. *Journal of Biomechanics*, **39**(10), pp. 1787–95.
- [81] Mobayen, S., 2016. “Finite-time robust-tracking and model-following controller for uncertain dynamical systems”. *Journal of Vibration and Control*, **22**(4), pp. 1117–1127.
- [82] Mobayen, S., and Tchier, F., 2017. “Design of an adaptive chattering avoidance global sliding mode tracker for uncertain non-linear time-varying systems”. *Transactions of the Institute of Measurement and Control*, **39**(10), pp. 1547–1558.
- [83] Moulay, E., and Perruquetti, W., 2006. “Finite time stability and stabilization of a class of continuous systems”. *Journal of Mathematical Analysis and Applications*, **323**(2), pp. 1430–1443.
- [84] Nguyen, T., Warner, H., Mohammadi, H., Simon, D., and Richter, H., 2017. “On the state estimation of an agonistic-antagonistic muscle system”. In Pro-

ceedings of the American Society of Mechanical Engineers Dynamic Systems and Control Conference, p. V001T37A005.

- [85] Nguyen, T. T., Warner, H., La, H., Mohammadi, H., Simon, D., and Richter, H., 2019. “State estimation for an agonistic-antagonistic muscle system”. *Asian Journal of Control*, **21**(1), pp. 354–363.
- [86] Össur, 2017. *Power Knee<sup>®</sup> Instructions for Use*. Össur, Reykjavík, Iceland. <https://assets.ossur.com/library/22242/POWER%20KNEE%20Instructions%20for%20use.pdf>.
- [87] Ottobock, 2017. *Empower<sup>TM</sup> MP Foot Specification Sheet*. Ottobock, Duderstadt, Germany. <https://professionals.ottobockus.com/media/pdf/14589-Empower-Spec-Sheet.pdf>.
- [88] Parrilo, P. A., 2003. “Semidefinite programming relaxations for semialgebraic problems”. *Mathematical Programming*, **96**(2), pp. 293–320.
- [89] Pieringer, D. S., Grimmer, M., Russold, M. F., and Riener, R., 2017. “Review of the actuators of active knee prostheses and their target design outputs for activities of daily living”. In Proceedings of the Institute of Electrical and Electronic Engineers International Conference on Rehabilitation Robotics, pp. 1246–1253.
- [90] Powell, B. T., 2017. “Investigation of extremum seeking control for adaptive exercise machines”. Master’s thesis, Cleveland State University.
- [91] Powell, M. J., Cousineau, E. A., and Ames, A. D., 2015. “Model predictive control of underactuated bipedal robotic walking”. In 2015 IEEE International Conference on Robotics and Automation (ICRA), IEEE, pp. 5121–5126.
- [92] Prajna, S., Papachristodoulou, A., and Parrilo, P. A., 2002. “Introducing SOS-TOOLS: a general purpose sum of squares programming solver”. In Proceedings

of the Institute of Electrical and Electronic Engineers Conference on Decision and Control, pp. 741–746.

- [93] Quintero, D., Villarreal, D. J., Lambert, D. J., Kapp, S., and Gregg, R. D., 2018. “Continuous-phase control of a powered knee–ankle prosthesis: Amputee experiments across speeds and inclines”. *IEEE Transactions on Robotics*, **34**(3), pp. 686–701.
- [94] Reznick, B., 1996. “Some concrete aspects of Hilbert’s 17th problem”. In *Real algebraic geometry and ordered structures*, Vol. 253, pp. 251–272.
- [95] Richter, H., 2015. “A framework for control of robots with energy regeneration”. *Journal of Dynamic Systems, Measurement, and Control*, **137**(9), p. 091004.
- [96] Richter, H., Mobayen, S., and Simon, D., 2018. “Contact and tracking hybrid control with impulse-momentum sliding surface and terminal sliding mode”. In *Proceedings of the American Society of Mechanical Engineers Dynamic Systems and Control Conference*, p. V001T04A001.
- [97] Richter, H., and Selvaraj, D., 2015. “Impedance control with energy regeneration in advanced exercise machines”. In *Proceedings of the American Control Conference*, pp. 5890–5895.
- [98] Richter, H., and Simon, D., 2014. “Robust tracking control of a prosthesis test robot”. *Journal of Dynamic Systems, Measurement, and Control*, **136**(3), p. 031011.
- [99] Richter, H., Simon, D., Smith, W. A., and Samorezov, S., 2015. “Dynamic modeling, parameter estimation and control of a leg prosthesis test robot”. *Applied Mathematical Modelling*, **39**(2), pp. 559–573.

- [100] Richter, H., Simon, D. J., and van den Bogert, A. J., 2014. “Semiactive virtual control method for robots with regenerative energy-storing joints”. *IFAC Proceedings Volumes*, **47**(3), pp. 10244–10250.
- [101] Richter, H., and Warner, H., 2017. “Stable nonlinear control of an agonist-antagonist muscle-driven system”. *IFAC Proceedings Volumes*, **50**(1), pp. 7199–7204.
- [102] Richter, H., and Warner, H., 2020. “Motion optimization for musculoskeletal dynamics: A flatness-based sum of squares approach”. *IEEE Transactions on Automatic Control*. (under review).
- [103] Rouse, E. J., Mooney, L. M., Martinez-Villalpando, E. C., and Herr, H. M., 2013. “Clutchable series-elastic actuator: Design of a robotic knee prosthesis for minimum energy consumption”. In Proceedings of the Institute of Electrical and Electronic Engineers International Conference on Rehabilitation Robotics, pp. 1–6.
- [104] Sanderson, D. J., and Martin, P. E., 1997. “Lower extremity kinematic and kinetic adaptations in unilateral below-knee amputees during walking”. *Gait & Posture*, **6**(2), pp. 126–136.
- [105] Segal, A. D., Orendurff, M. S., Klute, M. K., McDowell, M. L., Pecoraro, J. A., Shofer, J., and Czerniecki, J. M., 2006. “Kinematic and kinetic comparisons of transfemoral amputee gait using C-Leg<sup>®</sup> and Mauch SNS<sup>®</sup> prosthetic knees”. *Journal of Rehabilitation Research & Development*, **43**(7), pp. 857–870.
- [106] Seth, B., 1987. “Energy regeneration and its application to active above-knee prostheses”. PhD thesis, Massachusetts Institute of Technology.

- [107] Shen, C., Shi, Y., and Buckham, B., 2017. “Trajectory tracking control of an autonomous underwater vehicle using Lyapunov-based model predictive control”. *IEEE Transactions on Industrial Electronics*, **65**(7), pp. 5796–5805.
- [108] Shourijeh, M. S., Mehrabi, N., and McPhee, J., 2017. “Forward static optimization in dynamic simulation of human musculoskeletal systems: A proof-of-concept study”. *Journal of Computational and Nonlinear Dynamics*, **12**(5), p. 051005.
- [109] Shultz, A. H., Lawson, B. E., and Goldfarb, M., 2015. “Running with a powered knee and ankle prosthesis”. *IEEE Transactions on Neural Systems and Rehabilitation Engineering*, **23**(3), pp. 403–412.
- [110] Simon, A. M., Ingraham, K. A., Fey, N. P., Finucane, S. B., Lipschutz, R. D., Young, A. J., and Hargrove, L. J., 2014. “Configuring a powered knee and ankle prosthesis for transfemoral amputees within five specific ambulation modes”. *PloS one*, **9**(6), p. e99387.
- [111] Simon, D., 2008. “Biogeography-based optimization”. *IEEE Transactions on Evolutionary Computation*, **12**(6), pp. 702–713.
- [112] Simon, D., 2013. *Evolutionary Optimization Algorithms*. John Wiley & Sons.
- [113] Slotine, J.-J. E., and Li, W., 1991. *Applied nonlinear control*. Prentice Hall.
- [114] Spong, M. W., Hutchinson, S., and Vidyasagar, M., 2006. *Robot modeling and control*, Vol. 3. Wiley New York.
- [115] Struyf, P. A., van Heugten, C. M., Hitters, M. W., and Smeets, R. J., 2009. “The prevalence of osteoarthritis of the intact hip and knee among traumatic leg amputees”. *Archives of Physical Medicine and Rehabilitation*, **90**(3), pp. 440–446.

- [116] Sun, J., 2015. “Dynamic modeling of human gait using a model predictive control approach”. PhD thesis, Marquette University.
- [117] Sun, J., and Voglewede, P. A., 2014. “Dynamic simulation of human gait using a combination of model predictive and PID control”. In ASME 2014 International Design Engineering Technical Conferences and Computers and Information in Engineering Conference, American Society of Mechanical Engineers, p. V006T10A008.
- [118] Sup, F., Bohara, A., and Goldfarb, M., 2008. “Design and control of a powered transfemoral prosthesis”. *The International Journal of Robotics Research*, **27**(2), pp. 263–273.
- [119] Sup, F., Varol, H. A., and Goldfarb, M., 2011. “Upslope walking with a powered knee and ankle prosthesis: Initial results with an amputee subject”. *IEEE Transactions on Neural Systems and Rehabilitation Engineering*, **19**(1), pp. 71–78.
- [120] Sup, F., Varol, H. A., Mitchell, J., Withrow, T., and Goldfarb, M., 2008. “Design and control of an active electrical knee and ankle prosthesis”. In Proceedings of the Institute of Electrical and Electronic Engineers Conference on Biomedical Robotics and Biomechatronics, pp. 523–528.
- [121] Sup, F., Varol, H. A., Mitchell, J., Withrow, T. J., and Goldfarb, M., 2009. “Preliminary evaluations of a self-contained anthropomorphic transfemoral prosthesis”. *IEEE/ASME Transactions on Mechatronics*, **14**(6), pp. 667–676.
- [122] Sup, F., Varol, H. A., Mitchell, J., Withrow, T. J., and Goldfarb, M., 2009. “Self-contained powered knee and ankle prosthesis: Initial evaluation on a transfemoral amputee”. In Proceedings of the Institute of Electrical and Electronic

Engineers International Conference on Rehabilitation Robotics, IEEE, pp. 638–644.

- [123] Tabor, K. A., 1988. “The real-time digital control of a regenerative above-knee prosthesis”. Master’s thesis, Massachusetts Institute of Technology.
- [124] Takahama, T., and Sakai, S., 2009. *Solving Difficult Constrained Optimization Problems by the  $\varepsilon$  Constrained Differential Evolution with Gradient-Based Mutation*. Springer, pp. 51–72.
- [125] Tee, K. P., and Ge, S. S., 2011. “Control of nonlinear systems with partial state constraints using a barrier Lyapunov function”. *International Journal of Control*, **84**(12), pp. 2008–2023.
- [126] Tee, K. P., and Ge, S. S., 2012. “Control of state-constrained nonlinear systems using integral barrier Lyapunov functionals”. In Proceedings of the Institute of Electrical and Electronic Engineers Conference on Decision and Control, pp. 3239–3244.
- [127] Tee, K. P., Ren, B., and Ge, S. S., 2011. “Control of nonlinear systems with time-varying output constraints”. *Automatica*, **47**(11), pp. 2511–2516.
- [128] Thomas, P., Branicky, M., van den Bogert, A., and Jagodnik, K., 2009. “Application of the actor–critic architecture to functional electrical stimulation control of a human arm”. In Proceedings of the Innovative Applications of Artificial Intelligence Conference, pp. 165–172.
- [129] Towhidkhah, F., Gander, R. E., and Wood, H. C., 1997. “Model predictive impedance control: A model for joint movement”. *Journal of Motor Behavior*, **29**(3), pp. 209 – 222.

- [130] Tucker, M. R., and Fite, K. B., 2010. “Mechanical damping with electrical regeneration for a powered transfemoral prosthesis”. In Proceedings of the American Society of Mechanical Engineers and Institute of Electrical and Electronic Engineers International Conference on Advanced Intelligent Mechatronics, pp. 13–18.
- [131] Utkin, V. I., 2013. *Sliding Modes in Control and Optimization*. Springer Science & Business Media.
- [132] van den Bogert, A. J., Geijtenbeek, T., Even-Zohar, O., Steenbrink, F., and Hardin, E. C., 2013. “A real-time system for biomechanical analysis of human movement and muscle function”. *Medical & Biological Engineering & Computing*, **51**(10), pp. 1069–1077.
- [133] van Ingen Schenau, G. J., Van Woensel, W. W. L. M., Boots, P. J. M., Snackers, R. W., and de Groot, G., 1990. “Determination and interpretation of mechanical power in human movement: application to ergometer cycling”. *European Journal of Applied Physiology and Occupational Physiology*, **61**(1-2), pp. 11–19.
- [134] Venkataraman, S., and Gulati, S., 1993. “Control of nonlinear systems using terminal sliding modes”. *Journal of Dynamic Systems, Measurement, and Control*, **115**(3), pp. 554–560.
- [135] Wang, Y., and Srinivasan, M., 2014. “Stepping in the direction of the fall: The next foot placement can be predicted from current upper body state in steady-state walking”. *Biology Letters*, **10**(9), p. 20140405.
- [136] Warner, H., 2015. “Optimal design and control of a lower-limb prosthesis with energy regeneration”. Master’s thesis, Cleveland State University.
- [137] Warner, H., Khalaf, P., Richter, H., Simon, D., Hardin, E., and van den Bogert, A. J., 2020. “Powered transfemoral prosthesis with force-modulated impedance



- control and energy regeneration: A walking gait trial”. *IEEE Transactions on Biomedical Engineering*. (under review).
- [138] Warner, H., and Richter, H., 2020. “Musculoskeletal dynamics simulation by differential flatness and sum of squares methods: Application to optimal exercise”. (in preparation).
  - [139] Warner, H., Richter, H., and van den Bogert, A., 2017. “Nonlinear tracking control of an antagonistic muscle pair actuated system”. In Proceedings of the American Society of Mechanical Engineers Dynamic Systems and Control Conference, p. V001T38A006.
  - [140] Warner, H., Richter, H., and van den Bogert, A. J., 2019. “Backstepping control of open-chain linkages actuated by antagonistic Hill muscles”. *Journal of Dynamic Systems, Measurement, and Control*. (under review).
  - [141] Warner, H., Simon, D., Mohammadi, H., and Richter, H., 2016. “Switched robust tracking/impedance control for an active transfemoral prosthesis”. In Proceedings of the American Control Conference, pp. 2187–2192.
  - [142] Waters, R. L., Perry, J., Antonelli, D., and Hislop, H., 1976. “Energy cost of walking of amputees: the influence of level of amputation”. *The Journal of Bone and Joint Surgery. American Volume*, **58**(1), pp. 42–6.
  - [143] Winter, D. A., 1983. “Energy generation and absorption at the ankle and knee during fast, natural, and slow cadences”. *Clinical Orthopaedics and Related Research*(175), pp. 147–154.
  - [144] Winter, D. A., 1984. “Kinematic and kinetic patterns in human gait: Variability and compensating effects”. *Human movement Science*, **3**(1-2), pp. 51–76.

- [145] Winter, D. A., 2009. *Biomechanics and Motor Control of Human Movement*, 4th ed. John Wiley & Sons.
- [146] Winters, J. M., 1990. *Hill-based muscle models: A systems engineering perspective*. Springer, ch. 5, pp. 69–93.
- [147] Wu, S., and Voglewede, P. A., 2016. “Improvement of a forward dynamic MPC based human gait model”. In Proceedings of the American Society of Mechanical Engineers International Design Engineering Technical Conferences and Computers and Information in Engineering Conference, p. V006T09A003.
- [148] Xiang, Y., Arora, J. S., and Abdel-Malek, K., 2010. “Physics-based modeling and simulation of human walking: a review of optimization-based and other approaches”. *Structural and Multidisciplinary Optimization*, **42**(1), pp. 1–23.
- [149] Yang, R., and de Queiroz, M., 2016. “Adaptive control of the nonlinearly parameterized limb dynamics with application to neuromuscular electrical stimulation”. In Proceedings of the American Control Conference, pp. 4883–4888.
- [150] Yucesoy, C. A., Koopman, B. H. F. J. M., Huijing, P. A., and Grootenboer, H. J., 2002. “Three-dimensional finite element modeling of skeletal muscle using a two-domain approach: linked fiber-matrix mesh model”. *Journal of Biomechanics*, **35**(9), pp. 1253–1262.
- [151] Zajac, F. E., 1989. “Muscle and tendon: Properties, models, scaling, and application to biomechanics and motor control”. *Critical Reviews in Biomedical Engineering*, **17**(4), pp. 359–411.
- [152] Zelik, K. E., and Kuo, A. D., 2010. “Human walking isn’t all hard work: evidence of soft tissue contributions to energy dissipation and return”. *Journal of Experimental Biology*, **213**(24), pp. 4257–4264.

- [153] Zhang, Y., Wang, S.-h., Chang, B., and Wu, W.-h., 2019. “Adaptive constrained backstepping controller with prescribed performance methodology for carrier-based uav”. *Aerospace Science and Technology*, **92**, pp. 55–65.
- [154] Zhao, H., Horn, J., Reher, J., Paredes, V., and Ames, A. D., 2016. “Multi-contact locomotion on transfemoral prostheses via hybrid system models and optimization-based control”. *IEEE Transactions on Automation Science and Engineering*, **13**(2), pp. 502–513.
- [155] Zhao, H., Horn, J., Reher, J., Paredes, V., and Ames, A. D., 2017. “First steps toward translating robotic walking to prostheses: a nonlinear optimization based control approach”. *Autonomous Robots*, **41**(3), pp. 725–742.

## APPENDIX

## APPENDIX A

### COPYRIGHTS AND PERMISSIONS

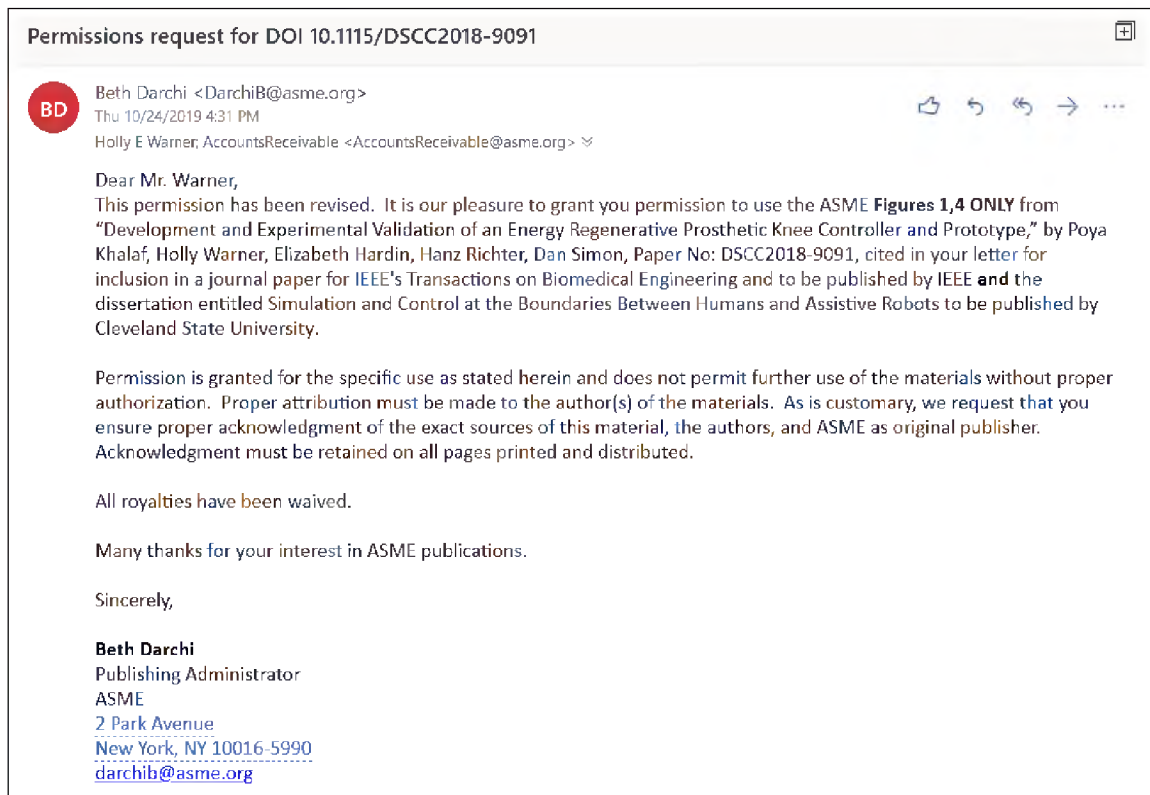




Figure 62: Permission to reuse photographs of the prosthesis prototype (Figure 1) and the volunteer wearing the prototype (Figure 9) from [59]



[Welcome](#)
[Log in](#)
[Cart \(0\)](#)
[Manage Account](#)
[Feedback](#)
[Help](#)


[Get Permission / Find Title](#)

[Go](#)

[Advanced Search Options](#)

**Looking for pay-per-use Permissions?** You're in the right place. Check out your results below.

You can no longer check license coverage for the Annual Copyright License on copyright.com. Please use [RightFind® Advisor](#) (for corporate licensees) and [RightFind® Academic](#) (for academic licensees). If you do not have access to RightFind® Advisor or RightFind® Academic please contact your Client Engagement Manager.


### Permissions Summary

[Back to results](#)

[New search](#)
[Can't find the publication you're looking for?](#)

**Journal of rehabilitation research and development**

**JOURNAL**

<b>ISSN:</b>	0748-7711	<b>Language:</b>	English	
<b>Publication year(s):</b>	1984 - present	<b>Country of publication:</b>	United States of America	
<b>Author/Editor:</b>	UNITED STATES			
<b>Publisher:</b>	THE SERVICE,			
<b>Rightsholder:</b>	JOURNAL OF REHABILITATION RESEARCH AND DEVELOPMENT			

*This work is in the public domain of the United States.  
You may use the work without restriction in the United States.*

[About Us](#) | [Privacy Policy](#) | [Terms & Conditions](#) | [Pay an Invoice](#)

Copyright 2019 Copyright Clearance Center

Figure 63: Permission to replicate the able-bodied data used for comparison in Figure 10 from [105]